

Techniques in the Optical Detection of
Magnetic Resonance using Nitrogen-
Vacancy Centre Ensembles in Diamond

Calum Donald Macrae

Centre for Biophotonics

Strathclyde Institute of Pharmacy & Biomedical Sciences

University of Strathclyde

Submitted 2018 for partial fulfilment of a PhD in Bioscience

'This thesis is the result of the author's original research. It has been composed by the author and has not been previously submitted for examination which has led to the award of a degree.'

'The copyright of this thesis belongs to the author under the terms of the United Kingdom Copyright Acts as qualified by University of Strathclyde Regulation 3.50. Due acknowledgement must always be made of the use of any material contained in, or derived from, this thesis.'

Signed: Calum Donald Macrae

Date: 09-12-2018

Abstract

Studies were performed to progress the application of nitrogen-vacancy (NV) centres to the sensing of magnetic fields.

A magnetometer using an NV centre ensemble contained within a 150 μm diameter diamond was built. Using an adapted epi-fluorescence microscopy setup and 2 mW of optical excitation, a sensitivity of $70 \pm 26 \text{ nT/Hz}^{1/2}$ was achieved with a bandwidth of 3.1 kHz. This was 110 times above the shot-noise limit of 639 pT/Hz^{1/2} and 1129 times above the spin projection noise limit of 62 pT/Hz^{1/2}. This was likely due to noise in the laser, microwaves and detectors. The experimental method requires large improvements in spin dephasing time (T_2^*) to enable the intended detection of marine worm action potentials via bio-magnetism.

Secondly, two-photon excited optical detection of magnetic resonance (2PODMR) of NV centre ensembles was successfully demonstrated. This proves two-photon excited magnetometry with NV centres possible. The 2PODMR linewidth and contrast were found to be reduced by 39.6 % and 73.7 % respectively, when compared with measurements of single-photon excited ODMR. The reduction in ODMR contrast can only partially be explained by the increased temperature and lower NV⁻/NV⁰ ratio under two-photon excitation. Two-photon excited fluorescence was also found to saturate at low fluorescence rates compared with single-photon excited fluorescence. This is likely to be related to previously measured effects where 1064 nm excitation has quenched 532 nm excited fluorescence.

Finally, a first step towards building a magneto-sensitive laser using NV centres for ultra-sensitive magnetometry was made. Direct measurements of stimulated emission from NV centre ensembles contained within a mm scale diamond were attempted but were inconclusive. Despite measuring a change in probe power using a pump-probe setup, the wavelength, power and temporal dependencies were not fully consistent with a measurement of stimulated emission. However, ODMR was successfully measured using the probe beam.

Acknowledgements

I would like to thank Gail McConnell for initiating this research, giving me the opportunity to perform my doctoral work in her research group, copious thesis feedback and her useful advice and supervision throughout. I would like to thank Erling Riis for his advice, supervision, useful technical discussions, for letting me work in one of his laboratories for 5 years and for opening my mind to the world of experimental photonics to begin with. I would also like to thank Paul Griffin for his supervision and advice throughout my time at Strathclyde University, Ewan Maclagan and Robert Wylie for their mechanical engineering advice, Gerard Drinkwater, Mark Hutcheon and Ken Gibson for their electrical engineering advice and Elmar Haller, Jonathan Pritchard and Dylan Cotta for their countless useful discussions. Finally, a big thanks to Brad Amos for bio-related advice and for teaching me to dissect ragworms and to my collaborators Alan Kemp, Vasili Savitski and Elisabeth Fraczek, from the Institute of Photonics, whose work gave me the opportunity to perform experiments with bulk diamond.

Contents

Abstract		iii
Acknowledgments		v
List of Figures		x
List of Tables		xxvi
List of Abbreviations		xxvii
Chapter 1	Introduction	1
Chapter 2	Background and Theory	8
2.1	Diamond	8
2.1.1	Diamond Synthesis	9
2.1.1.1	High Pressure / High Temperature (HPHT)	9
2.1.1.2	Chemical Vapour Deposition (CVD)	10
2.2	Nitrogen Vacancy Centres	11
2.2.1	Structure	11
2.2.2	NV Centre Synthesis	13
2.2.3	Optical Properties	14
2.2.4	Optical Transitions	14
2.2.5	Spin Transitions	16
2.2.5.1	Weak Magnetic Field Regime	20
2.2.6	Optical Detection of Magnetic Resonance (ODMR)	24
2.2.6.1	Optical Magnetic Resonance Spectroscopy	25
2.2.6.2	ODMR Linewidth	26
2.2.6.3	Magnetometric Sensitivity Limits	28

	2.2.7	ODMR Techniques	30
	2.2.8	Charge State Conversion	36
Chapter 3		Optical Magnetometry under a Microscope using Nitrogen Vacancy Centre Ensembles	38
	3.1	Overview	38
	3.2	Introduction	38
	3.3	Experimental Method	40
	3.3.1	Experimental Overview	40
	3.3.2	Theory of Operation	41
	3.3.3	Lock-in Amplifier Output	42
	3.3.4	Sensitivity Limits	46
	3.4	Experimental Set-up	47
	3.4.1	Optics	48
	3.4.2	Microwave Generation	50
	3.4.3	Microwave Negative Feedback System	50
	3.4.4	Microwave Antennae	52
	3.4.5	Photodetector	54
	3.4.6	B-Field Generation	57
	3.4.7	Data Acquisition	58
	3.5	Results	59
	3.5.1	Antennae	59
	3.5.2	Resonance Features	62
	3.5.3	ODMR Contrast	66
	3.5.4	Magnetometric Sensitivity	67
	3.5.5	Bandwidth	70
	3.5.6	Photodetectors	71
	3.5.7	Demonstration of Magnetometry	73
	3.6	Discussion	76
	3.6.1	Antennae and Microwave System	76
	3.6.2	Targeted Sensitivity	77
	3.6.3	Scaling Up	79
	3.7	Conclusion	80

Chapter 4	Two-photon Excited Optical Detection of Magnetic Resonance of Nitrogen Vacancy Ensembles	81
4.1	Overview	81
4.2	Introduction	81
4.3	Theory	82
4.4	Experiments	84
4.4.1	Emission Spectra	85
4.4.1.1	Experimental Setup	85
4.4.1.2	Results	87
4.4.2	Fluorescence as a function of excitation power	91
4.4.2.1	Experimental Setup	91
4.4.2.2	Results	92
4.4.3	Two-photon Excited ODMR (2PODMR)	95
4.4.3.1	Experimental Setup	95
4.4.3.2	Results	97
4.5	Discussion	100
4.6	Conclusion	103
Chapter 5	Stimulated Emission from Nitrogen Vacancy Ensembles in Bulk Diamond	105
5.1	Overview	105
5.2	Introduction	106
5.2.1	Diamond Samples	107
5.3	Experiments	108
5.3.1	Attempts to Measure Stimulated Emission under 532 nm Excitation	109
5.3.1.1	Theory	109
5.3.1.1.1	Reference Sample	113
5.3.1.2	Experimental Design	114
5.3.1.3	Experimental Setup	117
5.3.1.4	Results	119
5.3.1.4.1	Titanium:sapphire	119
5.3.1.4.2	Diamond Sample #1	121
5.3.1.4.3	Diamond Sample #2	123

	5.3.1.5 Discussion	125
	5.3.1.6 Conclusion	130
5.3.2	Attempts to Measure Stimulated Emission Under 637 nm Excitation	131
	5.3.2.1 Introduction	131
	5.3.2.2 Experimental Setups	132
	5.3.2.3 Results	136
	5.3.2.3 Discussion	139
	5.3.2.4 Conclusion	140
5.3.3	Attempts to Measure ODMR using Stimulated Emission	141
	5.3.3.1 Introduction	141
	5.3.3.2 Theory	141
	5.3.3.3 Experimental Setup	144
	5.3.3.4 Results	147
	5.3.3.4.1 Diamond Sample #1	150
	5.3.3.4.2 Diamond Sample #2	152
	5.3.3.5 Discussion	154
	5.3.3.6 Conclusion	157
5.4	Conclusion	158
Chapter 6	Conclusion	160
References		165
Appendices		178
Appendix 1	MATLAB code to acquire and average magnetometry data	178
Appendix 2	MATLAB code to perform negative feedback	180

List of Figures

- Figure 1 – Motor neuron (based on [8]) and NV centre doped nanodiamond located on the axon (not to scale). Action potentials travel from the cell body to the axon terminal along the axon. The inset shows a simulated magnetic signal during an action potential (reproduced and adapted from [9]). 2
- Figure 2 – a) System capable of using NV centre doped nanodiamonds to measure action potentials in neuronal samples - measurements are made by applying resonant microwaves whilst exciting fluorescence with a 532 nm laser and imaging it with a high-speed camera. b) Depiction of a typical neuronal sample loaded with nanodiamonds - not to scale. 4
- Figure 3 – Excised marine worm axon (reproduced and adapted from [15]) with microdiamond placed on the axon. Action potentials can propagate in either direction along the axon. 5
- Figure 4 – Measured marine worm action potential and associated magnetic field (reproduced and adapted from [15]). 6
- Figure 5 – Single nitrogen-vacancy centre – carbon contributing electrons to NV centre are in red, non-contributing carbon atoms are in pink, N stands for nitrogen and V for vacancy - based on [56]. 12

Figure 6 –	Four possible orientations of NV centre and their intrinsic spin quantisation axes - based on [56].	13
Figure 7 –	a) NV visible emission spectra under 532 nm excitation (reproduced and adapted from [22]). b) NV ⁻ and c) NV ⁰ electronic structures - fluorescent transitions are shown with arrows – diagram not to scale - based on [28, 55].	15
Figure 8 –	Optical transitions between the ³ A ₂ and ³ E states are resonant on the zero-phonon line (ZPL) or off-resonant on the phonon sidebands (PSB) – based on [78-80].	16
Figure 9 –	³ A ₂ fine structure with ¹⁴ N hyperfine structure. The allowed transitions are shown with black arrows. A small axial magnetic field is applied, E = 0 and the nuclear Zeeman interaction is omitted - diagram not to scale - based on [50, 55].	18
Figure 10 –	Zeeman shifts cause the energy separation of the NV ⁻ spin states to vary as a function of external magnetic field.	19
Figure 11 –	NV centre is sensitive to the magnetic field projection onto the z-axis - based on [79].	21

- Figure 12 – Zeeman shifts for:
a) a single NV centre - spectrum reproduced and adapted from [83], b) a single crystal ensemble - spectrum reproduced and adapted from [30], magnetic field applied in an arbitrary direction, c) an aggregate/powder - based on [84], spectra reproduced and adapted from [85] - spectra are from 0 to 40 Gauss.
- 22
- Figure 13 – Mechanism of spin contrast and optical spin polarisation. NV centres optically cycle on the $^3A_2 \leftrightarrow ^3E$ transition. Spin state dependant ISC (intersystem crossing) rates cause spin polarisation into the $m_s=0$ state - based on [50].
- 24
- Figure 14 – Plot of single hyperfine ODMR feature centred at $\omega_0=2\pi*3$ GHz with $C = 0.1$, $\text{Flumax} = 1$ and $\Gamma = 2.2$ MHz.
- 26
- Figure 15 – Scanning magnetic imaging setup. NV centre is attached to an AFM (atomic force microscope) probe and read-out optically. By scanning the tip or sample, magnetic imaging can be achieved.
- 30
- Figure 16 – Widefield fluorescence imaging / point-measurement ODMR setup. Pump laser is reflected off the diamond to minimise sample heating. Laser induced fluorescence is collected and either imaged onto a camera or photodetector.
- 32

- Figure 17 – Probe absorption ODMR setup. 1042 nm probe is overlapped with a 532 nm pump laser and passed through a diamond sample containing NV centres. The probe is subsequently filtered from the pump and measured with a photodetector. 34
- Figure 18 – Photoelectric detection of magnetic resonance setup. Magnetic resonance is measured using electrodes placed on the diamond. These measure photo-ionisation currents whilst microwaves and optical excitation are applied to the diamond. 35
- Figure 19 – Photoionisation and recombination processes of the NV centre:
 1 – one-photon ionisation [57]
 2 – two-photon ionisation via excited triplet state [55, 57]
 3 – ionisation via excited state tunnelling [55, 81]
 4 – ionisation via singlet state [127]
 5 – two-photon recombination [55, 57]
 6 – one-photon recombination via tunnelling [55]
 Ground state tunnelling [124, 128] has been omitted for clarity. 37
- Figure 20 – Simplified experimental setup for magnetometry. Microwaves are applied, and fluorescence is excited with a 532 nm laser and collected with an objective lens. A lock-in amplifier is used to convert the measured fluorescence signal into a magnetometry signal. 41
- Figure 21 – a) Plot of single hyperfine ODMR feature with $\omega_0 = 2\pi \cdot 3$ GHz, $C = 0.1$, $F_0 = 1$ and $\Gamma = 2.2$ MHz and b) corresponding lock-in amplifier output with $\omega_{Dev} = \Gamma/(2\sqrt{3})$ - based on [15]. 43

Figure 22 –	a) Plot of three hyperfine transition ODMR feature with $\omega_0 = 2\pi \cdot 3$ GHz, $C = 0.1$, $F_0 = 1$ and $\Gamma = 2.2$ MHz and b) same resonance measured with multi-frequency excitation with $\omega_{Dev} = \Gamma/(2\sqrt{3})$ – based on [15].	44
Figure 23 –	Plot of lock-in amplifier output with three hyperfine resonances and multi-frequency excitation with $\omega_0 = 2\pi \cdot 3$ GHz, $C = 0.1$, $F_0 = 1$ and $\Gamma = 2.2$ MHz and $\omega_{Dev} = \Gamma/(2\sqrt{3})$ – based on [15].	45
Figure 24 –	Magnetometry experimental setup. Microwave signal components are generated with signal generators, mixed, filtered and applied to an NV centre doped diamond. Fluorescence is excited with a 532 nm laser, collected with an objective lens and measured with a photodetector. The fluorescence signal is processed by a lock-in amplifier to produce the magnetometry signal.	48
Figure 25 –	Photograph of magnetometer.	49
Figure 26 –	Microstrip microwave antenna.	53
Figure 27 –	Microstrip transmission line. Front facing view.	53
Figure 28 –	Circuit diagram for division detector, 100nF capacitors on all power rails have been omitted for clarity. Circuit consists of two transimpedance amplified photodiodes connected to an	

	analog division integrated circuit. The entire circuit is powered by four 9 V batteries.	55
Figure 29 –	PCB of division detector with all components except the photodiodes.	56
Figure 30 –	Division detector box.	56
Figure 31 –	Arrangement showing wire used to generate magnetic fields sitting on the antenna, in contact with the microdiamond.	57
Figure 32 –	Micrographs showing the microdiamond in contact with the wire at different focal planes, approximate beam placement and size shown by red spot in b).	58
Figure 33 –	ODMR contrast as a function of sample position on antenna. 2 mW of optical excitation and full microwave power was used in these measurements.	60
Figure 34 –	ODMR contrast as a function of microstrip width. 2 mW of optical excitation and full microwave power was used in these measurements.	61
Figure 35 –	ODMR contrast as a function of microwave power out of signal generator. 2 mW of optical excitation was used in these measurements.	62

Figure 36 –	ODMR spectra using amplitude modulation of the microwaves and a single microwave frequency. 2 mW of optical excitation was used in these measurements.	63
Figure 37 –	ODMR spectroscopy using frequency modulation of the microwaves and a single microwave frequency. 2 mW of optical excitation was used in these measurements.	64
Figure 38 –	ODMR spectroscopy using multi-frequency excitation and amplitude modulation of the microwaves. 2 mW of optical excitation was used in these measurements.	65
Figure 39 –	ODMR spectroscopy using multi-frequency excitation and frequency modulation of the microwaves. 2 mW of optical excitation was used in these measurements.	66
Figure 40 –	ODMR contrast as a function of optical power at the sample. Full microwave power was used in these measurements.	67
Figure 41 –	Magnetometric sensitivity as a function of optical power. Full microwave power was used in these measurements.	68
Figure 42 –	Magnetometric sensitivity as a function of microwave power. 2 mW optical excitation was used in these measurements.	69

Figure 43 –	Measurement of magnetometer bandwidth. Full microwave power and 2 mW of optical excitation was used for these measurements.	70
Figure 44 –	Demonstration of bandwidth by measuring a 500 Hz square wave magnetic field modulation. Full microwave power and 2 mW of optical excitation was used for these measurements.	71
Figure 45 –	Measurement of a repeated magnetic field modulation - number of measurements averaged = 4282408. Full microwave power and 2 mW of optical excitation was used for these measurements.	73
Figure 46 –	RMS voltage of noise as a function of number of magnetometry measurements averaged. Full microwave power and 2 mW of optical excitation was used for these measurements.	74
Figure 47 –	Minimum detectable magnetic field as a function of averaging time. Full microwave power and 2 mW of optical excitation was used for these measurements.	75
Figure 48 –	Proposed mechanism of two-photon excited fluorescence of NV ⁻ - excitation is via the phonon sideband (PSB) - zero-phonon line (ZPL) also shown - (based on [18, 78-80, 147]).	82

- Figure 49 – Proposed mechanism for two-photon excited optical spin polarisation. NV centres are expected to optically cycle on the ${}^3A_2 \leftrightarrow {}^3E$ transition and spin state dependant ISC (intersystem crossing) rates to cause spin polarisation into the $m_s=0$ state - based on [18, 50, 147, 153]. 84
- Figure 50 – Experimental setup used to measure emission spectra. 1064 and 532 nm lasers are combined with a long pass filter and coupled into a microscope. These are used to separately excite fluorescence from an NV centre doped diamond sample. Fluorescence is collected with an objective lens, long and short pass filtered to remove excitation wavelengths, and measured with a spectrometer. 86
- Figure 51 – Normalised emission spectra under CW 532 nm and fs-pulsed 1064 nm excitation. 88
- Figure 52 – Difference of CW 532 nm and fs-pulsed 1064 nm excitation spectra at different fluorescence rates. High, medium and low refer to the excitation powers shown in Figure 51. 89
- Figure 53 – Difference of emission spectra at high and low power of CW 532 nm and fs-pulsed 1064 nm excitation. High and low refer to the powers used in Figure 51. 90

- Figure 54 – Experimental setup used to measure the dependence of the fluorescence rates on excitation power. 1064 and 532 nm lasers are combined with a long pass filter and coupled into a microscope. Fluorescence is collected with an objective lens, filtered with long and short pass filters and measured with a photodiode. Optical powers are monitored with beam pick-offs measured with photodiodes. 91
- Figure 55 – Fluorescence as a function of excitation power under fs-pulsed 1064 nm excitation. Measured using setup shown in Figure 54 – limited range fitted using Equation 30. The same y-data is plotted on a) with power on the x-axis and b) with power squared on the x-axis. 93
- Figure 56 – Fluorescence as a function of excitation power under CW 532 nm excitation. 95
- Figure 57 – Experimental setup used to measure 2PODMR. 1064 and 532 nm lasers are combined with a long pass filter and coupled into a microscope. Fluorescence is collected with an objective lens, filtered with long and short pass filters and measured with a photodiode. ODMR spectra are produced by applying and sweeping microwaves whilst measuring laser induced fluorescence. The fluorescence signal is processed by a lock-in amplifier, referenced to the microwave modulation rate, to produce the ODMR spectra. 96
- Figure 58 – One-photon excited ODMR and 2PODMR measured at the same fluorescence rate. Measured with 557 mW of 1064 nm and 26 μ W of 532 nm excitation at the sample. 98

Figure 59 –	One-photon excited ODMR and 2PODMR at the same fluorescence rate on separate y-axes. Same data as Figure 58.	99
Figure 60 –	a) Excitation via the phonon sideband (based on [78]). A 532 nm photon excites the NV centre first to $ 3\rangle$ before it decays to $ 2\rangle$. b) Process of stimulated emission (based on [78, 142, 168]) – stimulating photon causes de-excitation of an NV centre and the emission of a photon pair.	109
Figure 61 –	Expected gain as a function of pump power for diamond sample with an NV ⁻ concentration of 0.5 ppm.	113
Figure 62 –	Simplified experimental setup for measurements of a change in probe power. Pump and probe beams are combined using a dichroic mirror, passed through the sample, and the probe measured after separation from the pump.	114
Figure 63 –	Normalised probe and pump power as a function of time before passing through the sample.	115
Figure 64 –	Expected experimental output – 10% relative gain. Probe power is expected to increase in phase with the pump power due to stimulated emission.	116

Figure 65 –	Experimental setup used to measure stimulated emission with a 532 nm pump wavelength. Modulated pump and probe beams are combined using a dichroic mirror, passed through the sample, and the probe measured with a photodiode after separation from the pump using a prism. Modulation of the pump is achieved using an optical chopper, and the probe using an acousto-optical modulator. Demodulation of the probe is achieved using a lock-in amplifier referenced to the probe modulation rate and is recorded with an oscilloscope.	117
Figure 66 –	Measurement of relative gain using titanium:sapphire.	119
Figure 67 –	Measurement of relative gain as a function of probe power. 1.25 W pump power was used.	120
Figure 68 –	Change in probe power as a function of time –probe wavelength of 723 nm and power of 5 mW was used.	121
Figure 69 –	Change in probe power as a function of pump power with a) 723, b) 820 and c) 950 nm probes.	122
Figure 70 –	a) Change in probe power as a function of probe power with 723 nm probe (0.72 W pump), b) 820 nm probe (0.58 W pump) and c) 950 nm probe (0.45 W pump).	122
Figure 71 –	Change in probe power as a function of time (512 averaged) with a) 723, b) 820 and c) 950 nm probes, all at 400 mW.	123

Figure 72 –	Change in probe power as a function of pump power with a) 723, b) 820 and c) 950 nm probes.	124
Figure 73 –	Change in probe power as a function of probe power with a) 723 nm probe (1.2 W pump), b) 820 nm probe (1.15 W pump) and c) 950 nm probe (1.44 W pump).	124
Figure 74 –	a) Change in probe power as a function of time (512 averaged) with 723 nm at 5 mW, b) 820 nm at 800 mW and c) 950 nm at 400 mW probes.	125
Figure 75 –	Experimental setup for measurements of probe power as a function of time. Modulated pump and probe beams are combined using a cold mirror, passed through the sample, and the probe measured with a photodiode after separation from the pump using a prism. Modulation of the pump is achieved using an optical chopper, and the probe using the laser diode driver. Demodulation of the probe is achieved using a lock-in amplifier referenced to the probe modulation rate and recorded with an oscilloscope. Optical powers are monitored using beam pick-offs measured with photodiodes.	133

Figure 76 –	Experimental setup for measurements as a function of pump and probe power. Modulated pump and probe beams are combined using a cold mirror, passed through the sample, and the probe measured with a photodiode after separation from the pump using a prism. Modulation of the pump is achieved using an optical chopper, and the probe using the laser diode driver. Probe signal amplitude at the pump modulation rate is measured using a lock-in amplifier and recorded with an oscilloscope. Optical powers are monitored using beam pick-offs measured with photodiodes.	135
Figure 77 –	Change in probe power as a function of pump power.	137
Figure 78 –	Change in probe power as a function of probe power with pump power at 120 mW.	138
Figure 79 –	Change in probe power as a function of time at 120 mW pump and 0.31 mW probe power (512 averaged).	139
Figure 80 –	Simplified experimental setup to measure probe beam ODMR. Pump and probe beams are combined with a dichroic mirror and passed through an NV centre doped diamond sample. Modulated microwaves are applied to the sample and their frequency swept. The pump and probes are separated using a prism and the probe measured with a photodiode connected to a lock-in amplifier. This is referenced to the modulation rate of the microwaves to enable extraction of the ODMR signal.	142
Figure 81 –	Plot of ΔP vs. C_p/C based on the proposed model (Equation 40).	

Figure 82 – Experimental setup used to measure probe beam ODMR. Pump and probe beams are combined with a dichroic mirror and passed through an NV centre doped diamond sample. Modulation of the probe is achieved with an AOM. Frequency swept microwaves are modulated using a microwave switch and applied to the sample after amplification. The pump and probes are separated using a prism and the probe measured with a photodiode connected to a lock-in amplifier referenced to the probe modulation rate. The demodulated signal is fed into a second lock-in amplifier referenced to the microwave modulation rate to extract the ODMR signal. This is recorded with an oscilloscope.

145

Figure 83 – ODMR amplitude as a function of distance from the sample. 1.75 W of pump power was used and ~1 mW of probe power. Measurements were made with diamond sample #2.

148

Figure 84 – ODMR contrast as a function of a) pump power and b) probe power at 723 nm (0.5 W of pump power was used). Measurements were made with diamond sample #2.

149

Figure 85 – Probe beam ODMR contrast as a function of a) pump power (probes at 5 mW) and b) probe power (pump at 0.5 W).

150

Figure 86 – Probe beam ODMR Spectra with probe at a) 723 nm (1 mW probe and 0.72 W pump), b) 820 nm (5 mW probe and 0.58 W pump) and c) 950 nm (1 mW probe and 0.5W pump).

151

Figure 87 –	Fluorescence ODMR Spectra – a), b) and c) correspond to those measured simultaneously with a), b) and c) from Figure 86. Pump power of 0.5 W used.	151
Figure 88 –	Probe beam ODMR contrast as a function of a) pump power (probes at 5 mW) and b) probe power.	152
Figure 89 –	Probe beam ODMR spectra with probe at a) 723 nm (3 mW probe and 1.2 W pump), b) 820 nm (3 mW probe and 1.15 W pump) and c) 950 nm (5 mW and 1.44 W pump).	153
Figure 90 –	Fluorescence ODMR spectra – a), b) and c) correspond to those measured simultaneously with a), b) and c) from Figure 89. Pump power of 1.5 W used.	154

List of Tables

Table 1 – List of sensitivities achieved for different detectors - each detector was tested 10 times with 1, 10, and 100 s measurements of 500 nT, 1 kHz sinusoidal magnetic fields and the standard deviation calculated.

72

Table 2 – Diamond Specifications: N_s = substitutional nitrogen, NVN = nitrogen-vacancy-nitrogen, V⁰ = neutral vacancy - data provided by the Institute of Photonics (University of Strathclyde).

108

List of Abbreviations

2PODMR – two-photon excited optical detection of magnetic resonance

AC – alternating current

ADC – analog-to-digital converter

AOM – acousto-optic modulator

CMOS – complementary metal-oxide-semiconductor

CVD – chemical vapour deposition

CW – continuous wave

CW-ESR – continuous wave electron spin resonance

DC – direct current

FWHM – full-width-half-maximum

HPHT – high-pressure high-temperature

ISC – inter-system crossing

NA – numerical aperture

Ns – substitutional nitrogen

NV – nitrogen-vacancy / nitrogen-vacancy centre

NV⁻ – negatively charged nitrogen-vacancy centre

NV⁰ – neutral nitrogen-vacancy centre

NVN – nitrogen-vacancy-nitrogen

ODMR – optical detection of magnetic resonance

PCB – printed circuit board

PSB – phonon sideband

SNR – signal-to-noise ratio

STED – stimulated emission depletion

TIA – transimpedance amplified / transimpedance amplifier

TTL – transistor-transistor logic

UV – ultraviolet

V⁰ – neutral vacancy

ZPL – zero-phonon line

Chapter 1

Introduction

Since the early 2000s, research into fluorescent atom-like defects in diamond, called nitrogen-vacancy centres (NV centres), has dramatically increased. This has been driven by the discoveries that single NV centres can be measured using confocal microscopy, used as a single photon emitter and have magnetically sensitive spin states that can be optically polarised at room temperature [1]. Furthermore, microwave excitable transitions between the NV centre spin states were found to be optically detectable due to spin-state dependent fluorescence rates [1]. Using this principle, high sensitivity, nanoscale magnetometry with NV centres was proposed [2]. Furthermore, as the spin state can be controlled coherently [3], quantum logic operations are possible using NV centres and can be repetitively read-out using proximal nuclear spins [4]. In future, this may lead to quantum information processing using NV centres as qubits [4].

In 1995, diamond was also shown to be as bio-compatible as commonly used medical implant materials such as titanium and stainless steel [5]. Later work showed fluorescent nanodiamonds, which are nanoscale diamond crystals doped with NV centres, are biocompatible at the cellular level [6].

Given the biocompatibility of diamond and the ability to measure the NV centre's spin state, it was realised that fluorescent nanodiamonds could be used to make biologically

relevant measurements such as nanoscale-thermometry and nuclear magnetic resonance [7]. One particularly interesting avenue of research is that of the sensing of electrical impulses generated by neurons.

Although there are many types of neurons, they commonly possess dendrites, a cell body, an axon and axon terminals [8], as depicted in Figure 1.

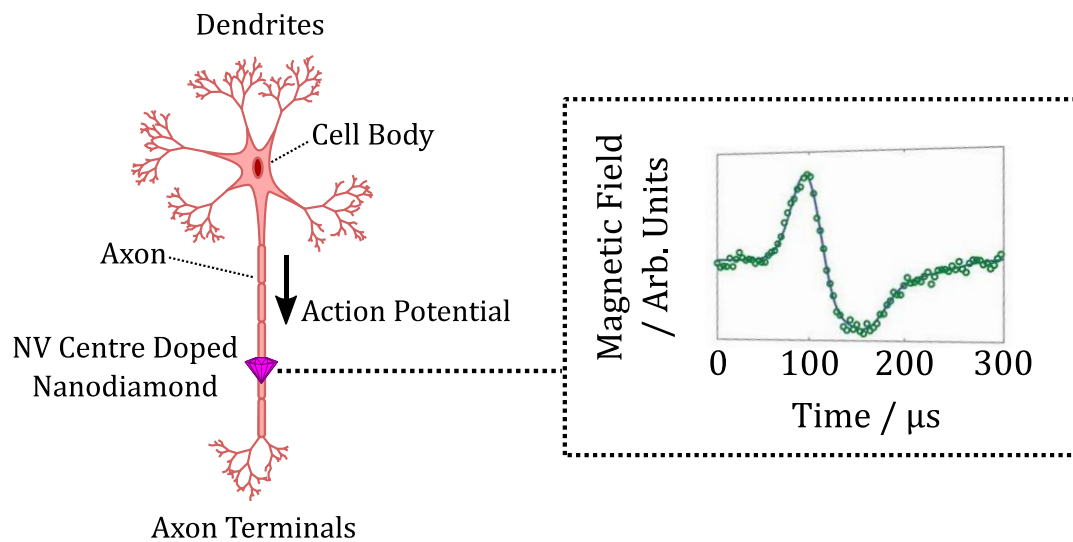


Figure 1 – Motor neuron (based on [8]) and NV centre doped nanodiamond located on the axon (not to scale). Action potentials travel from the cell body to the axon terminal along the axon. The inset shows a simulated magnetic signal during an action potential (reproduced and adapted from [9]).

The dendrites receive chemical signals from other neurons and convert them into electrical signals [8]. These serve to reduce the electrical potential between the inside and outside of the cell (membrane potential) [8]. Once a threshold is reached, a rapid increase and decrease of the membrane potential occur before it returns to its resting value [8]. This voltage fluctuation is called an action potential [8]. It travels down the

neuron's axon towards the axon terminals (Figure 1) where it initiates the release of calcium ions to facilitate communication with other neurons or cells [8]. A simulated magnetic field generated by a single neuronal action potential is shown in Figure 1 and experimentally measured marine worm action potentials and magnetic field fluctuations are shown in Figure 4.

Currently, action potentials are measured either using microelectrodes [9], patch clamp techniques [8] or optically using voltage-sensitive [10] or calcium-indicating [11] fluorescent dyes. Microelectrodes and patch-clamp techniques both have excellent signal-to-noise ratios. However, patch-clamp techniques require a separate probe per neuron, which limits scaling-up. Microelectrode arrays are currently limited to a ~ 20 μm spatial resolution [9].

Both voltage-sensitive and calcium-indicating fluorescent dyes allow multiplexed imaging of individual action potentials. However, voltage-sensitive dyes have a poor signal-to-noise ratio and cannot be used for long-term studies due to their toxicity [10]. Calcium-indicating dyes exhibit poor temporal resolution with single (~ 2 ms [10]) action potentials causing fluorescence changes of 100s of milliseconds [12]. Furthermore, chemical dyes can exhibit an irreversible quenching of fluorescence (photobleaching), when in the excited state [13].

NV centres in diamond can potentially address all of these issues as they are non-toxic [6] and do not photobleach [7]. They have also been theoretically shown to be sensitive enough to extracellularly measure the magnetic field fluctuation associated with single neuronal action potentials [10]. A long-term goal of this research is to provide a microscope system capable of simultaneous, real-time detection of thousands of

individual action potentials. This would be a considerable technological step forward as there is currently no instrument capable of such measurements [14]. Figure 2a shows a system potentially capable of this.

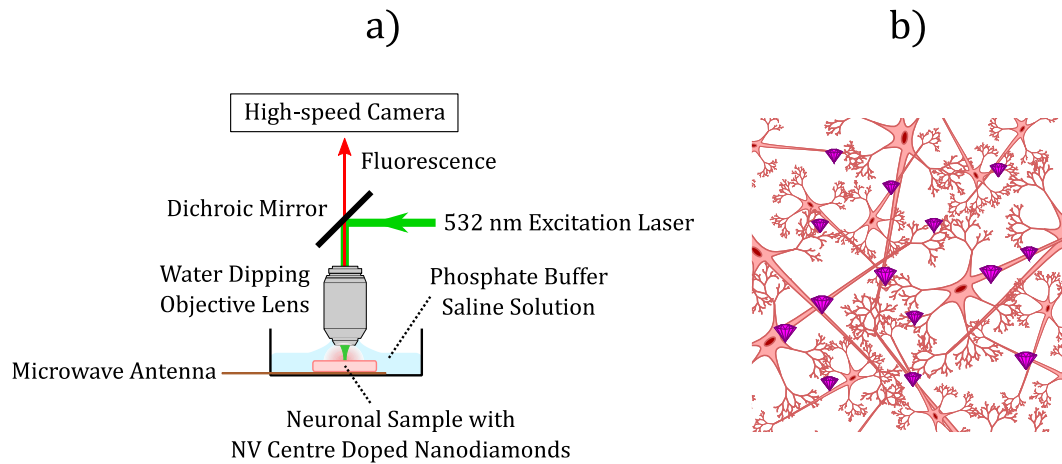


Figure 2 – a) System capable of using NV centre doped nanodiamonds to measure action potentials in neuronal samples - measurements are made by applying resonant microwaves whilst exciting fluorescence with a 532 nm laser and imaging it with a high-speed camera. b) Depiction of a typical neuronal sample loaded with nanodiamonds - not to scale.

A fluorescence microscope with a water-dipping lens would be used to perform live cell imaging on a neuronal sample containing nanodiamonds (Figure 2b). Imaging would be performed in a phosphate-buffered saline solution to maintain bio-compatible conditions. Microwaves resonant with the NV centres would be applied and the fluorescence imaged at sufficiently high frame-rates to detect the changes in NV centre fluorescence associated with action potentials.

The original short-term goal of this research was to measure the action potential transmitted along an excised marine worm axon (Figure 3). The aim was to provide a proof-of-concept measurement of a live action potential using NV centres.

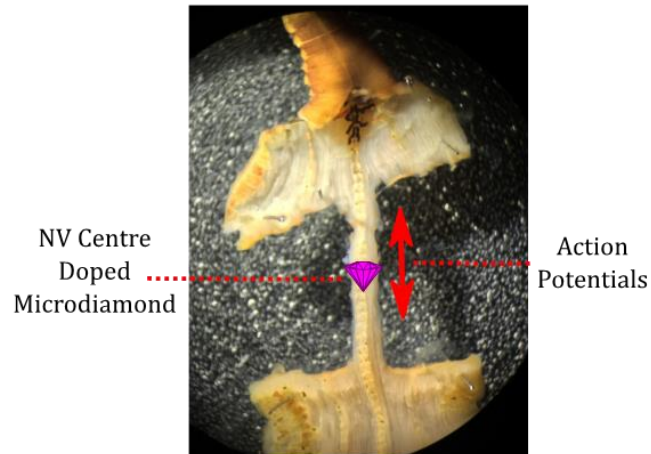


Figure 3 – Excised marine worm axon (reproduced and adapted from [15]) with microdiamond placed on the axon. Action potentials can propagate in either direction along the axon.

Marine worms provide a large (~0.5 mm), robust axon and can be stimulated to transmit action potentials on demand. This has been possible to measure since the 1960s [15]. Whilst this PhD was being undertaken, a measurement of a marine worm action potential was successfully performed using NV centres in bulk diamond [16], as shown in Figure 4. The experimental design used to achieve this is discussed in Section 2.2.7.

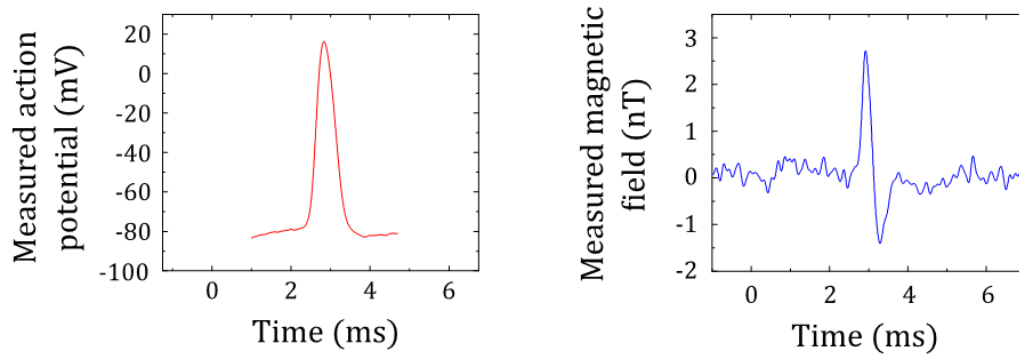


Figure 4 – Measured marine worm action potential and associated magnetic field (reproduced and adapted from [15]).

Two-photon excited fluorescence from NV centres has also been demonstrated [17]. This has several advantages over single-photon excitation when performing microscopy on live biological specimens. These include increased imaging depth and, due to an inhibition of fluorescence outside of the focal plane, reduced phototoxicity when performing 3D imaging [18]. Previous to this research, optical detection of the NV centre spin state had not been demonstrated under two-photon excitation.

NV centres in diamond have also been proposed as a laser gain material in the visible range due to the high thermal conductivity, low thermal expansion and high damage threshold of diamond [19, 20]. In particular, given the broad emission spectrum of NV centres, they may find use as the gain material in femtosecond and wavelength tunable lasers [21]. Previous research has demonstrated laser action using another defect in diamond [19], called the H3 defect, and a recent study has reported stimulated emission from NV centres [22]. Given the ability to measure magnetic fields with NV centres, a magneto-sensitive NV laser with the ability to perform ultra-sensitive magnetometry has recently been proposed [23]. This is a second long-term goal of this research.

With this in mind, there are three aims of the research presented in this thesis:

1. To build and quantify the sensitivity of a fluorescence microscopy system capable of magnetometry with NV centre ensembles
2. To ascertain whether two-photon excitation of NV centres allows magnetometry to be performed in a similar microscopy setup
3. To quantify the optical gain due to stimulated emission from mm-scale, NV doped diamond samples and to demonstrate the ability to use stimulated emission for magnetometry

The background and theory of diamond and nitrogen-vacancy centres are discussed in Chapter 2, the experiments performed to accomplish the listed aims are discussed in Chapters 3-5 and the conclusions of the research are presented in Chapter 6.

Chapter 2

Background and Theory

2.1 – Diamond

Diamond is a well-known allotrope of carbon and renowned for its outstanding material properties. It is one of the hardest substances on earth owing to its dense, strong bonding [24, 25] and is regularly used in industry for cutting, polishing and drilling glass, rock and gems [25-27]. Pure diamond is also optically transparent due to its wide band gap of 5.47 eV [28]. It transmits over a broad wavelength range from 226 nm to 500 μm excluding a region around 2.5-6.5 μm due to two and three phonon absorption [24]. However, its transmittance is reduced by its high refractive index of 2.43 (at 532 nm) [29]. This causes a reflection of $\sim 17\%$ at normal incidence in air [30].

There are two abundant isotopes of carbon, ^{12}C and ^{13}C , with natural concentrations of $\sim 98.1\%$ and $\sim 1.1\%$ respectively [31, 32]. ^{12}C exhibits no nuclear spin ($I=0$) [31] whereas ^{13}C exhibits a nuclear spin of $I=1/2$ [32], where I is the nuclear spin quantum number. As ^{13}C has nuclear spin, it is paramagnetic, and can be a major source of decoherence in NV centre experiments. However, isotope concentration is controllable in synthetic diamond [33-35].

One of the most exciting properties of diamond is its biocompatibility. Non-toxicity, bio-conjugation and the uptake of nanodiamonds in living cells have been demonstrated in the past decade [6, 36, 37]. This has led to the use of fluorescent nanodiamonds in super-resolution imaging [38], magnetic imaging [39] and nanometre-scale thermometry [40] experiments with living cells. In future, they may also be used as biomarkers for long-term tracking or as vehicles for advanced drug delivery [28].

2.1.1 - Diamond Synthesis

Although natural diamond can contain NV centres, synthetic diamond is commonly used in experiments to allow the defect concentration to be controlled and to allow reproducibility [30]. Synthetic diamond production began in the 1950s with a technique called high pressure/high temperature (HPHT) [41, 42]. Over time, further methods such as chemical vapour deposition (CVD) created the ability to perform controlled doping of diamond with various impurities during growth. Both types of diamond are used in experiments described in this thesis.

2.1.1.1 - High Pressure / High Temperature (HPHT)

Fundamentally, HPHT synthesis converts graphite to diamond by increasing the temperature and pressure of the sample's environment [43, 44]. This makes diamond thermodynamically favourable and causes a phase transition to occur [44]. Although graphite is more stable than diamond at room temperature, a large activation energy prevents it from converting back [45].

HPHT synthesis is the dominant manufacturing method for abrasive and cutting applications [46]. These diamonds are also used to produce commercial microdiamonds and nanodiamonds containing NV centres. The nanodiamonds are milled down from microdiamonds [28, 47, 48]. Isotopically purified samples (99.97% ^{12}C) can also be made using a purified carbon source [34]. The isotopically purified HPHT can contain 1.4 ppm of substitutional nitrogen [33] making it useful for nitrogen-vacancy ensemble applications. The best HPHT diamonds are also used as seeds for CVD diamond synthesis [42].

2.1.1.2 - Chemical Vapour Deposition (CVD)

Chemical vapour deposition creates diamonds via epitaxial growth on a substrate [42]. The process involves heating a mixture of hydrocarbons (typically methane) and molecular hydrogen in a reactor causing the molecules to disassociate and to form atomic hydrogen and hydrocarbon radicals [46]. These participate in chemical reactions on the seed diamond surface resulting in carbon deposition and diamond growth [46]. The chemical reactions and reactors are discussed in detail in the following references [42, 46, 49].

The majority of impurities in CVD diamond originate from the gases used in the growth process [24]. These gases are commercially available at contaminant levels below 1 ppm [24] allowing the creation of ultrapure diamond. Isotopically pure methane- ^{12}C can also be used to create an ultrapure and isotopically pure diamond capable of hosting nitrogen-vacancy centres with high room-temperature T_2^* (inhomogeneous electron-spin dephasing time) of 2 ms [35]. Under ideal conditions, this would allow single NV magnetometry with a sensitivity of $\sim 127 \text{ pT Hz}^{-1/2}$ [50] and could be

increased further using multi-pulse sequences to extend the coherence time [51]. By altering the amounts of N₂ gas added during growth, the concentration of doped nitrogen can also be controlled [31]. This is an attractive technique as substitutional nitrogen concentrations up to ~170 ppm [52, 53] or ~6.4 ppm in isotopically purified samples [54] have been achieved.

2.2 - Nitrogen-Vacancy Centres

2.2.1 - Structure

The nitrogen-vacancy (NV) centre is a useful defect in diamond. It is an atom-like system of electrons created when two adjacent carbon atoms in a diamond crystal have been substituted with a nitrogen atom and a vacant lattice site (vacancy) [50, 55, 56], as shown in Figure 5. There are at least two charge states, neutral and negatively charged [50, 55, 57], with some evidence of a non-fluorescing positively charged state [58, 59].

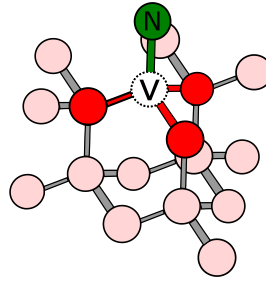


Figure 5 – Single nitrogen-vacancy centre – carbon contributing electrons to NV centre are in red, non-contributing carbon atoms are in pink, N stands for nitrogen and V for vacancy - based on [56].

The neutral state (NV^0) is made up of five electrons, two from the nitrogen atom and one from each of the three surrounding carbon atoms [50, 57]. The negatively charged state (NV^-) has one extra electron donated from elsewhere in the diamond, often presumed to be another substitutional nitrogen atom [50, 57]. Due to diamonds tetrahedral bonding, single NV centres can be orientated in one of four directions in the crystal, as shown in Figure 6. In ensembles, NV centres are usually equally distributed amongst all four orientations [53, 56].

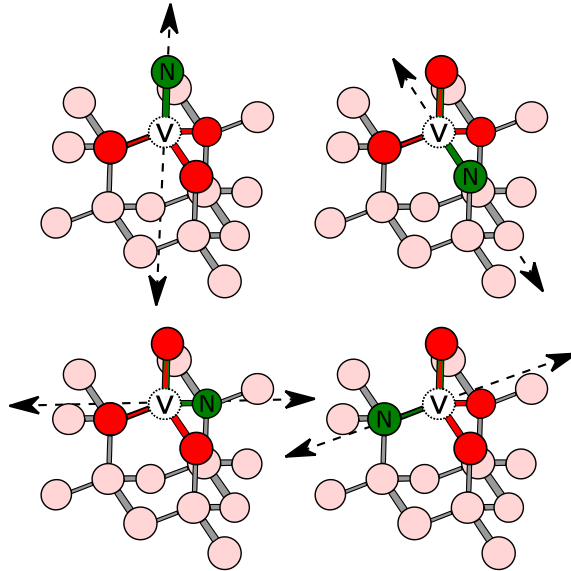


Figure 6 – Four possible orientations of NV centre and their intrinsic spin quantisation axes - based on [56].

2.2.2 - NV Centre Synthesis

NV centre synthesis is performed in three main stages: nitrogen incorporation, irradiation and annealing [42, 60, 61]. As described in Section 2.1.1, it is possible to incorporate nitrogen during diamond synthesis, otherwise, it can be added through nitrogen ion implantation [60, 62]. Vacancies are created in diamond by irradiation with electrons, hydrogen ions, helium ions or carbon ions [61]. Finally, the vacancies become mobile when annealed at high temperature (typically ≥ 800 °C [17, 47, 63]) allowing them to bind with the nitrogen atoms to form nitrogen-vacancy centres [31, 60].

2.2.3 - Optical Properties

NV centres have remarkable optical properties that make them of great interest for sensing applications whether in bulk or nanodiamond form. Unlike organic dyes commonly used in fluorescent microscopy, NV centres do not photobleach [11, 64-66]. They are therefore well suited to super-resolution techniques such as stimulated emission depletion microscopy [38, 67, 68], for long-term fluorescent tracking [38] or potentially as a laser gain material [21, 29]. Furthermore, fluorescence from a single NV centre can be measured using confocal microscopy at room temperature [69] and can be used as a single photon source [70, 71]. Individual NV centres from within a single nanodiamond can even be resolved using stimulated emission depletion (STED) microscopy [68, 72].

2.2.4 - Optical Transitions

Fluorescent transitions occur between electronic states of the NV centre, the nomenclature of which come from group theory. In this model, the combination of sp^3 orbitals from the contributory nitrogen and carbon atoms form NV molecular orbitals [28]. The letter and subscript number are known as the irreducible representation. Details of the molecular model can be found in a review by Doherty *et al* [73]. The superscript number refers to the spin multiplicity where 1 is a singlet, 2 is a doublet, 3 is a triplet and 4 is a quartet spin state. Both the NV⁻ ground (3A_2) and excited 3E states are spin triplets and can be measured optically [74, 75]. The energy levels of the NV⁰ and NV⁻ are shown in Figures 7b and 7c respectively.

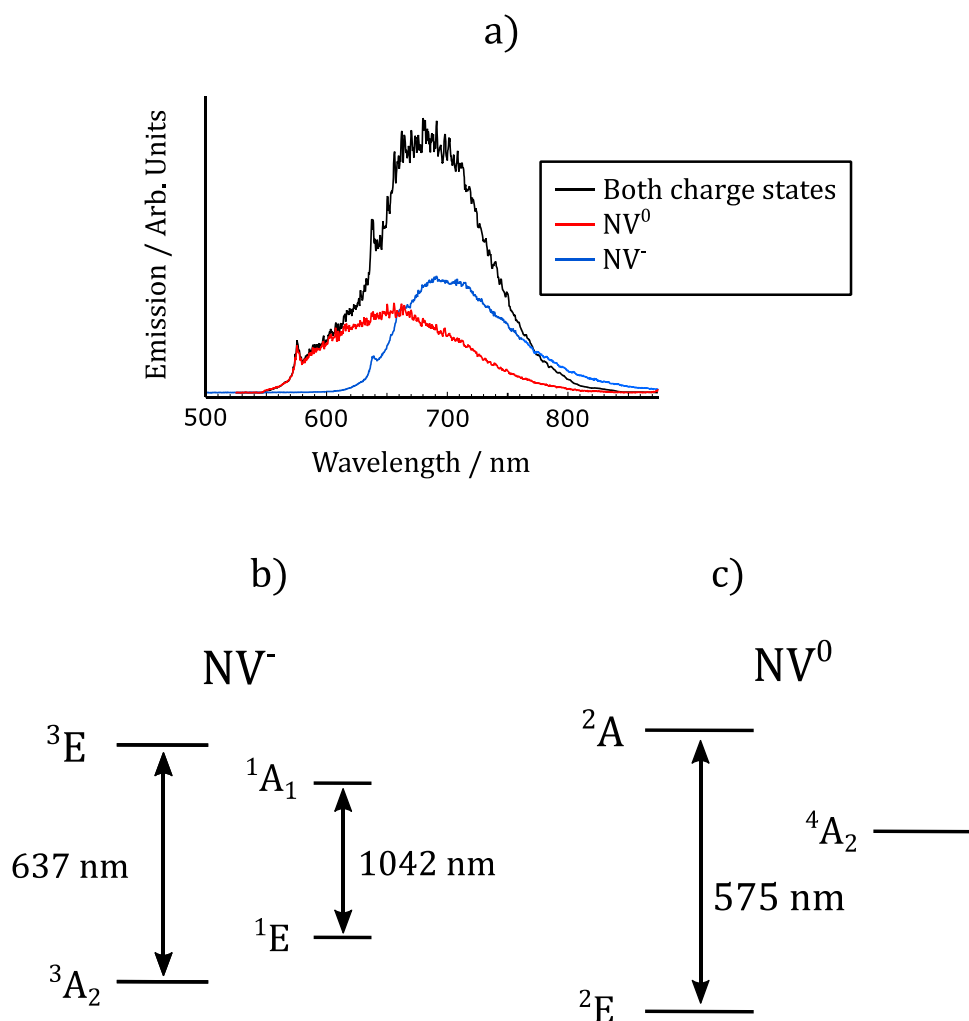


Figure 7 – a) NV visible emission spectra under 532 nm excitation (reproduced and adapted from [22]). b) NV^- and c) NV^0 electronic structures - fluorescent transitions are shown with arrows – diagram not to scale - based on [28, 55].

At room temperature, NV centres exhibit broad fluorescence spectra due to their phonon sidebands (PSB), the physics of which is described in detail in a review by Doherty *et al* [55]. In brief, PSB excitation involves excitation to a higher energy state, followed by fast thermal relaxation, as depicted in Figure 8. Phonon transitions are on

the time-scale of picoseconds [76] whereas optical transitions are on nanosecond time-scales (3E fluorescence lifetime is 13 ± 0.5 ns) [77].

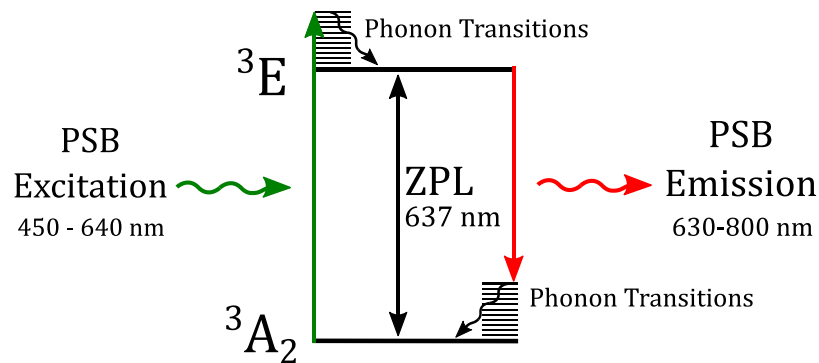


Figure 8 - Optical transitions between the 3A_2 and 3E states are resonant on the zero-phonon line (ZPL) or off-resonant on the phonon sidebands (PSB) – based on [78-80].

The NV^0 can be excited at a wavelength from about 400 to 580 nm [80] and emits from about 550 to 800 nm [22, 57]. The NV^- on the other hand, is excitable from about 450 to 640 nm [80] and emits from about 630 to 800 nm [22, 57]. Discrimination of charge states is possible with wavelength selective monitoring of NV fluorescence [57, 81] and near exclusive excitation of charge states is possible with narrowband excitation [80].

2.2.5 - Spin Transitions

Optical magnetometry with NV centres is fundamentally possible by monitoring magnetic dipole transitions within either of the NV^- triplet states. This process is called the optical detection of magnetic resonance (ODMR) and is facilitated by spin state dependent fluorescence rates. The spin contrast is defined as the fractional change of

the fluorescence rates between the $m_s = \pm 1$ and $m_s = 0$ states, where m_s is the electron spin projection quantum number. Because the spin contrast of the ground (3A_2) state is significantly higher than that of the excited (3E) state [74, 75], it is commonly used for magnetometry. The 3A_2 spin transitions can be described by the following Hamiltonian (in units of Hertz) [50, 79] :

$$H_{\text{total}} = H_{\text{spin}} + H_{\text{hyperfine}} + H_{\text{nuclear}} \quad (1)$$

where:

$$H_{\text{spin}} = DS_z^2 + E(S_x^2 - S_y^2) + g_s \mu_B \mathbf{B} \cdot \mathbf{S} \quad (2)$$

where D is the zero-field splitting, $\mathbf{S} = [S_x, S_y, S_z]$ is the electron spin operator, E is the transverse zero-field splitting, $g_s = 2.003$ [50] is the electron-spin g -factor, μ_B is the Bohr magneton, \mathbf{B} is the external magnetic field and:

$$H_{\text{hyperfine}} = A_{\parallel} S_z I_z + A_{\perp} (S_x I_x + S_y I_y) \quad (3)$$

where $A_{\parallel} = -2.16$ MHz [50] is the axial hyperfine constant, $\mathbf{I} = [I_x, I_y, I_z]$ is the dimensionless spin-projection operator for the nuclear spin [30], $A_{\perp} = -2.7$ MHz [50] is the transverse hyperfine constant, $\mathbf{I} = [I_x, I_y, I_z]$ is the dimensionless spin-projection operator for the nuclear spin [30], and:

$$H_{\text{nuclear}} = PI_z^2 - g_I \mu_N \mathbf{B} \cdot \mathbf{I} \quad (4)$$

where $P = 4.95$ MHz [50] is the quadrupole splitting parameter, $g_I=0.403$ [50] is the nuclear spin g-factor and μ_N is the nuclear magneton.

D , the zero-field splitting, causes separation of the $m_s=0$ and the $m_s=\pm 1$ states when no external magnetic field is applied. It is ~ 2.87 GHz at room temperature [50]. E , the transverse zero-field splitting, is intrinsically contributed by the crystal strain in the diamond and ranges from ~ 100 kHz in high purity CVD diamond, to a few MHz in nanodiamonds [79].

The z-axis is taken to be the intrinsic NV spin quantization axis (NV axis). It is the axis along which the nitrogen atom and vacancy are physically aligned in the lattice [79], as shown in Figures 6 and 11. A magnetic dipole transition, also known as a magnetic resonance or electron spin resonance (ESR), can be excited by a magnetic field oscillating perpendicular to this axis [61].

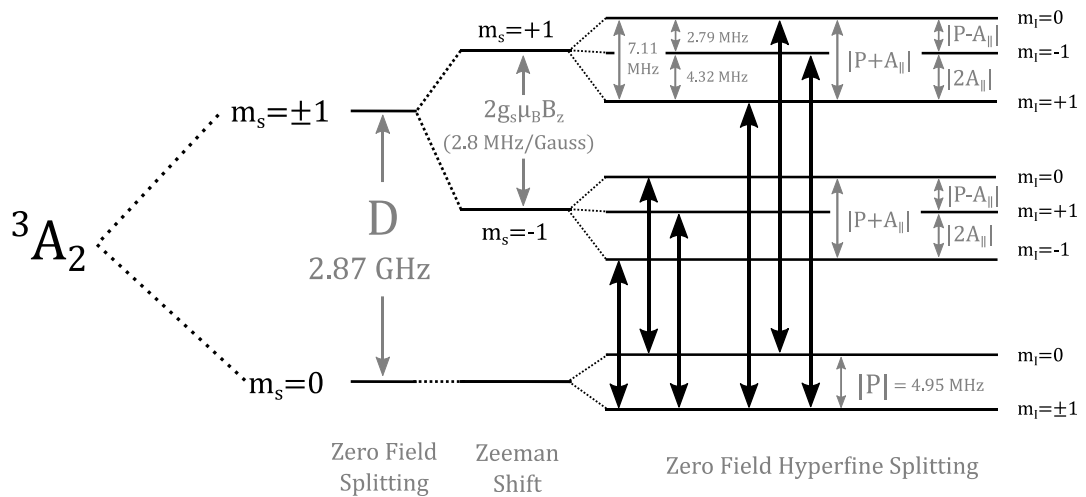


Figure 9 - 3A_2 fine structure with ^{14}N hyperfine structure. The allowed transitions are shown with black arrows. A small axial magnetic field is applied, $E = 0$ and the nuclear Zeeman interaction is omitted - diagram not to scale - based on [50, 55].

The 3A_2 state is coupled to the nucleus of the compositional nitrogen atom. For the abundant ${}^{14}\text{N}$ isotope, this gives rise to three hyperfine transitions per spin (m_s) transition with the $m_l=0$ hyperfine transitions being separated from the $m_l=\pm 1$ transitions by $\pm A_{\parallel}$, where m_l is the nuclear spin projection quantum number [50]. The magnetic dipole transitions obey the selection rules, $\Delta m_s = \pm 1$ and $\Delta m_l = 0$ [50]. The allowed ESR transitions are depicted in Figure 9.

The $g_s \mu_B \mathbf{B} \cdot \mathbf{S}$ and $g_I \mu_N \mathbf{B} \cdot \mathbf{I}$ terms indicate both the electron and nuclear spin states exhibit Zeeman shifts proportional to the applied magnetic field. These cause the energy separation between the spin states to be proportional to the external magnetic field, as shown in Figure 10. Because $g_I \mu_N \ll g_s \mu_B$ [50, 82], the nuclear spin Zeeman shift can usually be neglected.

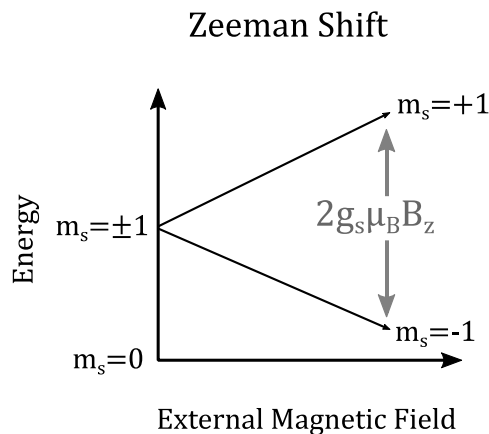


Figure 10 – Zeeman shifts cause the energy separation of the NV^- spin states to vary as a function of external magnetic field.

2.2.5.1 - Weak Magnetic Field Regime

The spin part of the Hamiltonian can be re-written (in Hz) [79]:

$$H_{\text{spin}} = H_{\parallel} + H_{\perp} + E(S_x^2 - S_y^2) \quad (5)$$

where:

$$H_{\parallel} = D_z^2 + g_s \mu_B B_z S_z \quad (6)$$

$$H_{\perp} = g_s \mu_B (B_x S_x + B_y S_y) \quad (7)$$

This separates the contributions parallel (H_{\parallel}) and perpendicular (H_{\perp}) to the NV axis and allows separation into weak and strong magnetic field regimes [79]. In this thesis, experiments are performed in the weak field regime, where $H_{\perp} \ll H_{\parallel}$. This is when $B_{\perp} = (B_x + B_y)^{1/2} \ll 100$ mT (1000 Gauss) and the Zeeman shifted ESR frequencies (in Hz) are given by [79]:

$$\nu_{\pm} = D \pm \sqrt{\left(\frac{g_s \mu_B B_z}{h}\right)^2 + E^2} \quad (8)$$

In this regime, the NV centre is sensitive only to the projection of the magnetic field onto the NV axis (B_z) and is insensitive to transverse magnetic fields, as depicted in Figure 11.

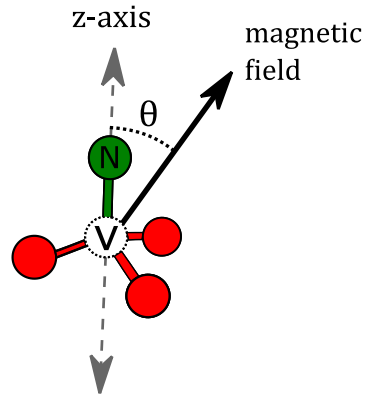


Figure 11 – NV centre is sensitive to the magnetic field projection onto the z-axis - based on [79].

Due to the E term in Equation 8, the ESR frequency is quadratically dependent on B_z unless $B_z \gg E$ [79]. In practice, this is achieved by adding a bias magnetic field such that $B_{Bias} \gg \frac{\hbar E}{g\mu_B}$, in which case the ESR frequency (in Hz) depends linearly on B_z and is approximated by [79]:

$$\nu_{\pm} \approx D \pm \frac{g_s \mu_B B_z}{h} \quad (9)$$

This allows high sensitivity magnetometry to be performed with $\frac{g_s \mu_B B_z}{h} \approx 2.8 \text{ MHz / Gauss}$.

The magnetic sensitivity along the NV axis has significant implications for the behaviour of the Zeeman shift for NV ensembles. As stated, for a single NV centre in the weak field regime, application of the external magnetic field causes separation of the $m_s = +1$ and $m_s = -1$ states proportional to the projection of the applied magnetic field onto the NV axis, as shown in Figure 12a.

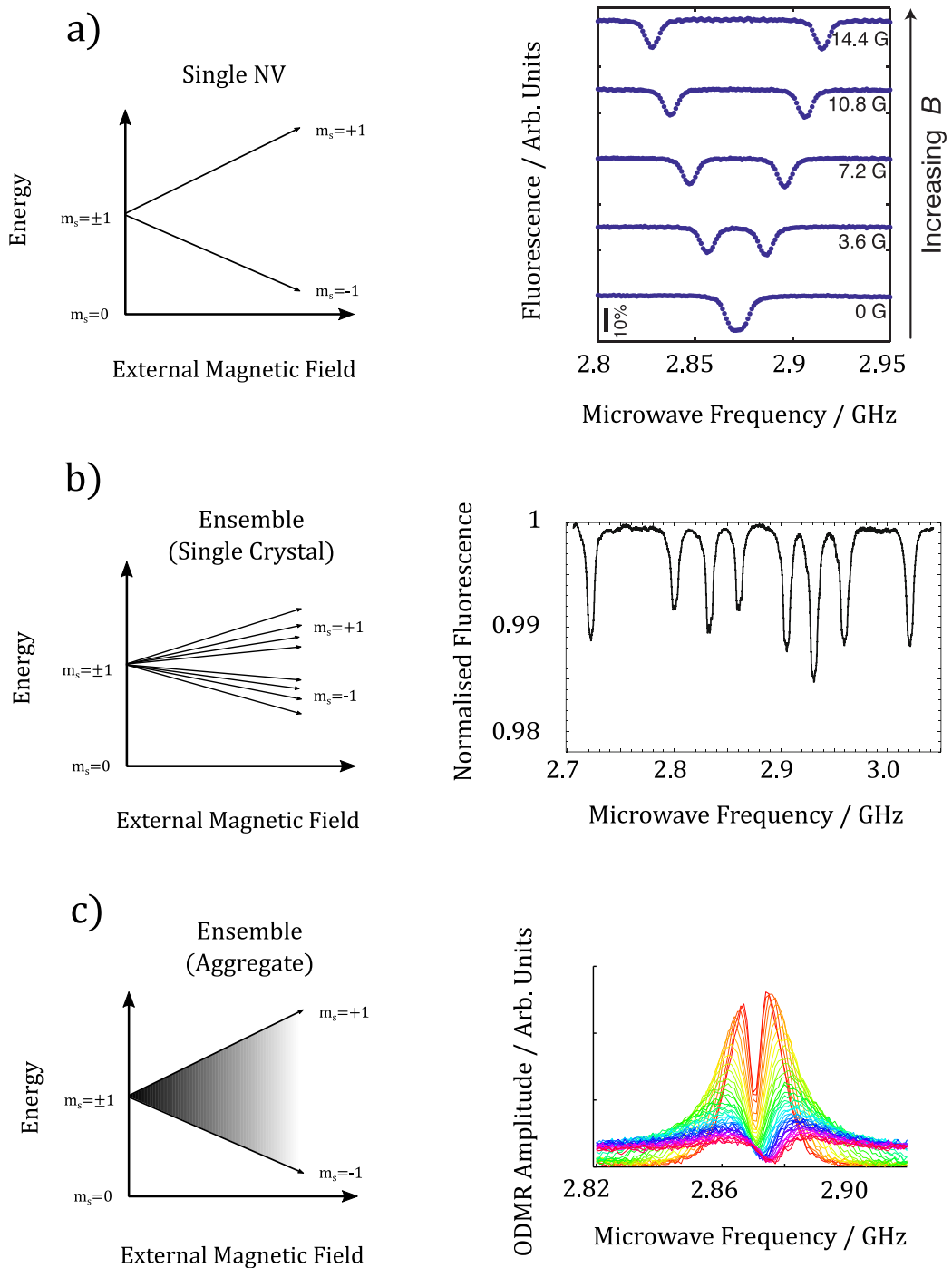


Figure 12 - Zeeman shifts for:

- a) a single NV centre - spectrum reproduced and adapted from [83],
- b) a single crystal ensemble - spectrum reproduced and adapted from [30], magnetic field applied in an arbitrary direction,
- c) an aggregate/powder - based on [84], spectra reproduced and adapted from [85] - spectra are from 0 to 40 Gauss.

In a single crystal ensemble, as there are NV centres aligned along four directions (Figure 6), the ensemble consists of four sub-ensembles, each measuring a different projection of the external magnetic field. This causes separation into four $m_s=+1$ resonances, and four $m_s=-1$ resonances upon application of a magnetic field [50], as shown in Figure 12b. Because off-resonant sub-ensembles do not contribute to the spin contrast but still fluoresce, spin contrast is reduced by a factor of four when addressing a single sub-ensemble compared to a single NV [50, 86]. This increases the relative background signal and therefore reduces the signal-to-noise ratio when performing magnetometry.

For an aggregate (or powder) of nanodiamonds, individual nanodiamonds within the aggregate can also have sub-ensembles but the individual crystals are randomly orientated [87]. This causes up to $4*n$ resonances per spin (m_s) transition, where n is the number of nanodiamonds being addressed. When an external magnetic field is applied and a large number of nanodiamonds are addressed, this produces a quasi-continuum of transitions between a minimum and maximum magnetic field projection due to the varied Zeeman shifts (65). This is shown in Figure 12c. This results in one broad resonance per spin (m_s) transition. As these have low ODMR contrast, the magnetometric sensitivity is severely degraded [61]. Therefore, it is necessary to make measurements using single crystals to achieve high-sensitivity magnetometry with ensembles.

2.2.6 - Optical Detection of Magnetic Resonance (ODMR)

The NV⁻ has attracted much attention in recent years as it can be optically polarised into the $m_s=0$ state by simply exciting the ${}^3A_2 \rightarrow {}^3E$ optical transition, even when at room temperature [50, 55, 79]. This optical transition generally obeys the selection rule $\Delta m_s=0$ and is therefore approximately spin conserving. However, the intersystem crossing (ISC) rates depend on the spin state [50]. In particular, the 3E $m_s=\pm 1$ states are more likely to transition to the singlet states than the 3E $m_s=0$ state. This is depicted in Figure 13.

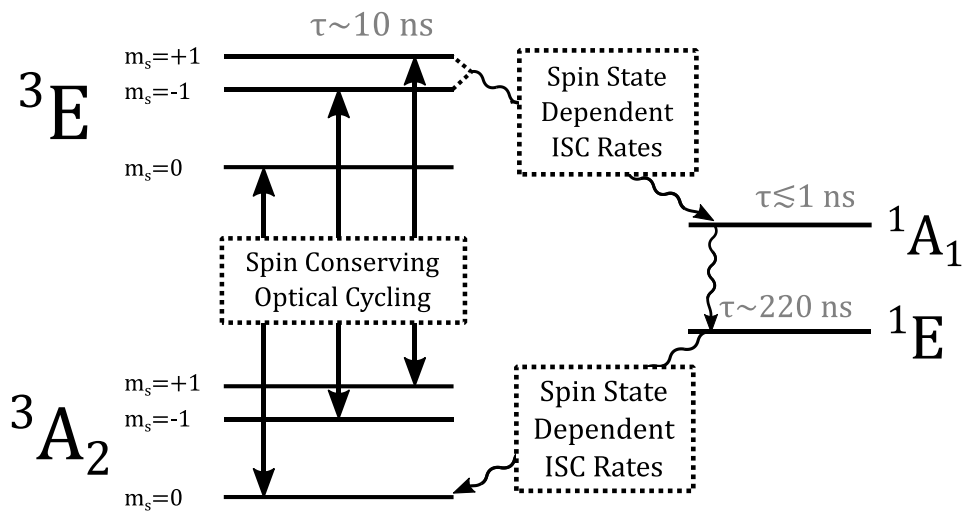


Figure 13 – Mechanism of spin contrast and optical spin polarisation. NV centres optically cycle on the ${}^3A_2 \leftrightarrow {}^3E$ transition. Spin state dependant ISC (intersystem crossing) rates cause spin polarisation into the $m_s=0$ state - based on [50].

When the NV⁻ is in the singlet state, it cannot undergo the ${}^3A_2 \leftrightarrow {}^3E$ transition.

Therefore, the $m_s=\pm 1$ states have a reduced probability of visible fluorescence

compared with the $m_s=0$ state. This creates distinguishability between the spin states via monitoring of the NV⁻ fluorescence rate.

Optical spin polarisation is further enhanced by spin state dependent ISC rates from the singlet states to the triplet states. The $^1E \rightarrow ^3A_2$ ISC transition is preferential to the 3A_2 $m_s=0$ state which, coupled with the $^3E \rightarrow ^1A_1$ preference, causes accumulation in the $m_s=0$ state of at least 80% of the NV⁻ population [50, 55]. Once polarised, NV-s are in their most fluorescent (brightest) state. If the $m_s=0 \rightarrow m_s=\pm 1$ transition occurs, a corresponding reduction in fluorescence is observed until spin re-polarisation into the $m_s=0$ state. This facilitates the optical detection of magnetic resonance which is the backbone of magnetometry with NV centres.

2.2.6.1 – Optical Magnetic Resonance Spectroscopy

When performing optical magnetic resonance spectroscopy, the NV⁻ fluorescence rate is monitored whilst the frequency of applied microwaves is swept across that of a magnetic resonance. Neglecting power broadening, a single hyperfine resonance has a Lorentzian line-shaped ODMR spectrum that can be described as a function of angular frequency (ω), as [16]:

$$F_{\text{single}}(\omega) = \text{Flu}_{\text{max}} \left(1 - C \frac{\left(\frac{\Gamma}{2}\right)^2}{\left(\frac{\Gamma}{2}\right)^2 + (\omega - \omega_0)^2} \right) \quad (10)$$

where Flu_{\max} is the maximum fluorescence intensity, C is the ODMR contrast and Γ is the full-width-half-maximum (FWHM) linewidth, as shown in Figure 14. The ODMR contrast is defined as [79]:

$$C = \frac{\text{Flu}_{\max} - \text{Flu}_{\min}}{\text{Flu}_{\max}} \quad (11)$$

where Flu_{\min} is the minimum fluorescence rate, as shown in Figure 14.

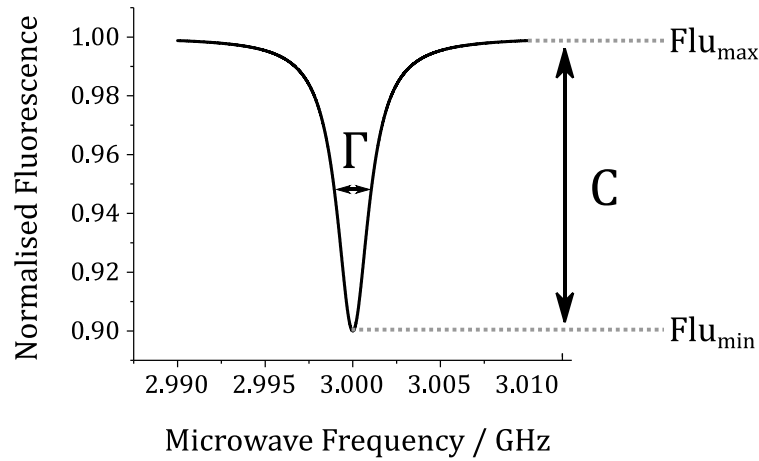


Figure 14 – Plot of single hyperfine ODMR feature centred at $\omega_0=2\pi*3$ GHz with $C = 0.1$, $\text{Flu}_{\max} = 1$ and $\Gamma = 2.2$ MHz.

2.2.6.2 – ODMR Linewidth

The minimum linewidth is the natural FWHM linewidth (Γ_{nat}). This can be determined using the natural dephasing time of the NV $^-$ electron spin (T_2) [79]:

$$\Gamma_{\text{nat}} = \frac{1}{\pi T_2} \quad (12)$$

However, the experimentally measured FWHM linewidth (Γ), in CW-ESR measurements, is set by the inhomogeneous dephasing time of the NV- electron spin (T_2^*):

$$\Gamma = \frac{1}{\pi T_2^*} \quad (13)$$

where $T_2^* \leq T_2$. T_2^* is reduced due to magnetic field noise in the environment [79], the readout method and the properties of the diamond.

With respect to the readout method, optical and microwave excitation can power broaden the ODMR resonance [88, 89]. However, if making a measurement of a magnetic field of known frequency and phase (AC magnetometry), coherent techniques can be used to improve sensitivity by a factor of $\sqrt{\frac{T_2^*}{T_2}}$, as described in a review by Rondin [79]. It should be noted that DC magnetometers measure fields within the bandwidth of the detector and, therefore, actually measure both AC and DC magnetic fields. For the intended application of magnetometric action potential detection, a DC magnetometry scheme is likely to be required as the action potentials occur with random phase.

As described in Section 2.1.1, the diamonds that exhibit NV centres with the best T_2^* are ultrapure and isotopically pure. T_2^* is increased by reducing the number of paramagnetic defects such as substitutional nitrogen and ^{13}C , thus minimising the randomly fluctuating spin bath internal to the diamond [88]. Of course, without any

substitutional nitrogen, you could not synthesise any NV centres, thus a balance must be struck in ensemble experiments. This also stresses the importance of developing techniques to improve substitutional nitrogen to NV centre conversion rates. Recent papers have demonstrated this to be around $\sim 10\%$ with current techniques [90, 91].

2.2.6.3 – Magnetometric Sensitivity Limits

The ODMR spectrum parameters limit the sensitivity of magnetometry with NV centres (η), defined as [50]:

$$\eta = \frac{B_{\text{measured}}\sqrt{\tau}}{\text{SNR}} \quad (14)$$

where B_{measured} is the measured magnetic field, τ is the measurement time and SNR is the signal-to-noise ratio of the measurement. Using the NV⁻ spin state for magnetometry has a spin-projection-noise-limited sensitivity given by [16]:

$$\eta_{\text{spin}} = \frac{\hbar}{g_s\mu_B} \frac{1}{\sqrt{NT_2^*}} \quad (15)$$

where N is the number of NV centres addressed.

By continually applying microwaves resonant with one of the $m_s=0 \rightarrow m_s=\pm 1$ transitions, the NV⁻ fluorescence maintains proportionality to the projection of the magnetic field applied to the measured axis. Magnetometry can, therefore, be performed by simply fixing the microwave frequency and detecting fluorescence changes due to Zeeman shifts of the ODMR resonance [79]. This technique is called

continuous-wave electron spin resonance (CW-ESR) and has a minimum detectable magnetometry sensitivity set by [88]:

$$\eta_{\text{CW-ESR}} = P_f \frac{\hbar}{g_s \mu_B} \frac{\Gamma}{C\sqrt{R}} \quad (16)$$

where R is the measured photon rate and P_f is a constant set by the ODMR lineshape. As \hbar , g_s and μ_B are fixed, the sensitivity is determined by the ODMR linewidth, contrast and measured photon rate.

The ODMR contrast is fundamentally limited by the intersystem crossing rates and the singlet and triplet state lifetimes [55]. Experimentally, it is proportional to the coupling strength of the microwaves to the NV centres. This depends on the applied microwave power [89, 92, 93] and the antenna alignment which should produce an oscillating B-field perpendicular to the measured NV axis [61].

The measured photon rate (R) depends on the experimental photon collection efficiency and the number of NV centres being measured. In ensemble measurements, R should scale linearly with the NV centre density, resulting in a shot-noise limited sensitivity decrease by a factor of $\frac{1}{\sqrt{N}}$ [79], where N is the number of NV centres measured. The photon collection efficiency depends on the particular technique used.

2.2.7 – ODMR Techniques

There have been several methods utilised to read out magnetic resonance from NV centres. Broadly, these can be split up into experiments that use single NV centres, and those that use ensembles.

Recent breakthroughs were in 2008 when both coherent control of a single NV centre in ultrapure bulk diamond [94], and nanoscale imaging with a single nanodiamond were demonstrated at room temperature [95].

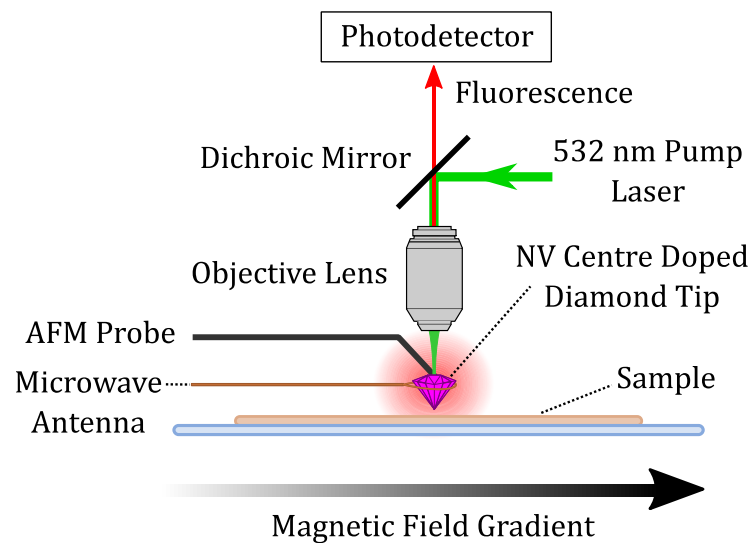


Figure 15 – Scanning magnetic imaging setup. NV centre is attached to an AFM (atomic force microscope) probe and read-out optically. By scanning the tip or sample, magnetic imaging can be achieved.

Although the setups vary, they generally involve attaching a single NV centre to a combined atomic force microscopy (AFM) / confocal fluorescence microscopy setup, as shown in Figure 15. Scanning can be performed by moving the sample under measurement [96] or AFM tip [97] and the NV centre can be contained in a nanodiamond [95] or in a bespoke bulk diamond AFM tip [98]. ODMR on a single NV is performed with a 532 nm excitation laser and optical filtering is achieved with a dichroic mirror. By performing spectroscopy in a known magnetic field gradient, the measured ODMR resonance becomes proportional to the NV position in the field and further spatial resolution improvements are possible [79]. By 2013, a single pixel DC sensitivity of $\sim 2 \mu\text{T}/\text{Hz}^{1/2}$ and AC sensitivity of $18 \text{ nT}/\text{Hz}^{1/2}$ had been achieved in a scanning setup [98]. Although nanoscale spatial resolution can be achieved, such measurements are extremely slow (42 min per point [98]).

In recent years, improvements in diamond sample quality have allowed AC sensitivities of $140 \text{ nT}/\text{Hz}^{1/2}$ [99] and $4 \text{ nT}/\text{Hz}^{1/2}$ [100] to be demonstrated with nanodiamond and bulk diamond respectively. However, these were in non-scanning setups. New techniques such as magnetic gradient sensing via coupling single NV centres to a mechanical resonator [101], coherent control of optically levitated nanodiamonds [102], relaxometry [103] and NV spin state to charge state conversion [104] may lead to improved single NV centre sensors in the near future.

Point magnetic field sensors using NV centre ensembles have also developed greatly in recent years. In 2015, $0.9 \text{ pT}/\text{Hz}^{1/2}$ was achieved with an AC magnetometry setup [105] and, in 2016, $15 \text{ pT}/\text{Hz}^{1/2}$ was achieved with a DC magnetometry setup with 3.6 kHz of bandwidth [16]. The DC magnetometer was used to measure the first action potential using NV centres [16].

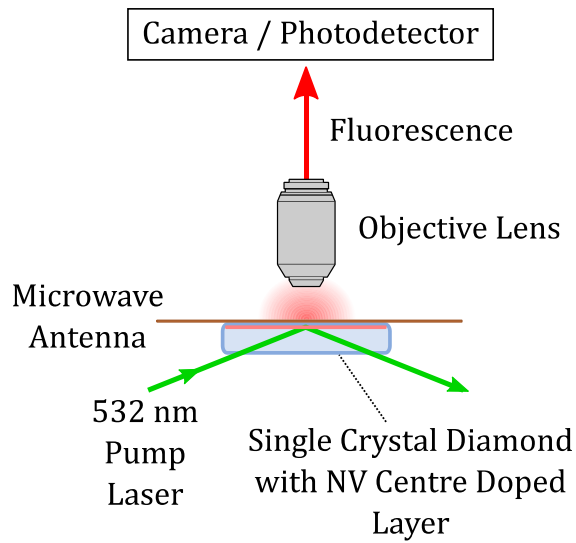


Figure 16 – Widefield fluorescence imaging / point-measurement ODMR setup. Pump laser is reflected off the diamond to minimise sample heating. Laser induced fluorescence is collected and either imaged with a camera or photodetector.

In this setup, the excitation beam was reflected off of the diamond to minimise heating of the sample, as shown in Figure 16. With this arrangement, fluorescence is collected with an objective lens and can be imaged onto a photodetector for point measurements or a camera to facilitate widefield magnetometry. Because this enables simultaneous measurement of the magnetic field over the entire microscopes field of view, this dramatically increases the bandwidth of widefield magnetic imaging compared with point scanning magnetometers. However, nanoscale resolution is lost as measurements are diffraction limited. Since 2010, this has led to several widefield experiments demonstrating both AC [106] and DC [107] magnetic imaging techniques. It should be noted that relatively long acquisition times are still currently required for high sensitivity measurements. For example, a DC sensitivity of 20 nT/Hz^{1/2} was achieved but with an imaging rate of only 10 frames per second [107] and in 2017, a sensitivity

of $\sim 1 \mu\text{T}/\text{Hz}^{1/2}$ was achieved whilst measuring at 60 frames per second [108]. As cameras with 10 kHz frame rates are available [108], widefield measurement of action potentials may be possible in future. The sensitivity limits using cameras are discussed in a recent paper by Wojciechowski [108].

Another advantage of using NV centre ensembles is the ability to perform magnetometry in multiple directions (vector magnetometry). This is achieved by measuring multiple NV axes and, since 2010 [107, 109], has been demonstrated in scanning imaging [109], widefield imaging [107] and point measurement systems [16]. The best sensitivity to date was with a non-scanning vector point measurement system, similar to that shown in Figure 16. A sensitivity of $50 \text{ pT}/\text{Hz}^{1/2}$ was simultaneously achieved along each Cartesian component [110].

Not all NV magnetometers rely on the detection of fluorescence to make measurements. Several other point measurement magnetometers have been developed that rely on absorption of a probe beam by the NV singlet states [111-114]. These typically use setups like that depicted in Figure 17, where a pump and probe beam are combined, passed through a diamond sample, then the probe isolated and measured.

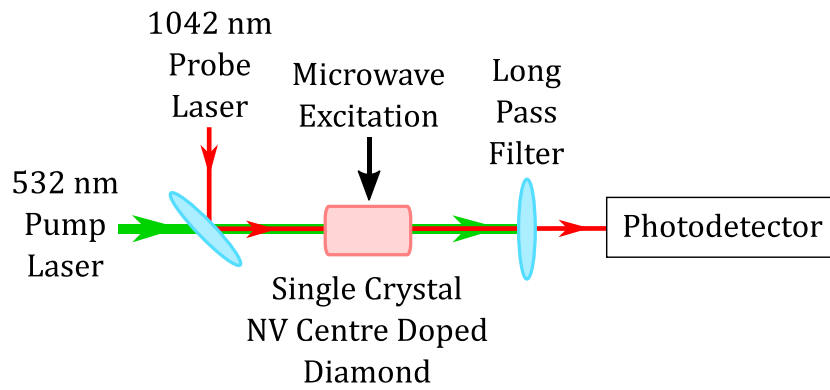


Figure 17 – Probe absorption ODMR setup. 1042 nm probe is overlapped with a 532 nm pump laser and passed through a diamond sample containing NV centres. The probe is subsequently filtered from the pump and measured with a photodetector.

Unlike fluorescence, which is emitted in all directions, the probe beam is collimated and allows for easy measurement. This was first demonstrated in 2010 at 75 K and achieved a sensitivity of $7 \text{ nT/Hz}^{1/2}$ [111]. Since then, in 2017, by placing the experiment in an optical cavity that was resonant with the singlet state transition, a sensitivity of $22 \text{ pT/Hz}^{1/2}$ was achieved at room temperature [114]. Recently, multiple magnetometry schemes have also been proposed that utilise stimulated emission from NV centres which could, theoretically, achieve record sensitivities of $\sim 1 \text{ fT/Hz}^{1/2}$ [23, 115]. These motivate the research into stimulated emission presented in Chapter 5.

Finally, detection of magnetic resonance from NV centres need not even be optical. Since 2016 [116], several experiments have demonstrated detection of magnetic resonance via monitoring currents generated by spin-state dependant photoionisation of NV centres [93, 116, 117]. A typical setup is depicted in Figure 18.

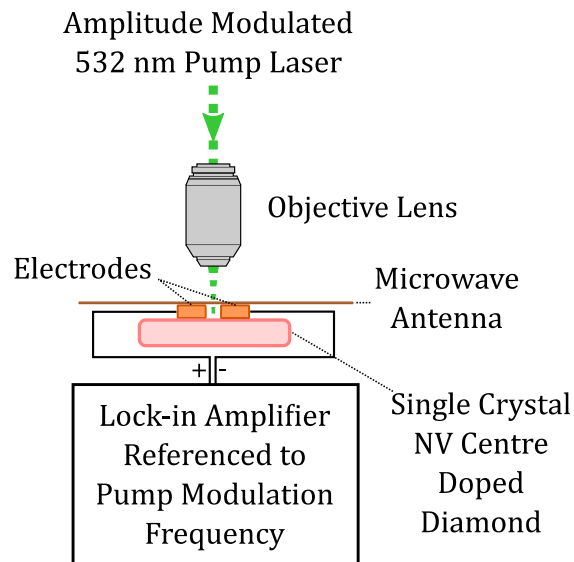


Figure 18 – Photoelectric detection of magnetic resonance setup. Magnetic resonance is measured using electrodes placed on the diamond. These measure photo-ionisation currents whilst microwaves and optical excitation are applied to the diamond.

In these experiments, the diamond is optically pumped, and electrodes are placed on the surface to readout the photoionisation currents. These are connected to a lock-in amplifier that is referenced to the modulation rate of the pump. This circumvents the problem of fluorescence collection efficiency and could, in future, lead to sensors that are faster and more sensitive than those that rely on optical detection [116].

2.2.8 - Charge State Conversion

Although NV centres do not permanently photobleach [11, 64-66], the photo-stability is a complicated matter. Charge state conversion has been experimentally demonstrated by both altering the local environment of the NV centre as well as through optical processes (photochromism). Charge state ratios have been demonstrated to be affected by irradiation with neutrons [118], doping with nitrogen [119] or phosphorus [120], applying electrochemical potentials [58, 121, 122] and using current injecting micro-electrodes [123]. Recently, it has been proposed that NV^- and NV^0 may form NV-NV molecules that share an electron through ground state tunnelling processes [124].

In work with HPHT nanodiamonds, variability in the charge state stability between individual NV centres under optical excitation was demonstrated [78]. Some NV centres remained in their charge state under relatively high excitation powers (10 mW), whereas others readily converted between charge states [78]. In earlier work with ultrapure bulk CVD, it was demonstrated that excitation with a wavelength that exclusively excited the negative charge state caused rapid photoionisation [125]. However, at commonly used excitation wavelengths such as 532 nm, both charge states are excited, and the NV centre does not photobleach. Evidence suggests this is achieved by dynamic photoionisation ($NV^- \rightarrow NV^0$) and recombination ($NV^0 \rightarrow NV^-$) processes [80]. Several NV centre photoionisation and recombination processes have been demonstrated and shown to be proportional to excitation power and wavelength [57, 80, 81, 126, 127]. These processes are summarised in Figure 19.

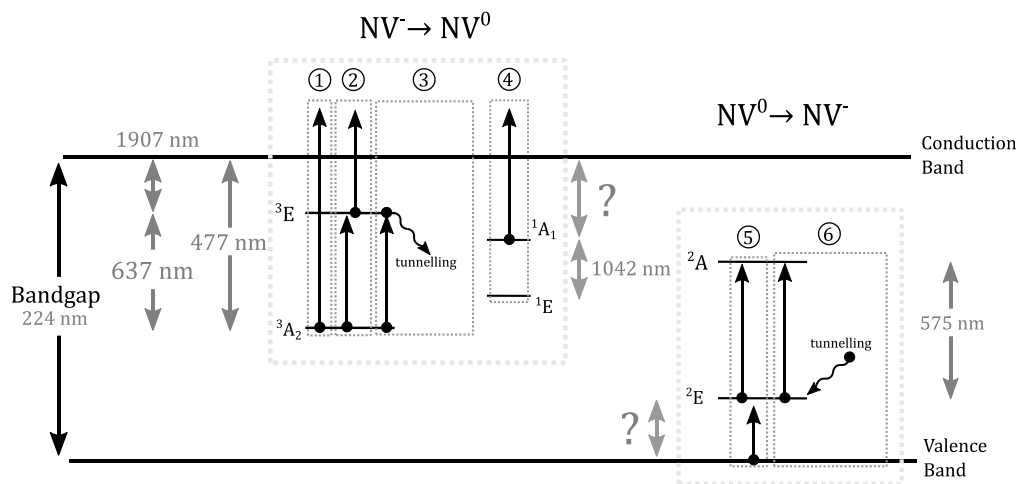


Figure 19 – Photoionisation and recombination processes of the NV centre:

1 – one-photon ionisation [57]

2 – two-photon ionisation via excited triplet state [55, 57]

3 – ionisation via excited state tunnelling [55, 81]

4 – ionisation via singlet state [127]

5 - two-photon recombination [55, 57]

6 – one-photon recombination via tunnelling [55]

Ground state tunnelling [124, 128] has been omitted for clarity.

The average contributions of the competing ionisation and recombination processes vary between diamond samples depending on factors such as electron donor/acceptor density [124, 128]. Although these processes are still not fully understood, they have already been utilised for multiple super-resolution and spin state readout techniques [104, 116, 117, 129-131].

Chapter 3

Optical Magnetometry under a Microscope using Nitrogen Vacancy Centre Ensembles

3.1 - Overview

In this chapter, the building of a fluorescence-based optical microscope system capable of magnetometry will be discussed. The system fundamentally uses the optical detection of magnetic resonance (ODMR) of nitrogen-vacancy centres in microdiamond to facilitate magnetometry. The system was designed to perform measurements of bio-magnetism with the goal of measuring action potentials of a dissected marine worm. The method of operation and performance in relation to this goal will be discussed.

3.2 - Introduction

The original aim of this research was to ascertain the sensitivity achievable using ensembles of fluorescent nanodiamonds to measure magnetic fields under a microscope. The intended long-term goal was to measure the action potentials of mammalian neurons as a tool for neural research. As discussed in Section 2.2.5.1, use of aggregates of nanodiamonds cannot be used to make highly sensitive magnetic field

measurements and single crystals must be used. 150 μm diameter HPHT diamonds containing nominally 2.5 ppm of NV⁻ were purchased from Adamas Nanotechnologies for use in these studies. Use of a larger microdiamond increased the fluorescence rate and signal-to-noise ratio compared with a single nanodiamond. Furthermore, it allowed different methods and detectors to be easily tested using the same sample. Use of a microdiamond is justified in that it is the same material as nanodiamonds before milling and should, therefore, have similar physical properties. Once the magnetometric sensitivity of the microdiamond is known, this can be considered an upper limit for the achievable sensitivity using a single nanodiamond of this type and with this method of magnetometry.

To test the instruments biocompatibility, the aim was to measure a marine worm action potential. In a recent measurement [16], a peak-to-peak magnetic field of ~ 1 nT was measured at ~ 1.2 mm from the axon centre. The DC equivalent / RMS value can be calculated from the following equation [132]:

$$V_{\text{RMS}} = \frac{V_{\text{pp}}}{2\sqrt{2}} \quad (17)$$

where V_{pp} is the peak-to-peak voltage. For V_{pp} of 1 nT, $V_{\text{RMS}} \sim 0.35$ nT.

As the diamond is in close proximity of the neuron, the action potential can be approximately modelled as a current in an infinite wire. The magnetic field (B) generated is then [133]:

$$B = \frac{\mu_0 I}{2\pi r} \quad (18)$$

Using Equation 18, a magnetic field of 0.35 nT at 1.2 mm would require a current of 2.1 μ A. Figure 32 shows the diamond is approximately in contact with the wire of nominal diameter 56 μ m. If the radial distance between the excitation focal point on the diamond and the wire centre is approximated at 50 μ m, the expected DC equivalent magnetic field is 8.4 nT. For an action potential duration of 2 ms [16] and $B = 8.4$ nT, a sensitivity of ~ 0.38 nT/Hz^{1/2} is, therefore, expected to allow measurement with a signal-to-noise ratio of 1, if averaged for 1 second [16].

Given that high optical excitation powers are likely to harm biological specimens, the excitation power was limited to 2 mW for the final results. This power was advised by colleagues in the Centre for Biophotonics (University of Strathclyde) who routinely image neuronal samples. Should this need to be adjusted in future, magnetometric sensitivity was measured as a function of optical power (Figure 41) for reference.

3.3 - Experimental Method

3.3.1 - Experimental Overview

Magnetometry was performed using the optical detection of magnetic resonance (ODMR) of a nitrogen-vacancy centre ensemble contained within a single microdiamond. By continually applying modulated microwaves resonant with one of the $m_s=0 \rightarrow m_s=\pm 1$ transitions, the NV⁻ fluorescence maintained proportionality to the projection of the magnetic field applied to the measured sub-ensemble NV axis (CW-

ESR). All three microwave hyperfine transitions were excited simultaneously. A simplified experimental setup is shown in Figure 20.

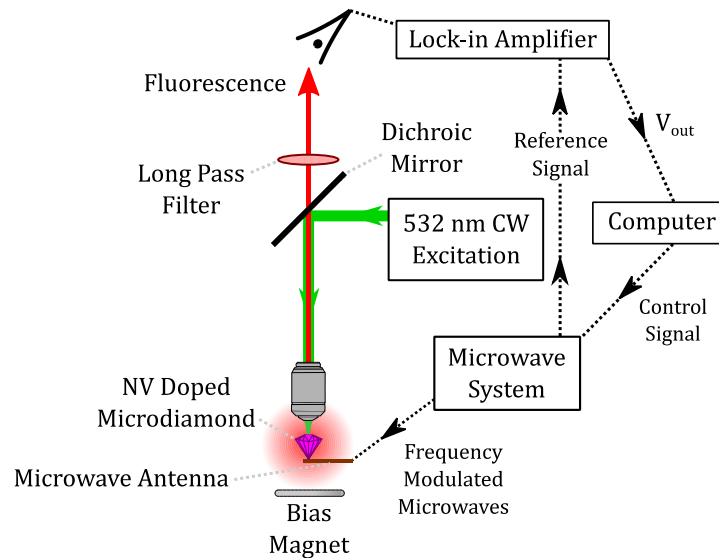


Figure 20 – Simplified experimental setup for magnetometry. Microwaves are applied, and fluorescence is excited with a 532 nm laser and collected with an objective lens. A lock-in amplifier is used to convert the measured fluorescence signal into a magnetometry signal.

3.3.2 - Theory of Operation

Optical excitation was achieved using a 532 nm continuous wave (CW) laser which provided simultaneous optical spin polarisation and read-out. By using an epifluorescence microscope setup, excitation and fluorescence collection was possible via a single objective lens and optical filtering was achieved with a dichroic mirror and long-pass filter. Fluorescence was measured with a photodetector and the signal sent to a lock-in amplifier referenced to the frequency modulation rate of the microwaves

(f_{FM}). Microwaves were square-wave modulated at $f_{FM} \sim 20$ kHz around a centre frequency ω_c , with a deviation of $\omega_{Dev} \sim 3.4$ MHz as such:

$$\omega_1 = \omega_c + \omega_{Dev} \text{square}(2\pi f_{FM} t) \quad (19)$$

As with previous experiments, modulation at higher frequencies (f_{FM}) was found to decrease ODMR amplitudes and resulted in a reduced signal-to-noise ratio for magnetometry [16, 134]. This limitation has previously been attributed to the time taken for optical spin re-polarisation [134]. Microwaves were applied with a microstrip antenna on which the microdiamond was placed. The output of the lock-in amplifier (V_{out}) was the magnetometry signal.

3.3.3 - Lock-in Amplifier Output

As described in Section 2.2.6.1, a single hyperfine resonance has a Lorentzian line-shaped ODMR spectrum. However, after frequency modulation and demodulation, the output of the lock-in amplifier (V_{out}) is a dispersion-like signal, shown in Figure 21b, described by [16]:

$$V_{out}(\omega_c) = \left(\frac{V_0 C}{2} \left(-\frac{\left(\frac{\Gamma}{2}\right)^2}{\left(\frac{\Gamma}{2}\right)^2 + (\omega_c - \omega_{Dev}) - \omega_0)^2} + \frac{\left(\frac{\Gamma}{2}\right)^2}{\left(\frac{\Gamma}{2}\right)^2 + (\omega_c + \omega_{Dev}) - \omega_0)^2} \right) \right) \quad (20)$$

where V_0 is a constant set by the signal amplitude and lock-in amplifier settings. HPHT diamond with a similar NV \cdot concentration to that used in the following

experiments (~ 2.5 ppm) has previously been measured to have a T_2^* of ~ 145 ns [61]. This corresponds to a $\Delta\nu_{\min}$ of ~ 2.2 MHz. For a Lorentzian lineshape ODMR feature, the slope of the zero-field splitting is maximised for $\omega_{\text{Dev}} = \frac{\Gamma}{2\sqrt{3}}$ [16].

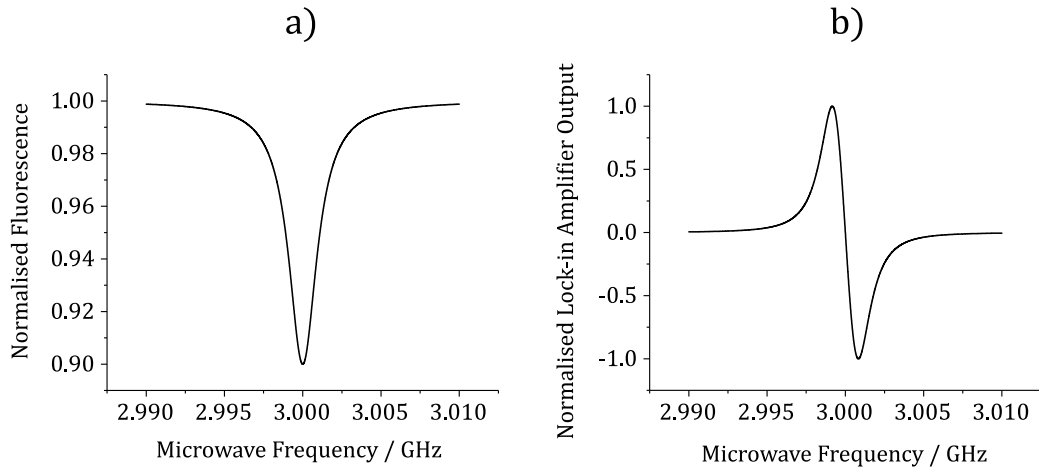


Figure 21 - a) Plot of single hyperfine ODMR feature with $\omega_0 = 2\pi \cdot 3$ GHz, $C = 0.1$, $F_0 = 1$ and $\Gamma = 2.2$ MHz and b) corresponding lock-in amplifier output with $\omega_{\text{Dev}} = \frac{\Gamma}{2\sqrt{3}}$ based on [16].

As discussed in Section 2.2.5, due to the ^{14}N hyperfine coupling, there are three microwave hyperfine resonances centred around ω_0 , as shown in Figure 22a, and contrast can be increased by addressing all three simultaneously [16]. This is achieved by mixing ω_1 with a sine wave of $\omega_{\text{HF}} = A_{\parallel}$ (the hyperfine separation). When applying the multi-frequency microwaves, the ODMR spectrum shows five peaks, as shown in Figure 22b. The outer peaks correspond to a single hyperfine resonance being addressed, the second and fourth correspond to two and the centre resonance corresponds to when all three hyperfine resonances are excited simultaneously [16].

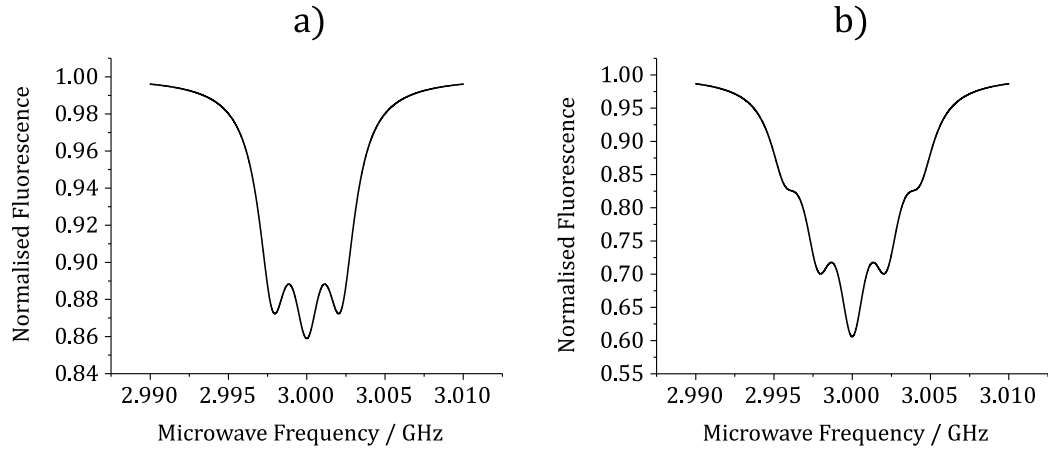


Figure 22 – a) Plot of three hyperfine transition ODMR feature with $\omega_0 = 2\pi \cdot 3$ GHz, $C = 0.1$, $F_0 = 1$ and $\Gamma = 2.2$ MHz and b) same resonance measured with multi-frequency excitation with $\omega_{\text{Dev}} = \frac{\Gamma}{2\sqrt{3}}$ – based on [16].

This results in a corresponding lock-in amplifier output described by [16]:

$$V_{\text{out}}(\omega_c) = V_0 \left(\sum_{p=-1}^1 \sum_{q=-1}^1 -C \frac{\left(\frac{\Gamma}{2}\right)^2}{\left(\frac{\Gamma}{2}\right)^2 + ((\omega_c + p\omega_{\text{HF}} - \omega_{\text{Dev}}) - (\omega_0 + q\omega_{\text{HF}}))^2} + C \frac{\left(\frac{\Gamma}{2}\right)^2}{\left(\frac{\Gamma}{2}\right)^2 + ((\omega_c + p\omega_{\text{HF}} + \omega_{\text{Dev}}) - (\omega_0 + q\omega_{\text{HF}}))^2} \right) \quad (21)$$

as shown in Figure 23.

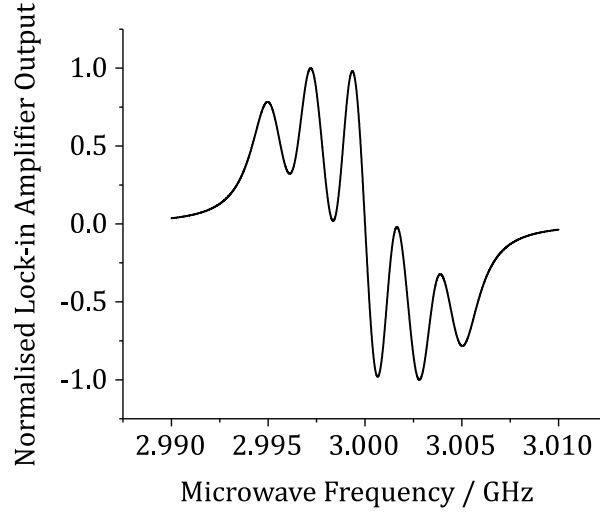


Figure 23 – Plot of lock-in amplifier output with three hyperfine resonances and multi-frequency excitation with $\omega_0 = 2\pi \cdot 3$ GHz, $C = 0.1$, $F_0 = 1$ and $\Gamma = 2.2$ MHz and $\omega_{\text{Dev}} = \frac{\Gamma}{2\sqrt{3}}$ – based on [16].

By setting ω_c to ω_0 , the output of the lock-in amplifier is proportional to Zeeman shifts of the ODMR resonances [16]:

$$V_{\text{out}} \propto \frac{V_0 C}{\Gamma} \frac{g_s \mu_B}{\hbar} B_z(t) \quad (22)$$

where $B_z(t)$ is the magnetic field projection onto the measured NV axis as a function of time, \hbar is the reduced Planck's constant, μ_B is the Bohr magneton and g_s is the electron-spin g-factor.

3.3.4 - Sensitivity Limits

The microdiamond used in this experiment had a nominal NV⁻ concentration of 2.5 ppm. HPHT diamond with ~2.5 ppm NV⁻ concentration has previously been measured to have a $T_2^* \sim 145$ ns [61]. If a 1 micron diameter beam addresses a volume roughly approximated by a sphere of 1 micron diameter, a volume of 5.236×10^{-19} m³ or 5.236×10^{-13} cm³ is addressed. As a NV⁻ concentration of 1 ppm = 1.76×10^{17} cm⁻³ [61], this corresponds to 230×10^3 NV⁻. Assuming $\frac{1}{4}$ of the NV centre ensemble contribute to the signal, from Equation 15, this gives $\eta_{\text{spin}} \sim 62$ pT/Hz^{1/2}.

For CW-ESR magnetometry with a Lorentzian lineshape, the photon-shot-noise limited sensitivity is [16, 88]:

$$\eta_{\text{CW ESR}} = \frac{4}{3\sqrt{3}} \frac{h}{g_e \mu_B} \frac{\Gamma_{\text{PB}}}{C\sqrt{R}} \quad (23)$$

where h is Planck's constant, Γ_{PB} is the power broadened full-width-half-maximum resonance linewidth and R is the detected photon rate defined as [16]:

$$R = \frac{V_{\text{PD}}}{R_L q} \quad (24)$$

where q is the elementary charge and V_{PD} is the voltage measured across a $R_L \Omega$ load due to the signal photocurrent generated by the measured fluorescence.

Experimentally, the sensitivity was quantified by measuring a sinusoidal magnetic field oscillation of known amplitude (B_{measured}). The signal-to-noise ratio (SNR) is defined as:

$$\text{SNR} = \frac{V_{\text{signal}}}{V_{\text{noise}}} \quad (25)$$

where V_{signal} and V_{noise} are the respective RMS (root mean square) voltages. V_{signal} was obtained by fitting sinewaves to averaged measurements in MATLAB and calculating the RMS value from the amplitude. V_{noise} was obtained by taking the RMS of the residuals of the fit. This allowed the sensitivity to be calculated using Equation 14.

3.4 - Experimental Set-up

A detailed experimental set-up is shown in Figure 24:

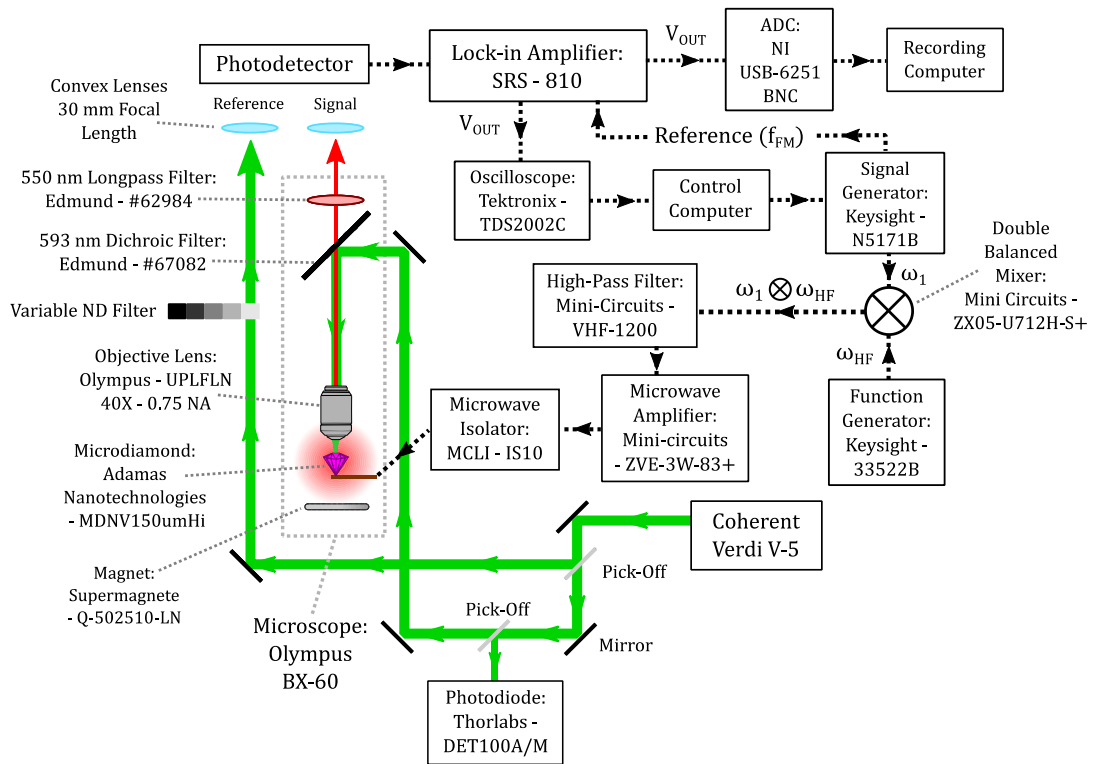


Figure 24 – Magnetometry experimental setup. Microwave signal components are generated with signal generators, mixed, filtered and applied to an NV centre doped diamond. Fluorescence is excited with a 532 nm laser, collected with an objective lens and measured with a photodiode. The fluorescence signal is processed by a lock-in amplifier to produce the magnetometry signal.

3.4.1 - Optics

The excitation laser was coupled into the microscope with a series of mirrors and a periscope. It was subsequently focused into the microdiamond and the fluorescence collected with a single objective lens. Optical powers were measured at the sample using a calibrated optical power meter (Thorlabs - PM100D, S130C) and used to calibrate a beam pick-off measured with a photodiode. This was used to monitor the

excitation powers during experimentation. Fluorescence passed through the dichroic mirror and long-pass filter and was focused onto the photodetector. This was connected to a lock-in amplifier to reduce the noise contributed to the magnetometry signal from the photodetection, microwave and laser systems. However, this is incapable of reducing any noise at the lock-in modulation frequency.

Several photo-detectors were also tested that aimed to reduce laser amplitude noise from the signal entering the lock-in amplifier. These subtracted or divided a reference laser signal from the fluorescence signal. This required a pick off from the excitation beam to be separately coupled via mirrors and a periscope adjacent to the microscope, as shown in Figure 25. Intensity control was achieved using the lasers control box, stacked neutral density filters and a variable neutral density filter on the reference beam path. A commercial auto-balanced subtraction detector (Newport - Nirvana 2007) and a homebuilt divider circuit were tested.



Figure 25 – Photograph of magnetometer.

3.4.2 - Microwave Generation

The ω_1 signal was generated by a Keysight N5171B signal generator using the inbuilt frequency modulation (FM) function. The FM modulation rate was sent from the 'LF OUT' port as a TTL (transistor-transistor logic) signal and connected to the 'REF IN' of the lock-in amplifier to be used as the demodulation reference. The ω_1 signal was sent from the 'RF Output' port and connected to a double-balanced mixer. The ω_{HF} signal was generated with a Keysight 33522B function generator and connected to the double-balanced mixer via a BNC cable. The mixed signal was passed through a high pass filter, was amplified and then sent to a microstrip antenna after passing through a microwave isolator to prevent microwave power being sent back to the amplifier. All connections, except where specified, were with SMA cables and components were nominally at 50 Ω impedance. The N5171B was connected to a computer via USB to allow automated control via scripts written in MATLAB.

3.4.3 - Microwave Negative Feedback System

When measuring a repeatable magnetic field fluctuation, such as that generated by a current pulse, averaging measurements can significantly increase the SNR (signal-to-noise ratio) at the expense of measurement bandwidth. Assuming noise sources are random or chaotic, they tend to zero upon averaging and an improvement in SNR scales as $\frac{1}{\sqrt{N}}$ [135], where N is the number of measurements averaged. As [50]:

$$B_{\min} = \frac{B_{\text{measured}}}{\text{SNR}} \quad (26)$$

increasing the SNR can significantly decrease the smallest detectable magnetic field (B_{\min}).

$\frac{dB}{dV_{out}}$ is the rate of change of output voltage with respect to the change in magnetic field and is set by the physical properties of the NV centres, the angle between the magnetic field vector and NV axis, the fluorescence collection efficiency and the gain of the photodetector and lock-in amplifier. To maximise $\frac{dB}{dV_{out}}$ for a given photodetector voltage (V_{PD}), the lock-in amplifier sensitivity setting should be minimised (i.e. highest gain). When the input voltage exceeds the lock-in amplifier's output range, it is said to overload. By using a negative feedback system, the sensitivity can be kept at a low setting, and measurements can be performed for extended periods of time without low frequency drift causing the lock-in amplifier to overload. As the zero-field splitting d is sensitive to temperature variations ($\frac{dD}{dT} = -74.2(7)$ kHz/K [136]), significant sources of drift include laboratory temperature or laser intensity fluctuations [16].

The feedback system consisted of a control computer which was connected via USB to both an oscilloscope displaying the output of the lock-in amplifier as well as the Keysight N5171B which generated the microwave signal (ω_1). A MATLAB script (Appendix 2) read the waveform displayed on the oscilloscope and calculated the mean. The script then adjusted ω_1 proportionally to the calculated mean, thereby driving the lock-in amplifier output towards zero. The microwave frequency was adjusted at a rate of ~ 0.6 Hz.

3.4.4 - Microwave Antennae

Several microwave antenna designs were tested. Initial tests were with straight wires and loops soldered to SMA connectors but optimising their position was found to be difficult. To overcome this, antennae were fabricated using printed circuit board (PCB) fabrication facilities. The process involved creating antennae designs with PCB design software (Autodesk – Eagle) and laser printing the design onto a transparent acetate sheet. This was placed onto a double-sided photoresist-coated PCB copper laminate and exposed to ultra-violet (UV) light. The acetate was removed and then the laminate placed in a developing solution and subsequently placed in an etchant solution. This process removed the photoresist and copper from the laminate where the UV light was exposed, thus leaving only the antennae design. The resolution was technically limited by the printer at 600 dots per inch or ~ 1 dot per 42 microns. However, due to imperfections in the exposing, developing and etching, the thinnest track/gap was limited to about 0.5 mm with the in-house facilities.

There are several antennae designs optimised for NV centre coupling discussed in the literature. Unfortunately, many have dimensions beyond the discussed fabrication resolution limits [92, 137] or required expensive components such as microwave phase shifters [138, 139]. Furthermore, microwave design software, which has been used by several groups to optimise antennae design [92, 137, 138], was prohibitively expensive in both time and money.

A microstrip transmission line was fabricated and glued on top of a microscope slide as shown in Figure 26. This allowed the antenna to be positioned using the microscopes mechanical stage.

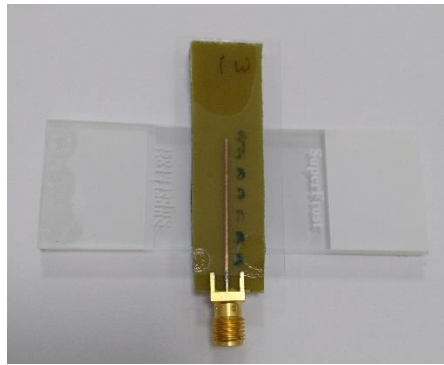


Figure 26 - Microstrip microwave antenna.

The transmission line is similar to a straight wire antenna described by Yang *et al* [140] but allowed a sample to sit on top of the microstrip at the most resonant position. The following calculations are for the antenna alone due to the difficulty of calculating the effect of the sample on the antenna without the aid of software.

The microstrip transmission line is characterised by the substrate thickness (h), the dielectric constant ϵ_R of the substrate and the width (W) of the copper track, as shown in Figure 27.

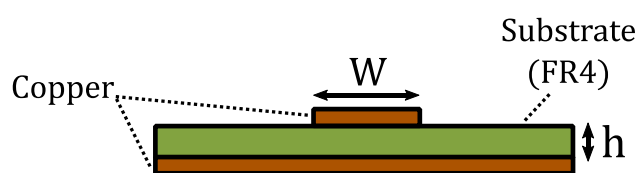


Figure 27 – Microstrip transmission line. Front facing view.

The impedance of a microstrip transmission line (Z) with $W > h$ can be calculated by the following equation [141]:

$$Z = \frac{120\pi}{\sqrt{\epsilon_{\text{eff}} \left(\frac{W}{h} + 1.393 + 0.667 \ln \left(\frac{W}{h} + 1.444 \right) \right)}} \quad (27)$$

where [141]:

$$\epsilon_{\text{eff}} = \frac{\epsilon_R + 1}{2} + \frac{\epsilon_R - 1}{2} \frac{1}{\sqrt{1 + 12 \frac{h}{W}}} \quad (28)$$

The photoresist board used (CIF – ABB16) had a nominal ϵ_R of 4.7 and $h = 0.8$ mm. For a 50Ω impedance, a W of ~ 1.47 mm is required according to Equations 27 and 28. A range of antennae with widths ranging from 0.5 to 3 mm were fabricated to test the validity of these models and to find the optimum dimensions to enable coupling of the microwaves to the NV centres.

3.4.5 - Photodetector

To mitigate laser noise entering the lock-in amplifier, a detector was designed and fabricated to divide the experimental fluorescence signal from a reference signal derived from an excitation laser pick-off. The division detector consisted of two reverse biased transimpedance amplified photodiodes using Hamamatsu – S1223-01 photodiodes and an Analog Devices - AD822N dual op-amp. This was connected to an analog computation unit (Analog Devices – AD538) to perform the division. The circuit diagram is shown in Figure 28. The detector was powered by four lithium 9V batteries regulated to 12 V to minimise power supply noise.

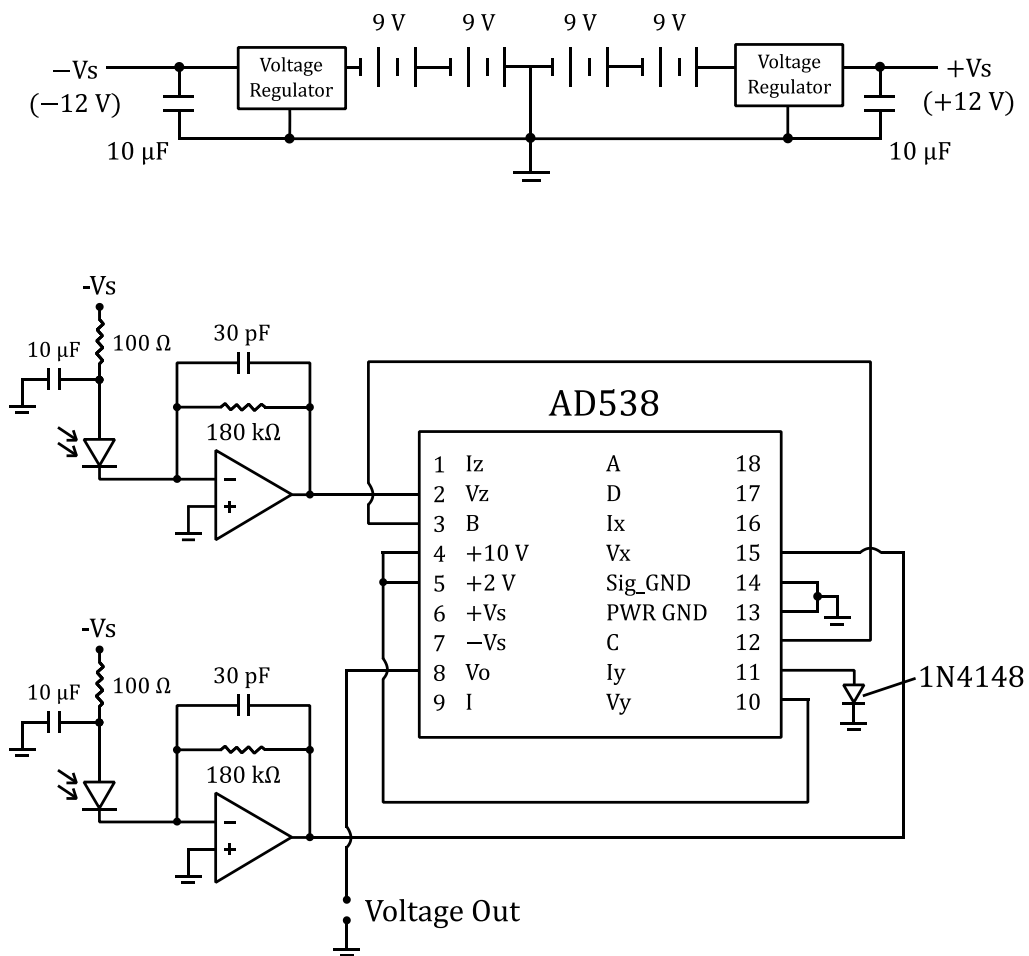


Figure 28 – Circuit diagram for division detector, 100nF capacitors on all power rails have been omitted for clarity. Circuit consists of two transimpedance amplified photodiodes connected to an analog division integrated circuit. The entire circuit is powered by four 9 V batteries.

The circuit was fabricated onto printed circuit board (PCB) (layout and fabrication by Ged Drinkwater, Department of Physics, University of Strathclyde), populated with components and placed into a metal box, as shown in Figures 29 and 30.

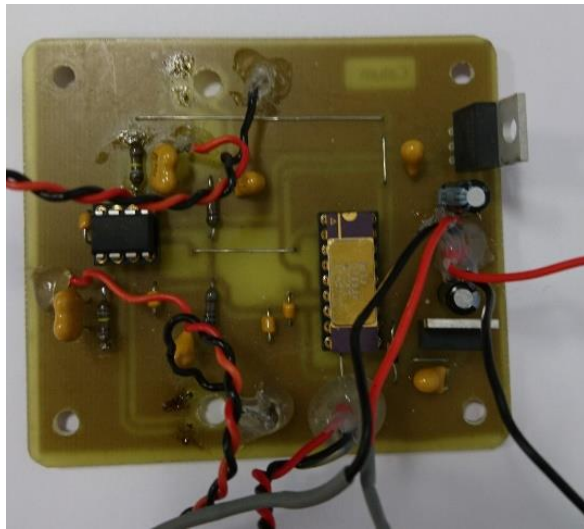


Figure 29 - PCB of division detector with all components except the photodiodes.



Figure 30 - Division detector box.

BNC connectors were utilised to allow the output from each transimpedance amplifier to be monitored as well as the output of the AD538. This allowed a single TIA photodiode to be tested as well as the subtraction of the generated signal and reference voltages via the 'A-B' input of the lock-in amplifier. The detector was compared with a commercially available auto-balanced subtraction detector (Newport – Nirvana 2007).

3.4.6 - B-Field Generation

To mimic the measurement of a neuron, magnetic fields were generated using a current through a wire. The wire had a nominal diameter of 56 μm and was placed on the microwave antenna in contact with the diamond, as shown in Figures 31 and 32. 500 Hz to 1 kHz square and sinusoidal currents from 1 μA to 1 mA were generated using a Keysight B2902A which is capable of directly generating modulated currents and current pulses with sub nA resolution. The current supply also outputted a TTL trigger signal for synchronisation of repeated measurements.

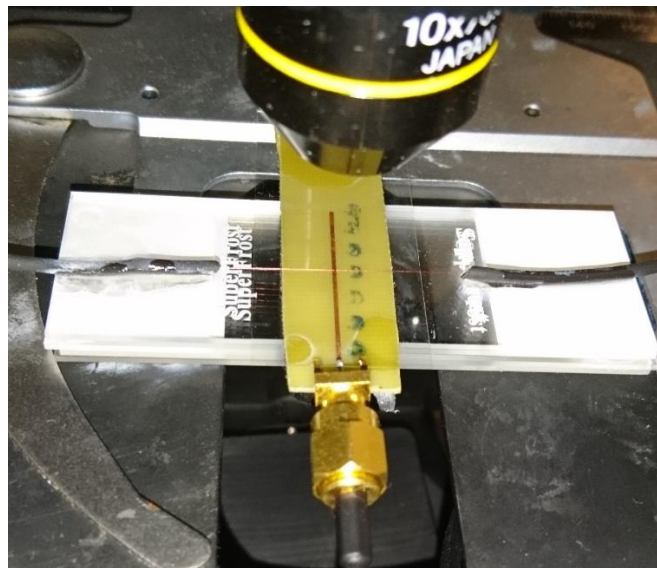


Figure 31 – Arrangement showing wire used to generate magnetic fields sitting on the antenna, in contact with the microdiamond.

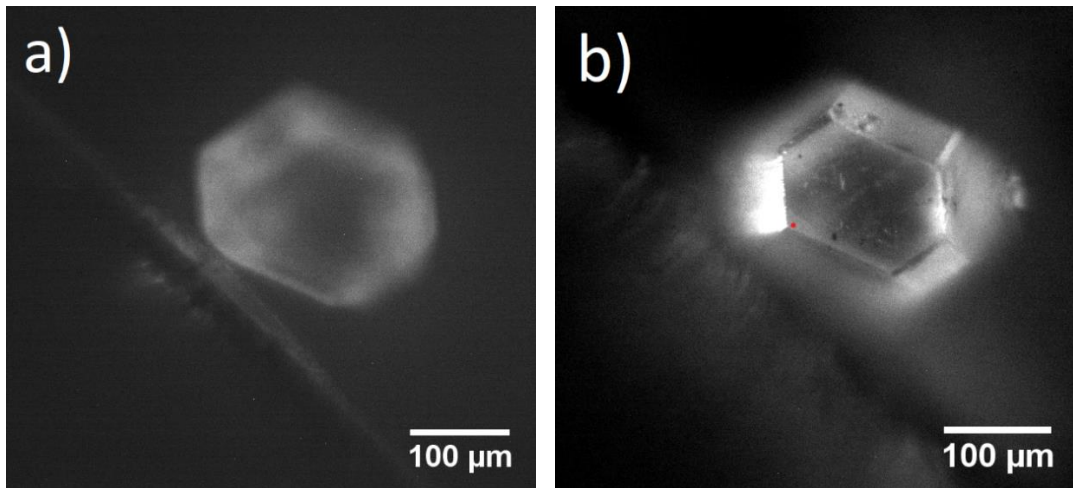


Figure 32 – Micrographs showing the microdiamond in contact with the wire at different focal planes, approximate beam placement and size shown by red spot in b).

A bias magnetic field up to ~ 20 Gauss was generated with permanent ferrite magnets (Supermagnete – FE-Q-50-50-05) placed below the antenna on the microscopes condenser lens holder. As the microwave antenna blocked microscope transmission light in the setup, placement here did not limit the microscope use any further. This also allowed convenient tuning of the magnetic field bias by varying the distance between the magnets and the sample using the condenser lens adjustment.

3.4.7 - Data Acquisition

Data was acquired using a National Instruments - USB-6251-BNC analog to digital converter (ADC) controlled by a computer running MATLAB (Appendix 1). The ADC has a 16-bit resolution and a total sample rate of 250 kHz to be equally shared across the channels. Two channels were recorded with a sample rate of 125 kHz; the output of the lock-in amplifier and a trigger TTL signal from the current supply generating the repeated magnetic field. This allowed averaging and analysis to be performed after

recording the raw data. As the measurement sample rate was over 40 times the magnetometer bandwidth of 3.1 kHz, aliasing is avoided. It was found that the ADC exhibited crosstalk between the channels. This was minimised by using physically separated channels (0 and 7) but was dealt with by discarding the first 0.5 ms of sampled magnetometry data corresponding to when the trigger was high. Finally, the output of the lock-in amplifier exceeded the input voltage rails by approximately 1 Volt, therefore a simple voltage divider circuit was added to the channel input.

3.5 - Results

3.5.1 - Antennae

To characterise the antennae, the ODMR contrast was measured as a function of position lengthwise on each antenna. The same microdiamond was used throughout these measurements and was sandwiched between two glass coverslips, adhered with nail varnish, to allow easy handling. The ODMR contrast was determined by measuring the fluorescence rate (V_{PD}) with and without microwaves applied. A typical antenna response, as a function of position, is shown in Figure 33. Error bars correspond to the oscilloscope resolution and DC accuracy uncertainty for the ODMR contrast and estimated at ± 1 mm for position on the antenna.

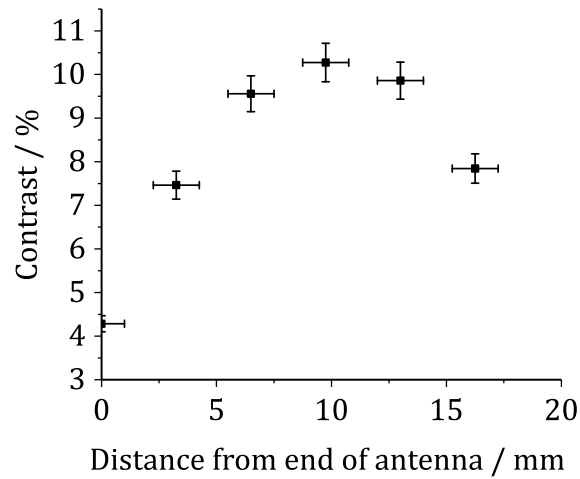


Figure 33 – ODMR contrast as a function of sample position on antenna. 2 mW of optical excitation and full microwave power was used in these measurements.

Figure 33 shows there was a clear peak in antenna performance ~ 9 mm from the tip of the antenna. This gives a convenient position to place samples and based on previous research [140], it is assumed to be due to the formation of a standing wave.

The maximum ODMR contrast that could be achieved for each antenna was measured as a function of microstrip width, as shown in Figure 34. Error in antenna width corresponds to an estimated fabrication tolerance of ± 0.25 mm and the oscilloscope resolution and DC accuracy uncertainty for ODMR contrast.

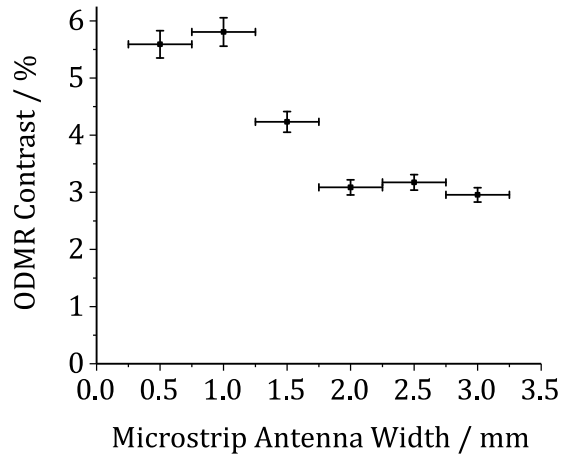


Figure 34 - ODMR contrast as a function of microstrip width. 2 mW of optical excitation and full microwave power was used in these measurements.

Individual maxima were determined by measuring the ODMR contrast for each antenna as a function of sample position. Figure 34 shows two antennae clearly out-performed the others, both of which were suitable for use in the magnetometry experiments.

Overall contrast was lower than in Figure 33 as this data was taken before the microwave amplifier was upgraded from a 1-Watt model (ZVE-8G+) to the 3-Watt model (ZVE-3W-83+) used in the magnetometry experiments.

Figure 35 shows the ODMR contrast as a function of microwave power for a single sub-ensemble at a constant 2 mW optical excitation power. Error bars correspond to the standard deviation of the measurements.

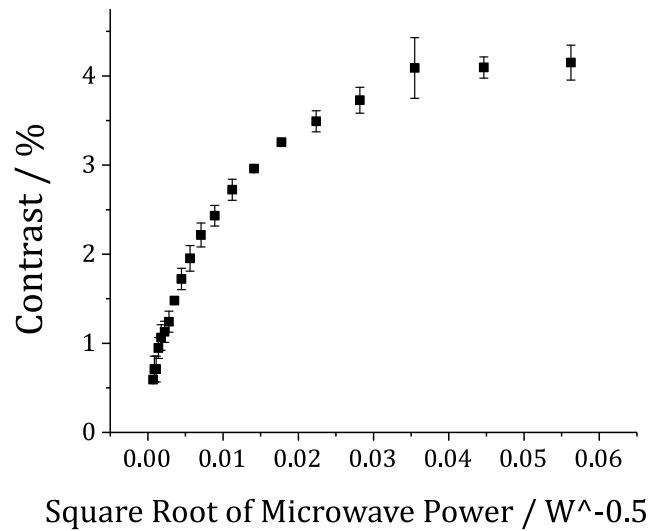


Figure 35 - ODMR contrast as a function of microwave power out of signal generator. 2 mW of optical excitation was used in these measurements.

Figure 35 shows the ODMR contrast saturates at approximately 4 %.

3.5.2 - Resonance Features

ODMR spectra were obtained to qualitatively compare the lineshapes with the expected spectra shown in Section 3.3.3. Spectra are shown at low and high microwave power to demonstrate the loss of resolution at high power due to power broadening. Because magnetometric sensitivity is proportional to linewidth (Equation 23), power broadening would be expected to decrease the magnetometric sensitivity. However, as shown in Figure 35, the ODMR contrast increased with microwave power and therefore there is a trade-off between the resonance linewidth and ODMR contrast. In Section 3.5.4, the overall magnetometric sensitivity as a function of microwave power is measured.

To obtain the spectra shown in Figures 36-39, the microwave frequency was swept, and the output of the lock-in amplifier was recorded using an oscilloscope. Figure 36 shows ODMR spectra at low and high microwave power using a single microwave frequency and using amplitude modulation. Single frequency measurements were made by plugging ω_1 directly into the high pass filter, thereby bypassing the double-balanced mixer. Microwave powers are those set by the signal generator. The multi-frequency microwave powers used are higher than the single frequency powers due to the additional attenuation by the double balanced mixer.

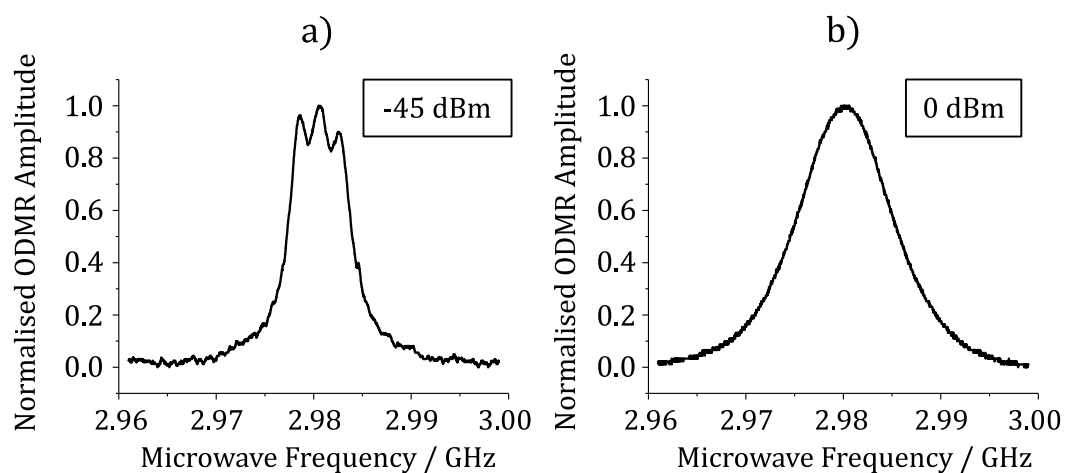


Figure 36 – ODMR spectra using amplitude modulation of the microwaves and a single microwave frequency. 2 mW of optical excitation was used in these measurements.

Figure 36a shows the expected hyperfine coupling shown in Figure 22a was observed, confirming that the sample contains mainly ^{14}N . Figure 36b shows that at high microwave power, there is sufficient power broadening to obscure the hyperfine structure

Figure 37 shows ODMR spectra taken using frequency modulation and a single microwave frequency.

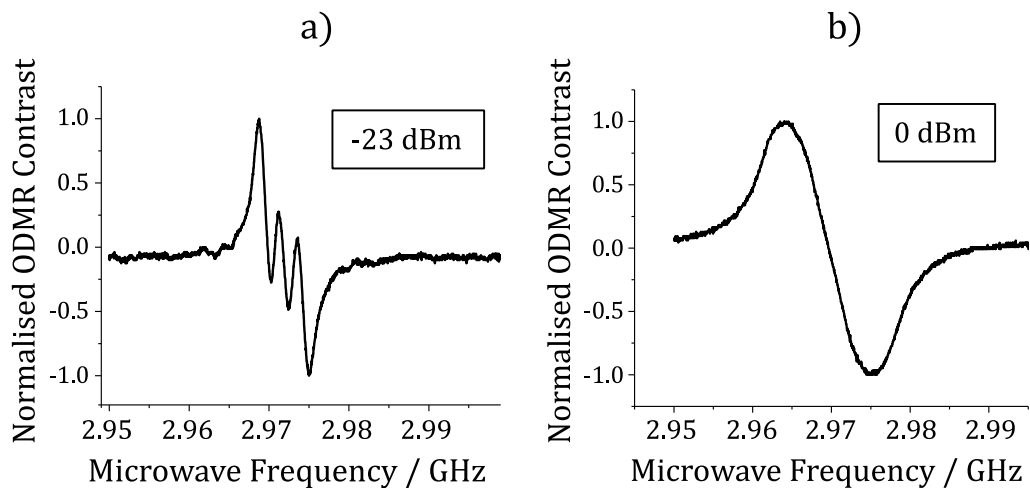


Figure 37 – ODMR spectroscopy using frequency modulation of the microwaves and a single microwave frequency. 2 mW of optical excitation was used in these measurements.

The expected dispersion-like signal is observed and again the hyperfine structure is obscured at high microwave power.

Figure 38 shows ODMR spectra taken using multi-frequency excitation and amplitude modulation. Figure 38a clearly shows the expected five peaks shown in Figure 22b thus demonstrating successful mixing of the microwaves.

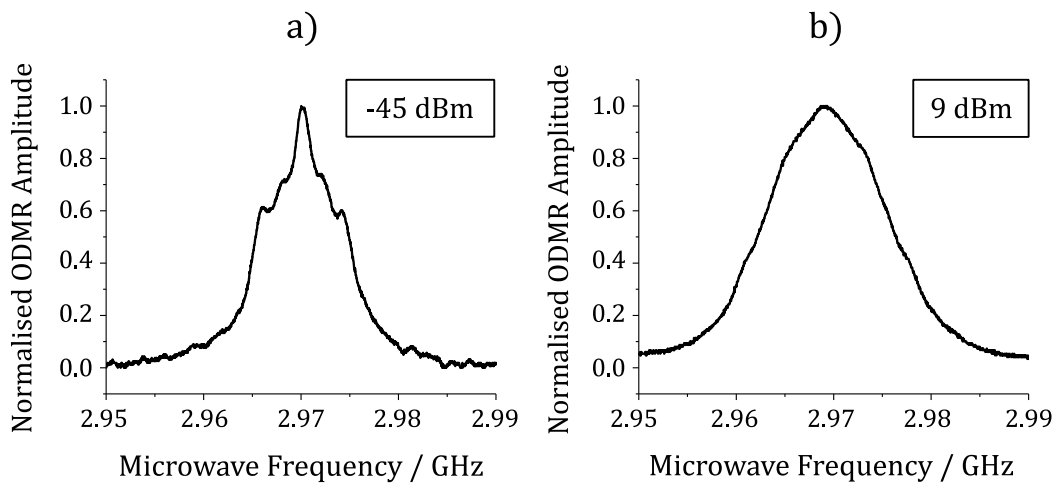


Figure 38 – ODMR spectroscopy using multi-frequency excitation and amplitude modulation of the microwaves. 2 mW of optical excitation was used in these measurements.

The expected five peaks are less defined in Figure 38b due to power broadening.

Figure 39 shows ODMR spectra taken using multi-frequency excitation and frequency modulation.

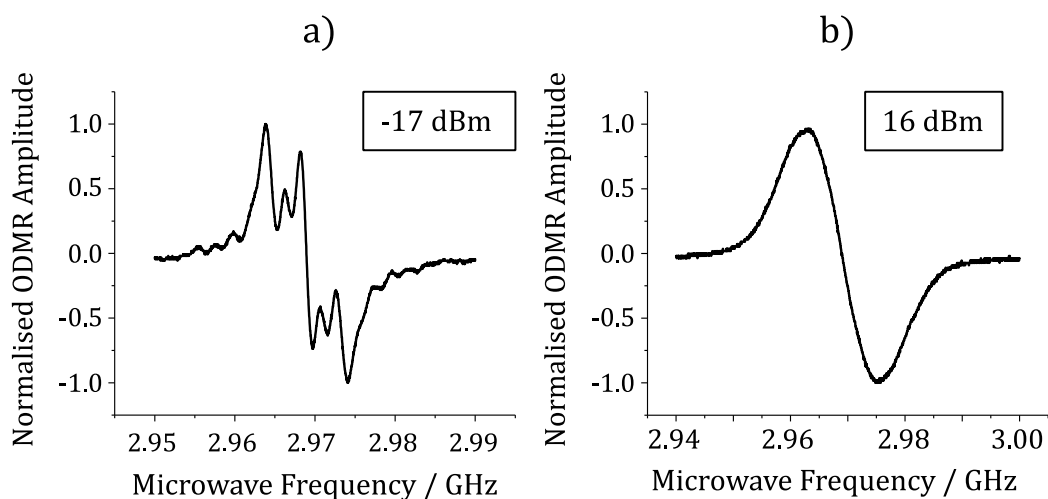


Figure 39 – ODMR spectroscopy using multi-frequency excitation and frequency modulation of the microwaves. 2 mW of optical excitation was used in these measurements.

Compared with Figure 23, the lineshape shown in Figure 39a compares reasonably well. At higher powers (Figure 39b) the hyperfine structure is again obscured by power broadening and is qualitatively similar to the spectrum shown in Figure 37b.

3.5.3 – ODMR Contrast

ODMR contrast was measured as a function of optical power at the sample, as shown in Figure 40. This was accomplished by measuring the fluorescence rate, with and without the application of resonant microwaves and calculating the percentage difference using Equation 11. These measurements were performed under ambient magnetic field conditions and used the entire ensemble. Error bars correspond to the oscilloscope resolution and DC accuracy uncertainty.

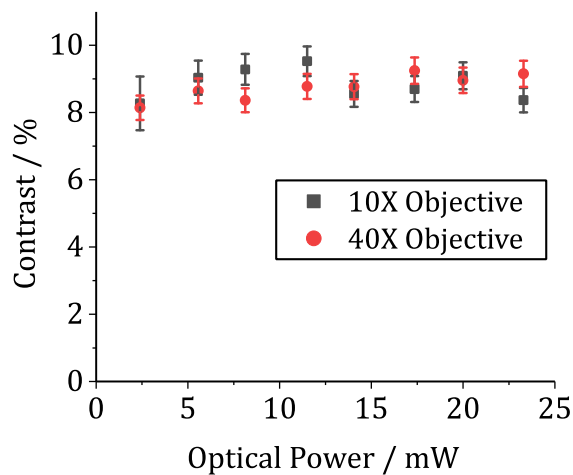


Figure 40 – ODMR contrast as a function of optical power at the sample. Full microwave power was used in these measurements.

Figure 40 demonstrates that the ODMR contrast is approximately constant over the range of powers tested. By using a 10X lens with an NA of 0.3 and a 40X lens with an NA of 0.75, a large range of optical intensities were measured. This is true as the spot size is inversely proportional to the NA of the lens [142]. In terms of ODMR contrast, there is no preferential optical intensity in this range.

3.5.4 – Magnetometric Sensitivity

Magnetometric sensitivities were determined by applying 1 kHz sinusoidal magnetic field oscillations of known amplitude (B_{measured}) and fitting the obtained magnetometry signals to a sinewave to obtain the signal voltage (V_{signal}). The RMS of the residuals of the fit were used to obtain the noise voltage (V_{noise}) and these values plugged into Equations 14 and 25 to obtain the magnetometric sensitivities.

The magnetometric sensitivity as a function of optical power at the sample, shown in Figure 41, was measured using a Thorlabs - DET36 photodiode. Error bars correspond to the standard deviation of the measurements.

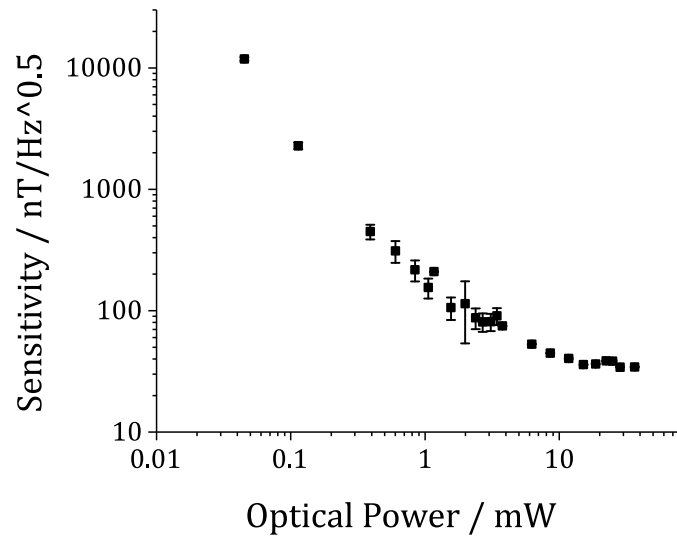


Figure 41 – Magnetometric sensitivity as a function of optical power. Full microwave power was used in these measurements.

Figure 41 shows the sensitivity is greatly enhanced by performing experiments at higher optical powers. Because the contrast is approximately constant over the measured range of optical powers, as shown in Figure 40, the increase in sensitivity is likely due to the increase in signal size. This decreases the shot-noise limit, increases the SNR out of the photodetector and allows a reduction in lock-in amplifier gain, for the same $\frac{dB}{dV_{out}}$. Sensitivity is ~ 200 nT/Hz^{1/2} at 1 mW excitation power and increases to ~ 34 nT/Hz^{1/2} at 36 mW. However, increasing the optical power is at the expense of reducing the biological applicability.

The dependence of magnetometric sensitivity on microwave power was also measured, as shown in Figure 42, using a Thorlabs - DET36 photodiode. Error bars correspond to the standard deviation of the measurements.

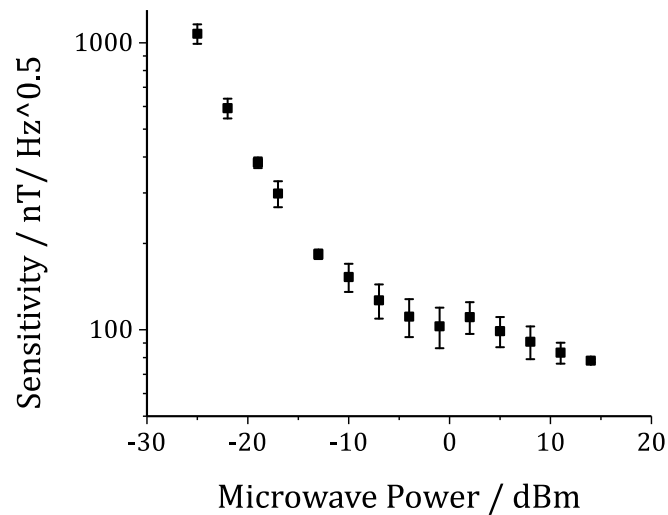


Figure 42 – Magnetometric sensitivity as a function of microwave power. 2 mW optical excitation was used in these measurements.

Figure 42 shows the magnetometric sensitivity increases with microwave power over the range available. This suggests that, even when performing experiments at maximum microwave power, the detrimental effect of power broadening the ODMR linewidth is insufficient to outweigh the benefit of the increase in contrast, shown in Figures 39 and 35 respectively. As there are no known biologically harmful effects from microwaves at these frequencies (~ 2.8 GHz), the microwave system is generally run at maximum power.

3.5.5 – Bandwidth

The bandwidth of the magnetometer was measured by applying sinusoidal varying magnetic fields of increasing frequency and measuring the detected B-field amplitude. The results are shown in Figure 43. The auto-balanced subtraction detector was used for these measurements. Error bars correspond to the oscilloscope resolution and DC accuracy uncertainty.

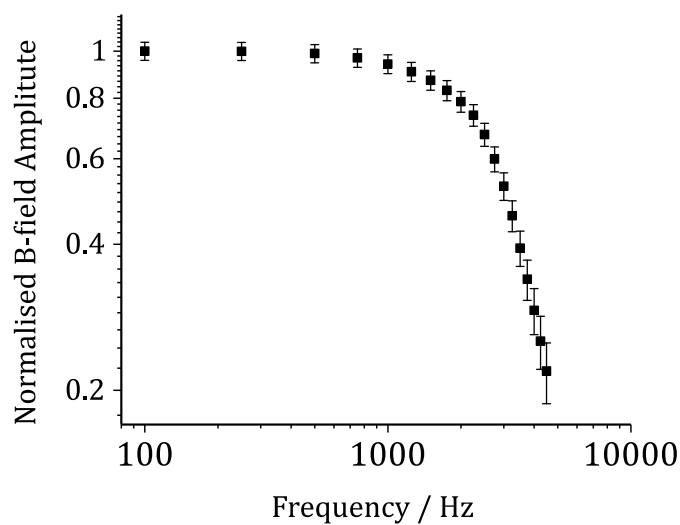


Figure 43 - Measurement of magnetometer bandwidth. Full microwave power and 2 mW of optical excitation was used for these measurements.

Figure 43 shows the frequency response of the magnetometer with a 3-dB point around 3.1 kHz.

The bandwidth was further demonstrated by measuring a 500 Hz square wave modulated B-field, as shown in Figure 44.

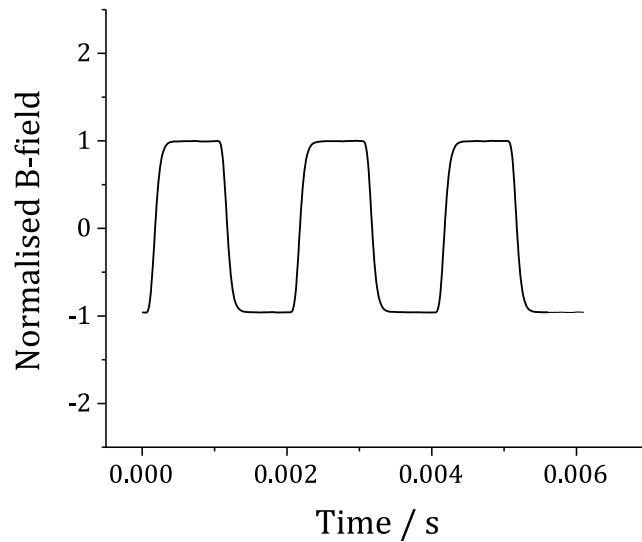


Figure 44 – Demonstration of bandwidth by measuring a 500 Hz square wave magnetic field modulation. Full microwave power and 2 mW of optical excitation was used for these measurements.

This measurement yielded a rise time of $\sim 189 \mu\text{s}$ (10% to 90%). Given the expected action potentials are $\sim 2 \text{ ms}$ in duration (500 Hz) [16], there is sufficient bandwidth for the intended measurements.

3.5.6 – Photodetectors

The achieved sensitivities for the different detectors tested are shown in Table 1. 2 mW optical power and maximum microwave power was used to characterise these.

Detector	Sensitivity (nT/Hz ^{1/2})
Commercial Auto-Balanced Subtraction Detector	66 ± 2
Subtracted TIA Photodiodes	87 ± 7
TIA Photodiode	160 ± 12
Divided TIA Photodiodes	500 ± 116

Table 1 – List of sensitivities achieved for different detectors - each detector was tested 10 times with 1, 10, and 100 s measurements of 500 nT 1 kHz sinusoidal magnetic fields and the standard deviation calculated.

There is a 1.85 times improvement when subtracting the reference signal using the lock-in amplifier 'A-B' input over using a single TIA photodiode. The division detector, although functioning, was 3.07 times worse than using a single TIA photodiode. Further investigation would be required to determine the cause. Optimisation of the signal to reference voltage ratios, multiplying gain factor and the relative phase of the signal and reference may lead to future improvements in the division detector.

The commercial auto-balanced subtraction detector showed a further 1.33 times improvement over the subtracted homemade TIA photodiodes. Given the homemade TIA photodiode circuit is very simple and costs around £20 to build, it is a more economical option over the auto-balanced subtraction detector costing over 100 times more.

An improvement in the TIA subtracted performance may be possible by performing the subtraction in the detector before entering the lock-in amplifier and could be checked in future experiments.

3.5.7 - Demonstration of Magnetometry

A measurement of a repeated magnetic field oscillation generated by 10 pulses of a 1 μA 1 kHz sinusoidal varying current over 12 hours is shown in Figure 45. This demonstrates the negative-feedback system allows measurements over long periods of time left unattended. This allows low precision, real-time measurements over long periods of time or a high precision measurement to be made by repeating measurements and averaging them. The auto-balanced subtraction detector was used for this measurement.

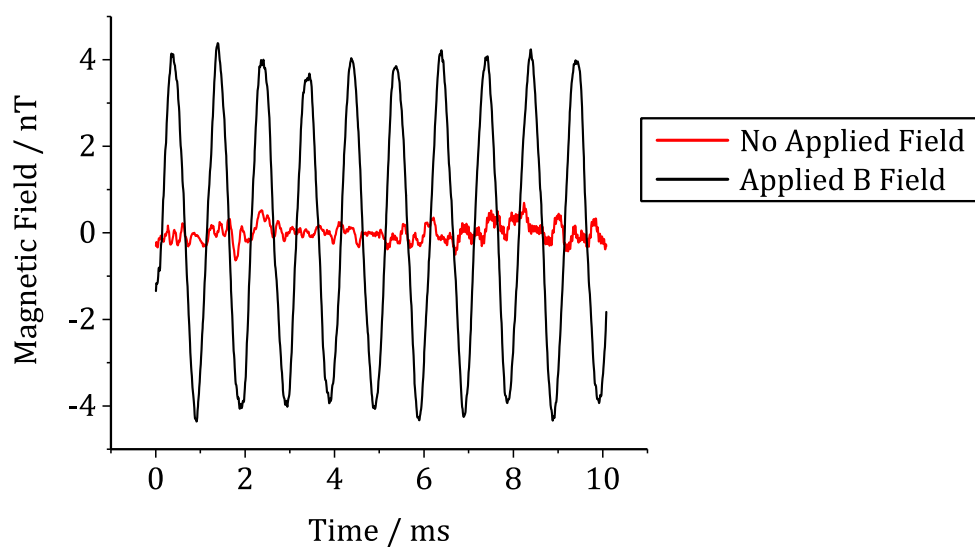


Figure 45 – Measurement of a repeated magnetic field modulation - number of measurements averaged = 4282408. Full microwave power and 2 mW of optical excitation was used for these measurements.

Figure 45 shows the magnetometer signal after averaging for 12 hours, with and without a magnetic field applied. The amplitude of the measured sinewave was 27.36

mV, giving an RMS of 19.34 mV, and the RMS of the residuals was 1.467 mV. This corresponds to measuring 10 pulses of a 1 kHz sine wave with a signal-to-noise ratio of ~ 13.2 . Given the 12 hours acquisition time, this corresponds to a sensitivity of ~ 45 nT/Hz^{1/2}.

The same experiment was performed with no applied magnetic field and the RMS voltage of the noise (V_{noise}) was measured as a function of number averaged, as shown in Figure 46.

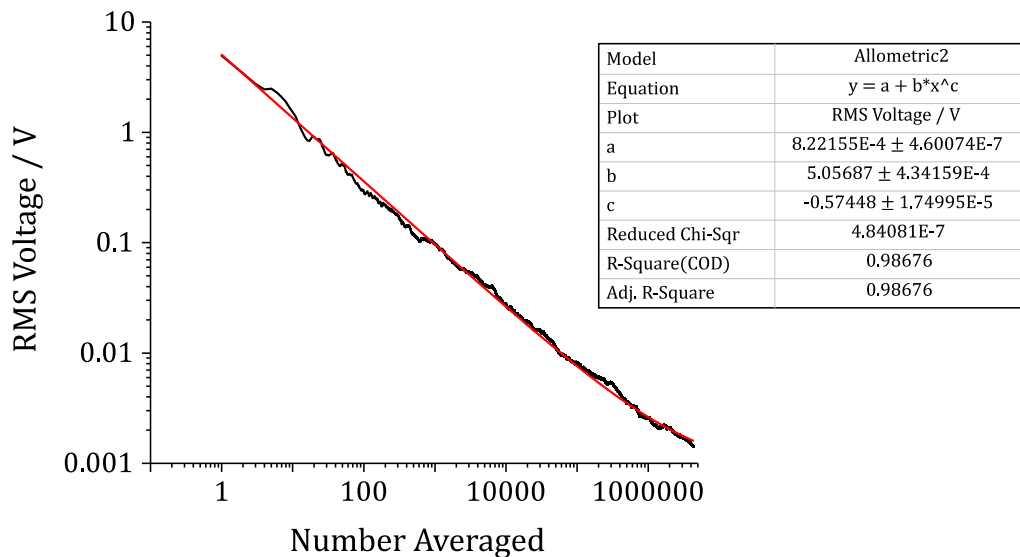


Figure 46 – RMS voltage of noise as a function of number of magnetometry measurements averaged. Full microwave power and 2 mW of optical excitation was used for these measurements.

This demonstrates that V_{noise} can decrease for at least 12 hours of acquisition time. As discussed in Section 3.4.3, the noise was expected to reduce as $\frac{1}{\sqrt{N}}$ where N is the number of measurements averaged. However, according to the fit shown in Figure 46, V_{noise} reduced as $N^{-0.57}$. This suggests the magnitude of the noise signal was not constant

throughout the measurement. This is not unreasonable given the experiment was run from ~4pm until ~4am when the laboratory temperature and seismic noise are likely to reduce. Although the general trend was as expected, this could be checked in future.

The same data is shown as B_{\min} versus averaging time in Figure 47:

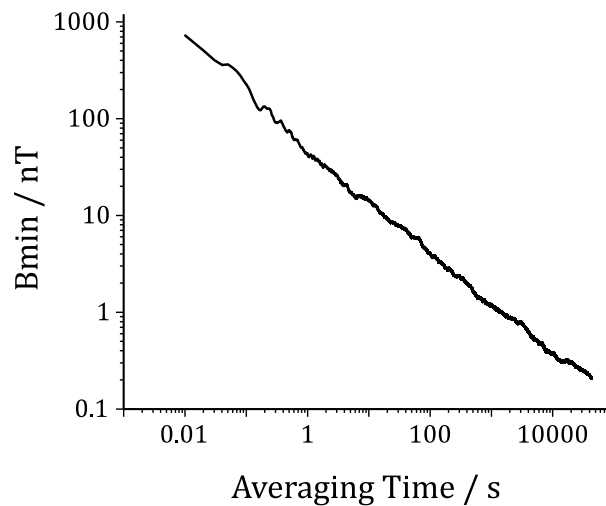


Figure 47 – Minimum detectable magnetic field as a function of averaging time. Full microwave power and 2 mW of optical excitation was used for these measurements.

At this sensitivity, a measurement of a repeated 1 nT magnetic field oscillation, with a SNR of 1, would take ~23 minutes of averaging. Measurements in real-time do not allow for averaging and would be limited to a single-shot sensitivity of fields of ~723 nT, with a SNR of 1, based on Figure 47. Reductions in laser, microwave and detector noise, an increase in sample T_2^* or optimisation of the angle between the NV measurement axis and the applied magnetic field, could increase the magnetometer sensitivity and, therefore, minimum detectable magnetic field per unit time.

3.6 – Discussion

3.6.1 - Antenna and Microwave System

As shown in Figure 34, antenna performance peaked with microstrip widths around 0.5 – 1 mm in the range tested. Although the impedance was expected to be matched around 1.5 mm, this does not account for the effect of the sample or coverslip on the antennae. It should be noted that without a circulator to measure the returned microwave power, we could not ascertain the efficiency of the antenna in general. By measuring ODMR contrast, we only gain knowledge of which antenna best coupled the microwaves to the NV centres. If using a pulsed ODMR scheme, the frequency of oscillation between the $m_s=0$ and $m_s=\pm 1$ spin states (Rabi frequency) could be measured directly to give a better understanding of the coupling strength up to and above the maximum contrast. This was not possible with the current setup as it would require an AOM to be used to pulse the excitation laser as well as an increase in the detector bandwidth to measure the sub μs changes of fluorescence.

Previous research suggests that the Rabi frequency of the magnetic dipole transition is proportional to the square root of the microwave power [89, 92, 93]. Figure 35 shows there is not a linear relationship between the square root of power out of the signal generator and the ODMR contrast. Reasons for this could include the microwave amplifier saturating or an impedance effect in the antenna at high power. However, due to the value attained, it is likely that this is an indication of reaching maximum contrast. Previously, NV⁻ ensembles were measured to have an ODMR contrast of $\sim 4\%$ [50]. Therefore, given the $\sim 4\%$ ODMR contrast achieved (Figure 35), this simple antenna

design appears to generate sufficient magnetic fields for this work. At maximum contrast, higher microwave powers are likely only to power broaden the linewidth of the transition which would be detrimental to magnetometric sensitivity.

3.6.2 - Targeted Sensitivity

The homemade transimpedance amplified photodiode measured ~ 2 V per mW of excitation with a 180 k Ω load. Based on Equation 24, this gives a measured photon rate of $R \sim 1.5 \cdot 10^{14} \text{ s}^{-1}$ for 2 mW of excitation. The measured contrast was ~ 4 % and full-width-half-maximum linewidth (Γ_{PB}) was ~ 11 MHz. Based on Equation 23, this gives a shot-noise-limited sensitivity of $\eta_{\text{CW}} \sim 639 \text{ pT/Hz}^{1/2}$. The sensitivity achieved was $66 \pm 2.2 \text{ nT/Hz}^{1/2}$ assuming a radial distance of 50 μm between the excitation region of the diamond and the core of the current carrying wire generating the magnetic field.

Estimating an uncertainty in this distance of 20 microns adds an additional uncertainty of 40 % for the magnetic field value. Adding this in quadrature with the previous uncertainty value yields an achieved sensitivity of $70 \pm 26 \text{ nT/Hz}^{1/2}$. This is 110 times above the shot-noise limit and 1129 times above the spin projection noise limit of $\sim 62 \text{ pT/Hz}^{1/2}$. The reduction in sensitivity is likely due to noise in the laser source, microwaves and detectors. The achieved sensitivity falls below the target of $0.38 \text{ nT/Hz}^{1/2}$ with which it would be reasonable to allow measurement of the action potential of a marine worm with 1 second of averaging. This is true even when using optical excitation powers over 15 times above the target of 2 mW. At 2 mW excitation power, our minimum detectable field for a single-shot measurement is $\sim 723 \text{ nT}$ with a bandwidth of 3.1 kHz. Given the shot noise limit is above our desired sensitivity, it is

not possible to achieve the required sensitivity using this technique with diamond with this T_2^* .

The successful approach by Walsworth *et al* [16] has a large advantage over the presented experimental design. By using a diamond chip containing NV centres that was not in contact with the specimen, they were able to use 2.75-4.5 W of excitation power and collect 17-28 mW of fluorescence [16]. This dramatic increase in R (signal photon rate) is greatly beneficial as shot noise sensitivity scales as $\frac{1}{\sqrt{R}}$ (Equation 23).

The disadvantage of the diamond chip design is the increased distance between the NV centres and the specimen being measured ($\sim 13 \mu\text{m}$). Given the $\sim 400 \mu\text{m}$ diameter of the marine worm axon [16], the chip approach is superior as the gain in SNR from the fluorescence is greater than the increase in B-field magnitude by reducing the distance between the sensor and specimen by $13 \mu\text{m}$.

In future, it is desirable to measure mammalian neurons that are expected to generate $\sim 1 \text{ nT}$ on their axon surface [16]. The largest nanodiamonds currently commercially available are 140 nm in diameter (Adamas Nanotechnology). The smaller particle size would result in lower fluorescence rates as there are fewer emitters. This would cause an increase in the shot-noise limit and a decrease in sensitivity compared with the current set-up. Furthermore, the excitation beam could not be focused tighter than the particle size, thus wasting power and reducing the excitation efficiency. The 140 nm particle nominally has ~ 800 NV centres, giving a spin-projection-noise-limited sensitivity of $\sim 1.05 \text{ nT/Hz}^{1/2}$ for a $T_2^*=145 \text{ ns}$. Given the action potentials are only a fraction of a second, a real-time measurement would require a single-shot sensitivity

below $1 \text{ nT/Hz}^{1/2}$. Therefore, this measurement is impossible to make in real-time with a single nanodiamond of this quality, using a CW-ESR technique.

3.6.3 - Scaling up

When using multiple micro/nanodiamonds to measure multiple neurons, each diamond has a most sensitive axis to measure from, each of which is at a different microwave frequency due to the different projections of the magnetic field for the individual NV axes. The technique used in these experiments necessitates measuring each diamond individually, in a laser scanning configuration for example, with different microwave frequencies or magnetic fields applied during the measurement of each diamond. Compared with a widefield setup, this has an inherently lower bandwidth. Furthermore, it is expected that gains in sensitivity in future are likely possible by using coherent magnetometric methods developed in the field of nuclear magnetic resonance. This would likely allow measurements closer to the spin-projection noise limit [16].

Previous research has shown that T_2^* , and therefore magnetometric sensitivity, is greatly enhanced by applying the bias magnetic field along the NV axis being measured [143]. This would also require magnetic field alignment for each diamond and re-alignment upon displacement of the diamond. Under biological experimental conditions, where the diamond could be moving, this could be very challenging.

3.7 - Conclusion

A magnetometer using a nitrogen-vacancy centre sub-ensemble contained in a single $\sim 150 \mu\text{m}$ diameter diamond was built. The sensitivity achieved was $70 \pm 26 \text{ nT/Hz}^{1/2}$ with a bandwidth of 3.1 kHz using 2 mW of optical excitation. This is 110 times above the shot-noise limit of $\sim 639 \text{ pT/Hz}^{1/2}$ and 1129 times above the spin projection noise limit of $\sim 62 \text{ pT/Hz}^{1/2}$. The reduction in sensitivity is likely due to noise in the laser source, microwaves and detectors. The sensitivity achieved in our experiment falls above the target of $0.38 \text{ nT/Hz}^{1/2}$ which could reasonably allow measurement of the action potential of a marine worm with a SNR of 1, using 1 second of averaging (84).

The experimental method would require large gains in sample quality to be useful for the intended bio-magnetometry applications. In particular, without gains in T_2^* , the long-term goal of mammalian neural sensing in real-time appears to be unattainable with a quantitative spin-projection based measurement using a single nanodiamond of this quality. Furthermore, the technique used in these experiments cannot be easily scaled up to a multiplexed widefield setup for magnetic imaging with nano/microdiamonds.

Given that the discussed experimental method does not give the required sensitivity and that the measurement of action potentials via magnetic field fluctuations need not be quantitative to be useful, future experiments using nano/microdiamond of this quality should investigate detection methods such as relaxometry [144, 145] or the electric-field detection of membrane potentials [7].

Chapter 4

Two-photon Excited Optical Detection of Magnetic Resonance of Nitrogen Vacancy Ensembles

4.1 - Overview

The previous section discussed an optical microscope system capable of performing magnetometry in the microscope's field of view. In this section, it will be demonstrated that two-photon excitation can be used to make the same type of measurement. The experiments will compare the performance of one-photon excited optical detection of magnetic resonance (ODMR), used in the previous chapter, to novel measurements of two-photon excited ODMR (2PODMR).

4.2 - Introduction

Two-photon excitation has several advantages over single-photon excitation when performing microscopy on live biological specimens. These include increased imaging depth and, due to an inhibition of fluorescence outside of the focal plane, reduced phototoxicity when performing 3D imaging [18]. Should improvements in

magnetometric sensitivity allow measurements of bio-magnetometry, it may be possible to combine NV magnetometry with the advantages of two-photon microscopy.

Although two-photon excited fluorescence of NV centres has previously been demonstrated [17, 146], 2PODMR has not. Therefore, the aim of this work was to demonstrate 2PODMR, to thus prove two-photon excited NV magnetometry feasible.

4.3 - Theory

Two-photon fluorescence is a non-linear process involving transitions between two molecular/electronic states of a fluorophore. It involves the absorption of two photons and is generally followed by emission of a single photon of greater energy [18], as depicted in Figure 48.

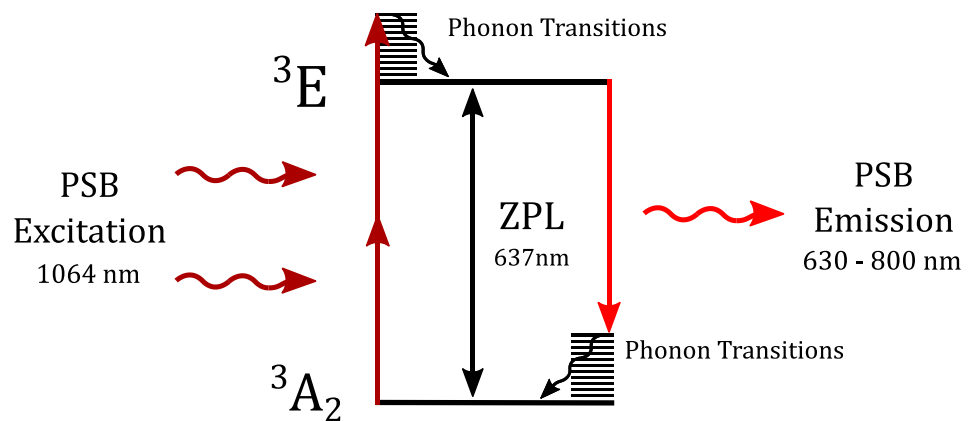


Figure 48 – Proposed mechanism of two-photon excited fluorescence of NV⁻ - excitation is via the phonon sideband (PSB) - zero-phonon line (ZPL) also shown - (based on [18, 78-80, 147]).

In terms of geometric symmetry, the NV⁻ and NV⁰ belong to the C_{3v} point group [55, 148] which is non-centrosymmetric [149]. As a result, the Laporte selection rule does not apply [150] and parity does not have to change during transitions. This allows the single photon transitions to also be excited with two-photons [17].

The number of photon-pairs absorbed from a focused and pulsed laser beam is [151]:

$$n_{2P} = \frac{\delta}{\tau f} \left(\frac{\pi NA^2}{hc\lambda} \right)^2 \langle P \rangle^2 \quad (29)$$

where δ is the two-photon absorption cross-section, τ is the pulse duration, f is the pulse repetition rate, λ is the wavelength, h is Planck's constant, c is the speed of light and NA is the numerical aperture of the objective lens. Two-photon excited fluorescence should, therefore, scale as the square of the average excitation power ($\langle P \rangle^2$). Wavelengths near 1070 nm have recently been shown to most efficiently two-photon excite NV⁻ [152]. At this wavelength, similar to the one-photon excitation spectra, NV⁰ is also efficiently excited. This suggests that, like with one-photon excitation, there are dynamic conversion processes between the NV charge states taking place.

Two-photon excited optical spin polarisation, depicted in Figure 49, is expected to be analogous to one-photon optical spin polarisation, as discussed in Section 2.2.6.

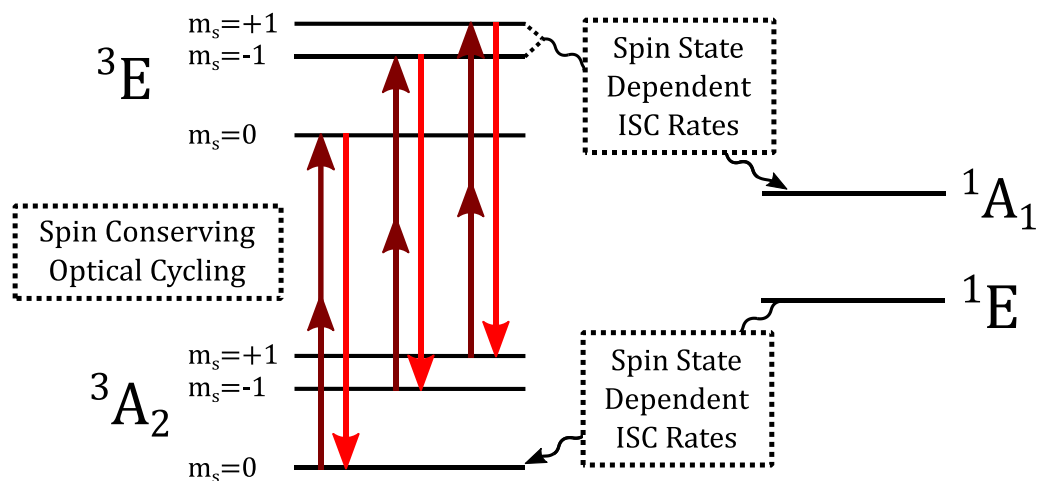


Figure 49 – Proposed mechanism for two-photon excited optical spin polarisation. NV centres are expected to optically cycle on the $^3A_2 \leftrightarrow ^3E$ transition and spin state dependant ISC (intersystem crossing) rates to cause spin polarisation into the $m_s=0$ state - based on [18, 50, 147, 153].

Because the intersystem crossing rates under 1064 nm excitation are not published, the expected 2PODMR contrast was unknown prior to measurement. However, because the ODMR contrast comes from spin-state dependent intersystem crossing rates, assuming excitation is to the same state, there is no known reason to assume they would differ from the one-photon excited intersystem crossing rates.

4.4 - Experiments

Three experiments were performed, namely measurements of emission spectra, fluorescence as a function of excitation power and 2PODMR. Measurements were made using adapted epi-fluorescence microscopy setups, as shown in Figures 50, 54 and 57. A broadband 50:50 beamsplitter was used to allow both 1064 nm and 532 nm excited

fluorescence to be measured using the same optics. This allowed comparisons to be made at the same measured fluorescence rate for either one or two-photon excitation. A Fianium – FP-1060-2-fs laser was used as the two-photon excitation source. It nominally provides 200 fs pulses at a repetition rate of 80 MHz, at a wavelength of 1064 nm, with average optical powers up to 3 W. By using a pulsed laser, the peak optical power is greatly increased over a continuous-wave laser with the same average power [153]. This increases the probability of two photons arriving at the NV centre simultaneously and, therefore, increases the two-photon excited fluorescence rate [153].

Experiments were performed using a commercially available microdiamond (Adamas Nanotechnologies - MDNV150umHi) with a nominal diameter of 150 μm and an NV⁻ concentration of 2.5 ppm. By using a microdiamond with a high concentration of NV centres, the fluorescence yield was increased. It was also found that smaller diamonds (15 μm diameter) moved from focus under high-powered 1064 nm excitation whereas the same section of the same 150 μm could be used for multiple experiments, allowing better comparison of results.

4.4.1 - Emission Spectra

4.4.1.1 - Experimental Setup

The setup used to measure emission spectra is shown in Figure 50.

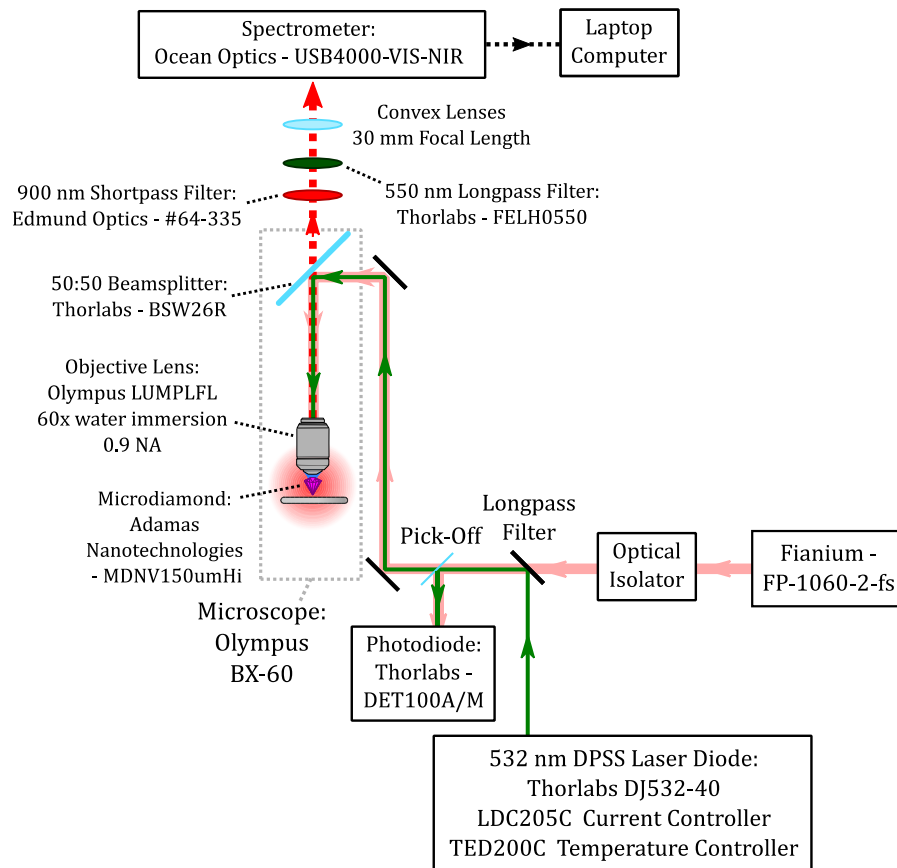


Figure 50 – Experimental setup used to measure emission spectra. 1064 and 532 nm lasers are combined with a long pass filter and coupled into a microscope. These are used to separately excite fluorescence from an NV centre doped diamond sample. Fluorescence is collected with an objective lens, long and short pass filtered to remove excitation wavelengths, and measured with a spectrometer.

A water-emersion lens was used as it had the best transmittance at 1064 nm out of the available objective lenses and was intended to be used for future measurements of bio-magnetism. The emission filters were chosen to transmit fluorescence between 550 and 900 nm. This allowed measurement of both NV^- and NV^0 fluorescence [22, 57]. Filters were chosen with relatively flat wavelength dependencies across the measurement window. This ensured an accurate measurement of the wavelength

dependency of the fluorescence. The spectrometer had a nominal resolution of 1.5 - 2.3 nm (full-width-half-maximum), which was sufficient to measure the broad emission window and features such as the zero-phonon lines. Optical powers were measured at the sample using a calibrated optical power meter (Thorlabs - PM100D, S130C, S350C) and used to calibrate beam pick-offs measured with photodiodes. These were used to monitor the excitation powers during experimentation. A long pass filter was used to combine the 532 and 1064 nm beams and an optical isolator was used to ensure no laser light was back reflected into the 1064 nm laser. For these experiments, optical power was controlled using the laser's in-built control.

4.4.1.2 - Results

The emission spectra for both 1064 nm and 532 nm excitation are shown in Figure 51. Each spectrum is normalised to its individual maximum. Results were obtained at low, medium and high powers with equivalent fluorescence rates for 532 and 1064 nm excitation.

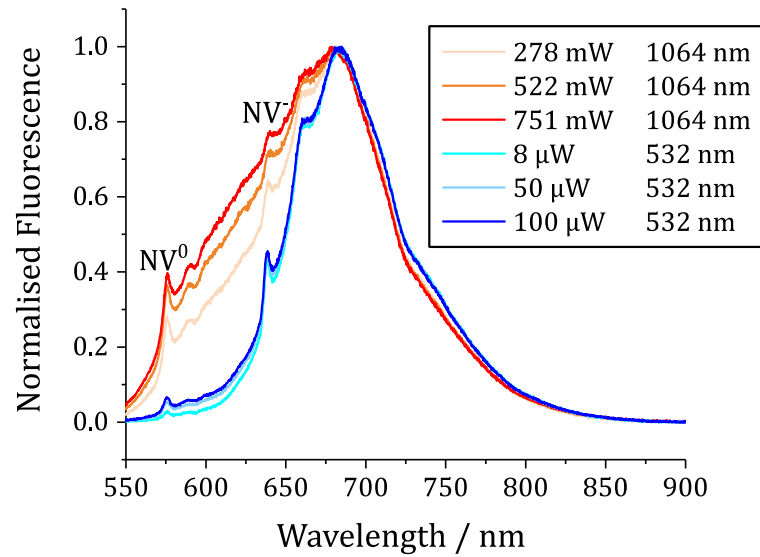


Figure 51 – Normalised emission spectra under CW 532 nm and fs-pulsed 1064 nm excitation.

Peaks at 575 nm and 637 nm can be clearly distinguished when using either 532 nm or 1064 nm excitation. These correspond to the zero-phonon lines of the NV^0 and NV^- respectively [154-156].

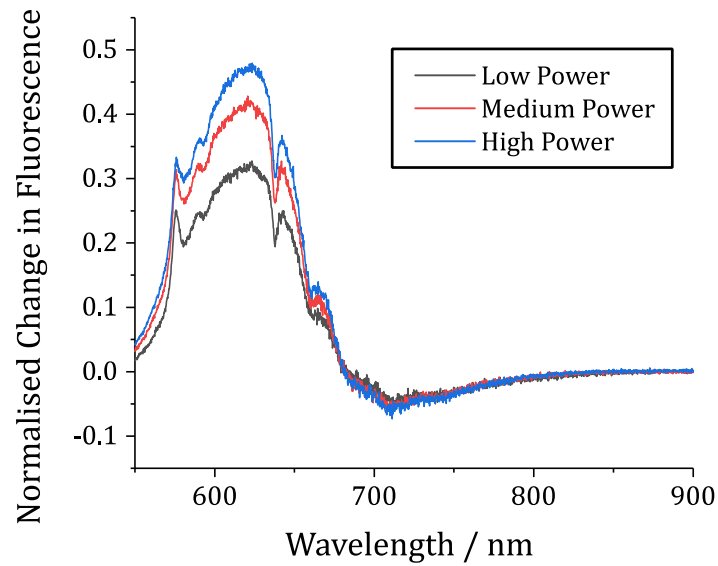


Figure 52 – Difference of CW 532 nm and fs-pulsed 1064 nm excitation spectra at different fluorescence rates. High, medium and low refer to the excitation powers shown in Figure 51.

Figure 52 shows the difference of the normalised one and two-photon emission spectra. These were obtained by subtracting the normalised one-photon spectra data from the two-photon spectra data shown in Figure 51. Increased emission at wavelengths below the zero-phonon line of the NV^- (637 nm) demonstrates NV^0 is more efficiently excited at 1064 nm than at 532 nm.

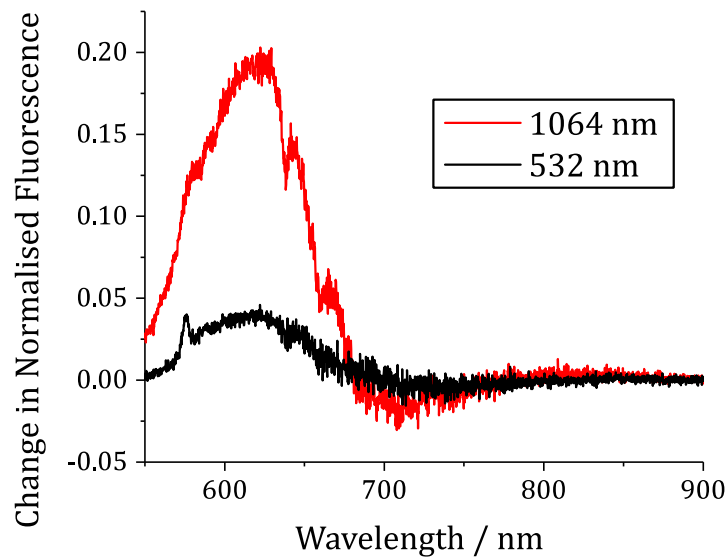


Figure 53 – Difference of emission spectra at high and low power of CW 532 nm and fs-pulsed 1064 nm excitation. High and low refer to the powers used in Figure 51.

Figure 53 shows the difference of emission spectra at the highest and lowest powers shown in Figure 51 for each excitation wavelength. This demonstrates, at either wavelength, the NV^-/NV^0 ratio decreases with increasing excitation power. This agrees with previously published results and is attributed to photoionisation of the NV^- [17, 152].

4.4.2 - Fluorescence as a function of excitation power

4.4.2.1 - Experimental Setup

The experimental setup used to measure fluorescence as a function of excitation power is shown in Figure 54.

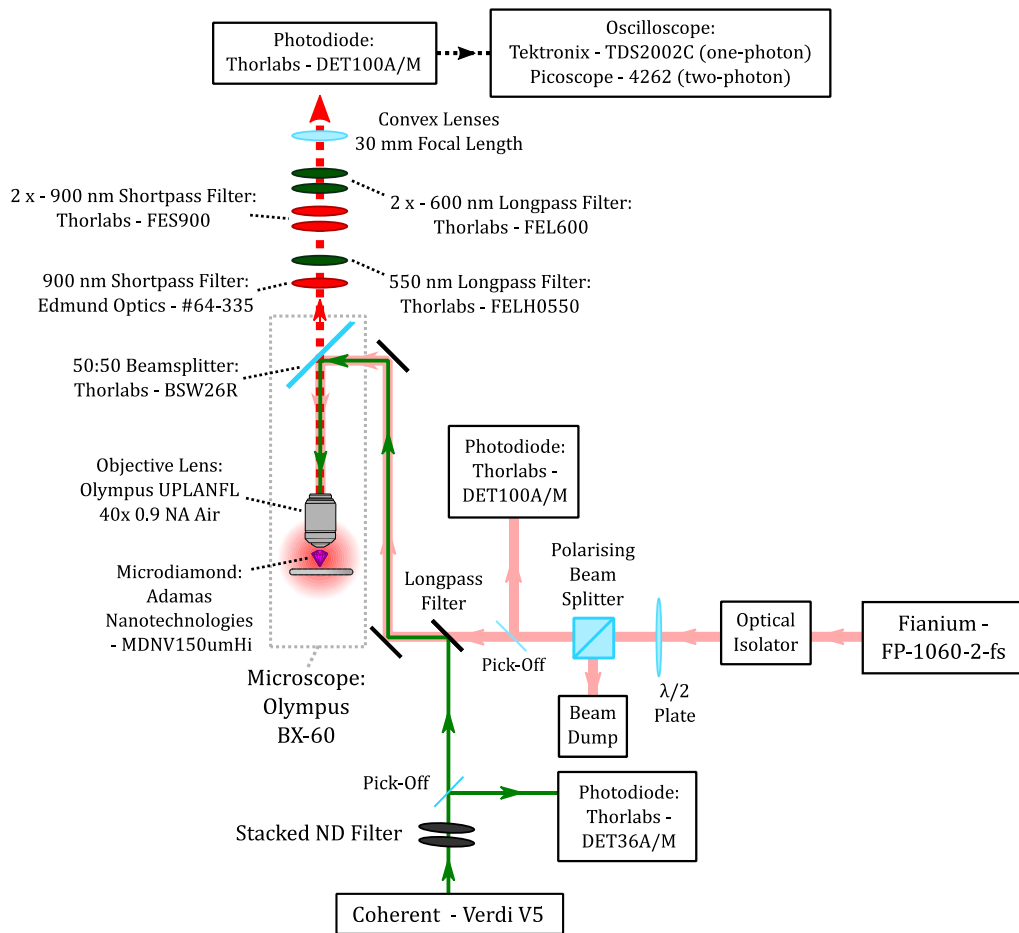


Figure 54 - Experimental setup used to measure the dependence of the fluorescence rates on excitation power. 1064 and 532 nm lasers are combined with a long pass filter and coupled into a microscope. Fluorescence is collected with an objective lens, filtered with long and short pass filters and measured with a photodiode. Optical powers are monitored with beam pick-offs measured with photodiodes.

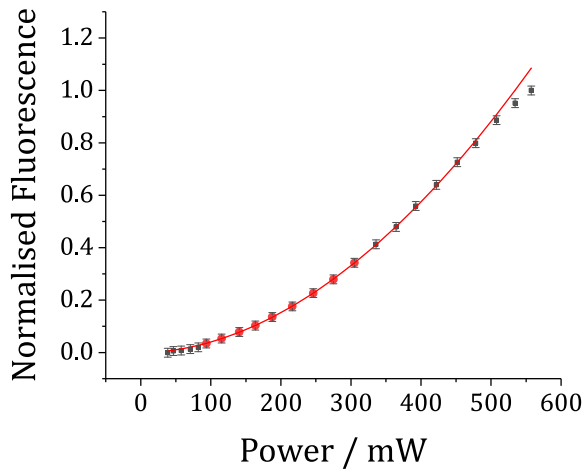
Because the diamond would move when re-applying water for the water-immersion lens, the objective lens was changed to a dry objective with the same NA. Due to the objective lens' reduced transmission at 1064 nm, the available power at the sample was reduced at this wavelength. However, it meant the same part of the diamond could be used in the remaining measurements. This allowed for a fairer comparison of results as the diamond was not polished and the transmission likely varied as a function of position on the diamond.

Further long and short pass filters were added to ensure no reflected excitation light reached the detector. A polarising beam splitter and rotatable half-wave plate were added to allow better control over the 1064 nm power levels. This also ensured the same pulse length was used throughout the experiments by constantly running the 1064 nm laser at full power. An oscilloscope (Tektronix – TDS2002C) with a 1 M Ω termination was used to measure the output of the photodiode for the one-photon excited measurements. Due to the low signal levels for the 2-photon excited measurements, a 16-bit oscilloscope (Picoscope – 4262) was used to measure the output of the photodiode. This oscilloscope also had a 1 M Ω termination allowing direct comparison of the values measured using either oscilloscope.

4.4.2.2 - Results

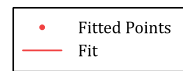
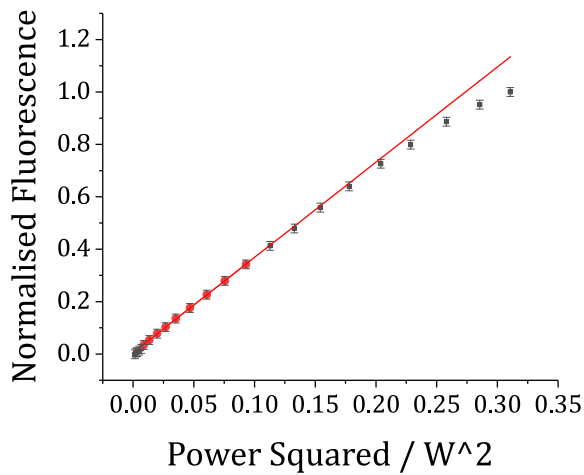
Figure 55 shows the dependence of two-photon excited fluorescence as a function of excitation power. Error bars correspond to the resolution and DC uncertainty of the oscilloscope.

a)



Model	Allometric2
Equation	$y = a + b \cdot x^c$
a	$-2.68651E-4 \pm 0.00155$
b	$5.94228E-6 \pm 7.25972E-7$
c	1.91601 ± 0.02083
Reduced Chi-Sqr	$7.70687E-7$
R-Square(COD)	0.99995
Adj. R-Square	0.99993

b)



Equation	$y = a + b \cdot x$
Plot	Fitted Points
Weight	No Weighting
Intercept	$0.00533 \pm 9.48892E-4$
Slope	3.63393 ± 0.01884
Residual Sum of Squares	$1.68952E-5$
Pearson's r	0.99991
R-Square(COD)	0.99981
Adj. R-Square	0.99979

Figure 55 – Fluorescence as a function of excitation power under fs-pulsed 1064 nm excitation. Measured using setup shown in Figure 54 – limited range fitted using Equation 30. The same y-data is plotted on a) with power on the x-axis and b) with power squared on the x-axis.

Figure 55 shows the fluorescence rate did not follow the expected simple quadratic power dependency at these excitation powers and appears to saturate. This is discussed in Section 4.5. Fits to the data from 94 to 304 mW of excitation power is shown in Figure 55. This range was chosen as the first 4 points did not fit well due to the very low signal levels and powers above 304 mW were not included due to the saturation effect. The data shows an exponent of 1.92 ± 0.02 when fitted to the equation:

$$y = a + bx^c \quad (30)$$

This confirms the excitation process is mainly due to two-photon excitation.

The dependency of the fluorescence rate on excitation power at 532 nm is shown in Figure 56. The fluorescence is normalised to the maximum two-photon excited fluorescence shown in Figure 55. 1 on this scale corresponds to 65 nW of measured fluorescence based on the generated photodiode voltage.

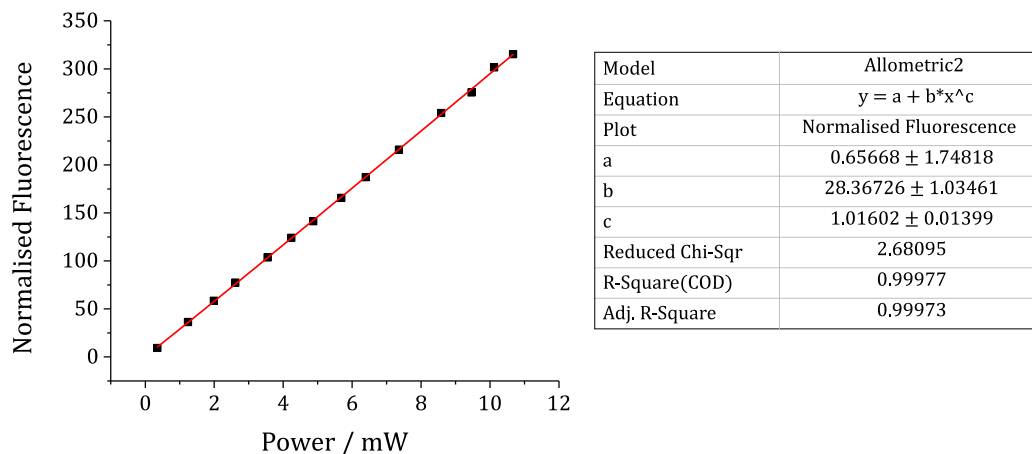


Figure 56 – Fluorescence as a function of excitation power under CW 532 nm excitation.

Figure 56 shows the 532 nm excited fluorescence data fits to equation 30 with an exponent of 1.02 ± 0.02 . This confirms the fluorescence is due to one-photon excitation. Furthermore, the data shows that at least two orders of magnitude more fluorescence can be achieved using one-photon excitation versus two-photon excitation with no evidence of saturation.

4.4.3 - Two-photon Excited ODMR (2PODMR)

4.4.3.1 - Experimental Setup

The experimental setup used to measure 2PODMR is shown in Figure 57.

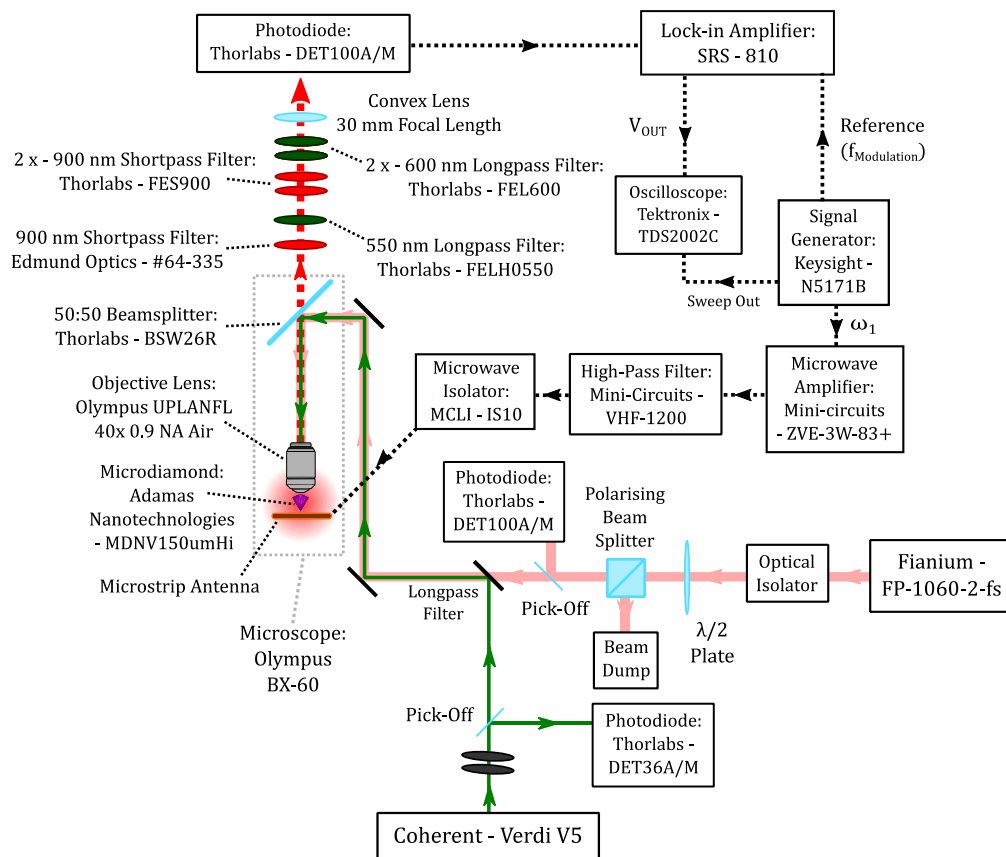


Figure 57 – Experimental setup used to measure 2PODMR. 1064 and 532 nm lasers are combined with a long pass filter and coupled into a microscope. Fluorescence is collected with an objective lens, filtered with long and short pass filters and measured with a photodiode. ODMR spectra are produced by applying and sweeping microwaves whilst measuring laser induced fluorescence. The fluorescence signal is processed by a lock-in amplifier, referenced to the microwave modulation rate, to produce the ODMR spectra.

A signal generator was used to generate square-wave amplitude-modulated microwaves. Modulation was performed using the in-built modulation function of the signal generator. These were passed through a high-pass filter to remove the modulation frequencies, an amplifier to increase the microwave power and an isolator to prevent back reflections into the amplifier. Microwaves were applied to the NV

centres via the microstrip antenna described in Section 3.4.4, and the microwave frequency swept from 2.75 to 3 GHz. The modulation depth was 100 % to maximise contrast and the acquisition time was two minutes per sweep. The fluorescence was measured with a photodiode connected to a lock-in amplifier referenced to the amplitude modulation rate. A modulation rate of 223 Hz and a time constant of 300 ms were used on the lock-in amplifier. The optimum phase setting was found to be the same for both excitation wavelengths and the same settings were used for both measurements. To enable comparison of one and two-photon excited ODMR, the same DC voltage (~30 mV) was inputted to the lock-in amplifier for both measurements. This ensured differences in ODMR amplitude corresponded to differences in ODMR contrast. However, this was not corrected for the different NV^-/NV^0 ratios.

4.4.3.2 - Results

Measurements of both one-photon excited ODMR and 2PODMR are shown in Figures 58 and 59.

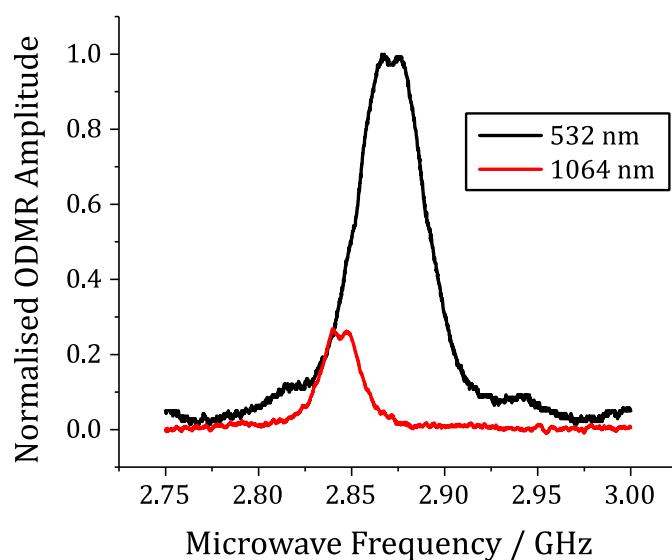


Figure 58 – One-photon excited ODMR and 2PODMR measured at the same fluorescence rate. Measured with 557 mW of 1064 nm and 26 μ W of 532 nm excitation at the sample.

A Gaussian fit to each spectrum yields an amplitude ratio (2P/1P) of 26.3 %. The reduction in ODMR contrast can be partially explained by the decreased NV^-/NV^0 ratio shown in the emission spectra. However, for this to fully account for the reduction in contrast would require there to be more NV^0 fluorescence than NV^- . This can be discounted by the emission spectra shown in Figure 51. Figure 59 shows the same data as Figure 58 but shown on separate Y-scales.

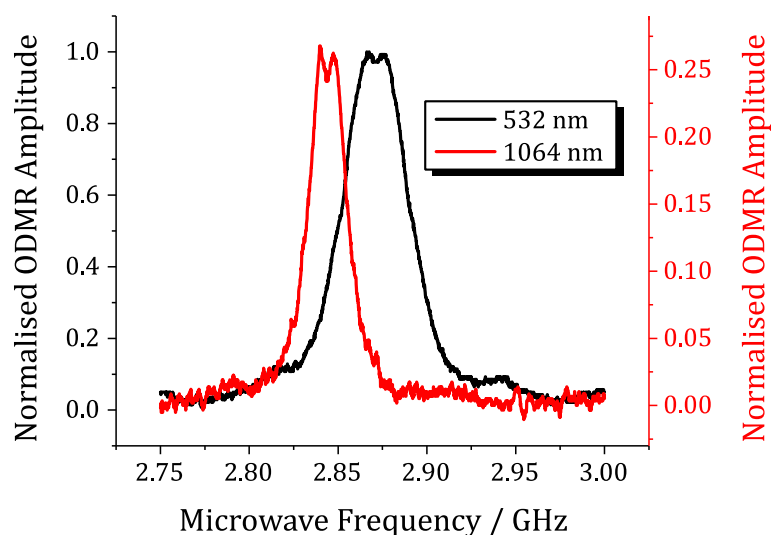


Figure 59 – One-photon excited ODMR and 2PODMR at the same fluorescence rate on separate y-axes. Same data as Figure 58.

Figure 59 clearly shows both a reduction in linewidth and shift of the resonance when using 1064 nm excitation. A Gaussian fit to each spectrum yields a linewidth ratio of 60.4 % and a shift of the ODMR resonance of -27 MHz. Previous work with similar HPHT diamond has shown laser intensities up to 36 mW mm^{-2} resulted in sample heating up to 372 K [157]. It is, therefore, reasonable to assume there is significant heating of the samples tested in the presented experiments. Using a polynomial approximation of the temperature dependence of the zero-field splitting [158], the shift of -27 MHz corresponds to a temperature of $\sim 520 \text{ K}$ ($\sim 247 \text{ }^\circ\text{C}$) during the two-photon excited measurement. At this temperature, previous measurements have shown an approximately 22 % reduction in single-photon excited ODMR contrast [158].

4.5 - Discussion

2PODMR was successfully demonstrated using a nitrogen-vacancy ensemble contained in a single microdiamond. This conclusively demonstrates the viability of two-photon excited magnetometry using NV centres. The 2PODMR contrast was found to be reduced by 73.7 % and the 2PODMR linewidth was found to be reduced by 39.6 % when compared with measuring single-photon excited ODMR at the same fluorescence rate.

Two-photon excited fluorescence was also demonstrated to saturate at far lower fluorescence rates than under one-photon excitation (Figures 55 and 56). As discussed in Section 3.3.4, the CW-ESR shot-noise limit scales as $\frac{1}{\sqrt{R}}$, where R is the detected photon rate. The low fluorescence rate under two-photon excitation, compared with that under one-photon excitation, would, therefore, limit the achievable magnetometric sensitivity.

The reduction in two-photon excited fluorescence is likely due to recently discovered processes that cause one-photon excited fluorescence to quench under simultaneous 532 and 1064 nm excitation [155, 159, 160]. Recent research has confirmed multiple processes under simultaneous 532 nm and 1064 nm excitation which can both increase and decrease NV⁻ fluorescence rates [155]. These depend on optical intensity and relate to both thermal and NV⁻ ↔ NV⁰ conversion processes [155]. Unlike in previous research, in the presented results, the two-photon excited fluorescence appears to be quenched by the same laser that is exciting the fluorescence.

The measured reduction in ODMR contrast of 73.7 % is not trivial to explain with the presented experimental data. Assuming that, due to the elevated temperature, there is the same reduction in ODMR contrast under one and two-photon excitation, a drop in ODMR contrast of 22 % is expected [158]. To account for the additional 51.7 % reduction in contrast would require there to be an NV^-/NV^0 ratio of ~ 34 %. This is ruled out by the emission spectra shown in Figure 51 and suggests that there is another reason for the reduced 2PODMR contrast.

A likely candidate is that high optical excitation powers caused heating of the microwave antenna. This could potentially cause a change in the antenna's impedance and a corresponding reduction in microwave coupling efficiency. To test whether heating of the antenna reduces its efficiency, using a microwave circulator, the microwave power back-reflected from the antenna could be measured as a function of excitation power/temperature.

To mitigate any heating of the microwave antenna under high excitation power, a loop antenna that is not in contact with the diamond could be used. This may require increased microwave powers to maintain the same contrast as the distance between the antenna and NV centre is increased.

Another possibility for the reduced 2PODMR contrast is that the excited state intersystem crossing rates may differ for the two excitation wavelengths. Measurements of intersystem crossing rates have been made under 532 nm excitation [161] and could be repeated under 1064 nm excitation in future experiments.

The reduction in 2PODMR linewidth was unexpected and is not currently understood. Compared with one-photon excitation at the same fluorescence rate, lower linewidths under two-photon excitation would increase magnetometric sensitivity. Therefore, this is potentially a very interesting avenue of investigation for future work.

It may be the case that there is preferential optical excitation of certain NV axes taking place due to the polarisation dependency of two-photon excitation [147]. Experiments should be repeated as a function of angle of polarisation and with circular polarisation for the optical excitation. Experiments should also be repeated with a bias magnetic field applied to allow measurement of the individual sub-ensembles. This would allow the ODMR contrast of the individual NV axes to be compared. Furthermore, measurement of a single sub-ensemble ODMR linewidth would provide a definitive demonstration of a reduction in linewidth.

By repeating experiments with aggregates of nanodiamonds under both one and two-photon excitation, effects owing to the orientation of the diamonds should be averaged out. This may also provide insight when compared with single crystal results.

A reduction in ODMR linewidth under increasing 532 nm excitation has previously been reported [89] and may also be related. This could be tested by repeating measurements as a function of excitation power, starting at lower excitation powers.

Given the successful demonstration of 2PODMR conclusively demonstrates two-photon excited spin polarisation, a two-photon excited version of recent spin-to-charge readout protocols [104] should be possible. This could be an interesting avenue of investigation for future two-photon excited magnetometry research using NV centres.

Future work could also demonstrate coherent spin state control of NV centres under two-photon excitation to verify the viability of coherent two-photon excited magnetometry. This would be best performed with high quality CVD diamond samples.

Although the experimental setup was adequate to measure 2PODMR, several improvements could be made. Given the low fluorescence rate, an avalanche photodiode or photomultiplier would likely be a more suitable photodetector for these measurements. With greater optical detection sensitivity, measurements could be made at lower optical excitation powers and bandpass filters could be used to differentiate fluorescence contributions from NV^- and NV^0 .

To allow a better comparison between one and two-photon excited fluorescence rates, a confocal setup should be employed to reject out of focus fluorescence. This likely has a far greater contribution to the one-photon excited fluorescence signal as two-photon excitation is only probable in the focus of the 1064 nm excitation beam and not from scattered light.

Finally, temperature control of the sample, such as use of a cold finger [155], could be implemented to mitigate thermal effects.

4.6 - Conclusions

Two-photon excited optical detection of magnetic resonance (2PODMR) has been successfully demonstrated using a nitrogen-vacancy ensemble contained in a single

microdiamond. This conclusively demonstrates the viability of two-photon excited magnetometry using NV centres.

The 2PODMR contrast was found to be reduced by 73.7 % when compared with measuring single-photon excited ODMR at the same fluorescence rate. This can only partially be explained by the increased temperature and lower NV^-/NV^0 fluorescence ratio under two-photon excitation. The 2PODMR linewidth was also found to be reduced by 39.6 %, though the mechanism is not currently understood.

Evidence of saturation of two-photon excited fluorescence was found at rates at least two orders of magnitude lower than under one-photon excitation. This is assumed to be related to thermal and $NV^- \leftrightarrow NV^0$ conversion processes demonstrated under simultaneous 532 nm and 1064 nm excitation [155].

Chapter 5

Stimulated Emission from Nitrogen Vacancy

Ensembles in Bulk Diamond

5.1 - Overview

The previous two sections discussed the development of a niche magnetometer using nitrogen-vacancy centres in a fluorescence microscopy setup for biological research. In this section, research towards a novel and more general magnetometer that also uses the optical detection of magnetic resonance (ODMR) will be discussed.

This work takes early steps towards building a magneto-sensitive laser using nitrogen-vacancy centre doped diamond as the laser gain material. Such a laser is expected to allow ultra-sensitive measurements of magnetic fields [23]. This could be useful for a variety of applications such as mapping of the earth's magnetic field, the detection of submarines, shipwrecks and mines, and ex-vivo bio-sensing applications such as electrocardiographic (heartbeat) and electroencephalographic (brain activity) sensing [50].

The first two sections describe attempts to measure stimulated emission from a nitrogen-vacancy centre ensemble, under both non-resonant and resonant excitation. This would demonstrate the fundamental process on which the proposed laser would

be built. The third section describes attempts to use stimulated emission to perform ODMR. This would demonstrate the magneto-sensitivity of the proposed laser.

5.2 - Introduction

Magnetometry using ensembles of nitrogen-vacancy centres can rely on measurements of small changes in fluorescence intensity [16, 162]. As fluorescence is generally emitted in all directions, achieving high collection efficiencies is challenging. A typical 25 mm diameter lens with a 35.1 mm focal length in air and a high-quality oil-immersion objective lens with an NA of 1.4, have maximum fluorescence collection efficiencies of 3.4 % and 31 % respectively [163, 164]. In contrast, a theoretical 100 % collection efficiency of light generated by stimulated emission is possible as the photons are emitted into a single mode. Furthermore, stimulated emission from NV centre ensembles could allow the creation of a laser using diamond as an optical gain medium [165]. This is attractive for both its excellent thermal conductivity as well as an ability to output in proportion to shifts of the NV⁻ magnetic resonance [23]. Based on this principle, a room temperature magnetometer has recently been proposed with an expected sensitivity near $1 \text{ fT}/\text{Hz}^{1/2}$ [23].

Whilst this work was being undertaken, a successful demonstration of stimulated emission from a nitrogen-vacancy centre ensemble was reported [22]. Although the efficiency was not quantified, it was accompanied by indirect evidence of stimulated emission. This included a reported reduction in fluorescence with nanosecond-scale temporal dynamics and a wavelength dependency proportional to the fluorescence emission spectrum. Previously, there have been several demonstrations of super-

resolution imaging using stimulated emission depletion microscopy with nitrogen-vacancy centres [38, 68, 166]. As these rely on stimulated emission to suppress fluorescence, it is further indirect evidence of stimulated emission from NV centres.

The aim of this research was to directly quantify the optical gain of a probe beam due to stimulated emission from a nitrogen-vacancy centre ensemble contained in a mm scale diamond. A secondary aim was to perform the optical detection of magnetic resonance (ODMR) using stimulated emission. This would demonstrate the feasibility of using stimulated emission to perform magnetometry.

5.2.1 - Diamond Samples

The diamonds used in the presented experiments and the information in Table 2 was provided by the Institute of Photonics (University of Strathclyde). Substitutional nitrogen concentrations were determined using Fourier-transform infrared spectroscopy and the concentration of the other defects were determined by absorption spectroscopy at 77 K [90].

Sample #	Name	Pre-Treated Ns Conc. (ppm)	NVN Conc. (ppm)	NV ⁻ Conc. (ppm)	NV ⁰ Conc. (ppm)	V ⁰ Conc. (ppm)	Size (mm)
1	1409E6 sCVD02	4.5	0.069	0.549	0.578	0.088	2.93x3.08x1.85
2	1409E6 sCVD04 -01	4.5	0.495	0.313	0.099	0	1.5x1.5x1.8
3	E6H3A	7	0.06	0.76	0.13	0	2.96x2.97x2.16

Table 2 –Diamond Specifications:

Ns = substitutional nitrogen, NVN = nitrogen-vacancy-nitrogen, V⁰ = neutral vacancy
- data provided by the Institute of Photonics (University of Strathclyde)

All samples were synthesised using chemical vapour deposition by Element6 and approximately 2x2x3 mm in size. Additional treatments including electron irradiation and annealing were performed by the Institute of Photonics. Sample #2 has undergone the same treatment as sample #1 except for an additional high-pressure, high-temperature treatment. Details of similar samples created by the Institute of Photonics can be found at the following reference [90]. Although sample #3 looks to have the best specifications, it was unavailable when the measurements in Sections 5.3.1 and 5.3.3 were performed.

5.3 - Experiments

Experiments to measure stimulated emission and ODMR using stimulated emission were initially performed using 532 nm excitation. Due to inconclusive results, a measurement of stimulated emission using resonant 637 nm excitation was subsequently attempted.

5.3.1 – Attempts to Measure Stimulated Emission under 532 nm Excitation

5.3.1.1 - Theory

Stimulated emission is an optical process whereby an incident photon causes an excited fluorophore to emit a photon in the same direction, with the same polarisation and in-phase with the incident photon [167]. As two photons are now in the mode of the incident photon, optical amplification has occurred. This is depicted in Figure 60.

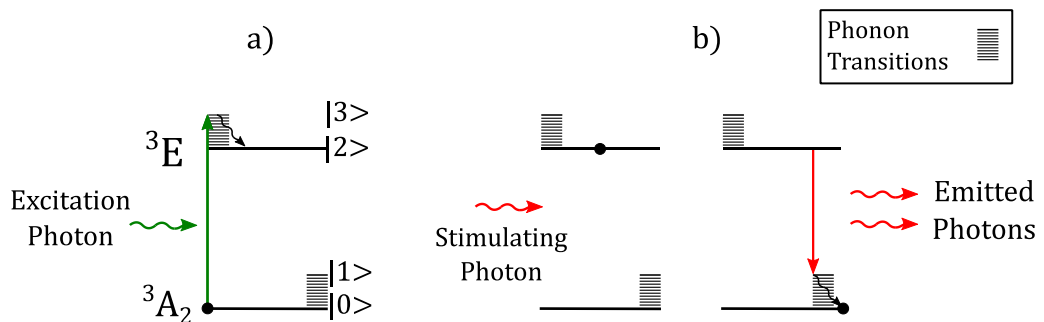


Figure 60 – a) Excitation via the phonon sideband (based on [78]). A 532 nm photon excites the NV centre first to $|3\rangle$ before it decays to $|2\rangle$.
 b) Process of stimulated emission (based on [78, 142, 168]) – stimulating photon causes de-excitation of an NV centre and the emission of a photon.

The loss or gain of a flux of photons passing through a medium can be described as the absorption or stimulated emission of photons respectively. Spontaneous emission has a negligible contribution to gain as photons are emitted in all directions [142]. The rate of

change of a flux of photons at a position z in a gain medium can be described using the following equation [142]:

$$\frac{dF}{dz} = \sigma_{\text{tran}}(N_2 - N_1)F(z) \quad (31)$$

where σ_{tran} is the transition cross section, $F(z)$ is the photon flux at position z and N_1 and N_2 are the population densities of the $|1\rangle$ and $|2\rangle$ states respectively, as shown in Figure 60. With $N_2 > N_1$, optical amplification occurs whereas, with $N_1 > N_2$, absorption occurs [142]. The requirement of $N_2 > N_1$ is known as population inversion. This should be easily achievable as, neglecting the NV^\cdot singlet states, the NV^\cdot is a 4-level system with fast decaying $|3\rangle$ and $|1\rangle$ states relative to state $|2\rangle$, from which stimulated emission should occur. Therefore, in theory, it requires only a single NV^\cdot to be pumped to create population inversion [142].

The stimulated emission cross-section (σ_{stim}), as a function of wavelength (λ), is defined as “the laser gain of a transition per unit population inversion in the absence of saturation or excited state absorption” [169]. It can be calculated using the following equation [169]:

$$\sigma_{\text{stim}}(\lambda) = \frac{\eta \lambda^5 I(\lambda)}{\tau_f (\int \lambda I(\lambda) d\lambda) f_2 8\pi n^2 c} \quad (32)$$

where η is the radiative quantum efficiency of the excited state, $I(\lambda)$ is the fluorescence emission spectrum, c is the speed of light, n is the refractive index and:

$$f_2 = \frac{N_{\text{pumped}}}{N_2} \quad (33)$$

where N_{pumped} is the population density of NV^- in all the pumped states, including the ^3E and singlet states. τ_f is the fluorescence lifetime of the excited state which is defined as the mean time the fluorophore remains in the excited state, including radiative and non-radiative emission processes [170].

As the stimulated emission cross section has a wavelength dependency proportional to that of the fluorescence emission spectrum, at room temperature, stimulated emission from NV^- is expected to most efficiently occur at the peak of the phonon sideband near 700 nm [22].

NV^- centre based lasers, which use stimulated emission as the optical amplification process, are expected to be pumped into the excited ^3E state via excitation on the phonon sideband at 532 nm [23], as shown in Figure 60a. A 532 nm pump is typical of many previous magnetometry experiments using NV^- [16, 39, 162].

For pump and probe intensities well below saturation, the optical gain in an ideal 4-level laser gain material can be described with the following equation [171]:

$$G = \frac{\sigma_{\text{stim}} \tau_f P_{\text{abs}}}{h \nu_{\text{pump}} A_p^*} \quad (34)$$

where P_{abs} is the absorbed pump power, h is Planck's constant, ν_{pump} is the frequency of the pump light and A_p^* is the effective pump area.

The fraction of absorbed pump power to incident pump power can be estimated from the following equation [171] :

$$P_{\text{frac}} = 1 - e^{-\sigma_{\text{abs}}NL} \quad (35)$$

where σ_{abs} is the absorption cross-section at the pump wavelength, N is the fluorophore density and L is the length of the gain material.

Using Equation 35, the absorbed pump power can be calculated [171]:

$$P_{\text{abs}} = P_{\text{applied}}P_{\text{frac}} \quad (36)$$

where P_{applied} is the applied pump power.

The effective pump area is related to the overlap integral of the pump and probe beams and can be approximated by [171]:

$$A_p^* = \frac{\pi}{2} \left(\overline{W}_{\text{pump}}^2 + \overline{W}_{\text{probe}}^2 \right) \quad (37)$$

where $\overline{W}_{\text{pump}}$ and $\overline{W}_{\text{probe}}$ are the average pump and probe radii respectively [171].

For the NV; $\sigma_{\text{abs}} = 3.1 \times 10^{-17}$ at 532 nm [17], $\sigma_{\text{stim}} = 3.6 \times 10^{-17} \text{ cm}^2$ [172], $\tau_f \sim 13 \text{ ns}$ [77], the samples used had a length of $\sim 2 \text{ mm}$ and the pump and probe radii were 47 and 21 μm respectively. Using Equations 34-37, the expected gain as a function of pump power can be calculated and is shown in Figure 61.

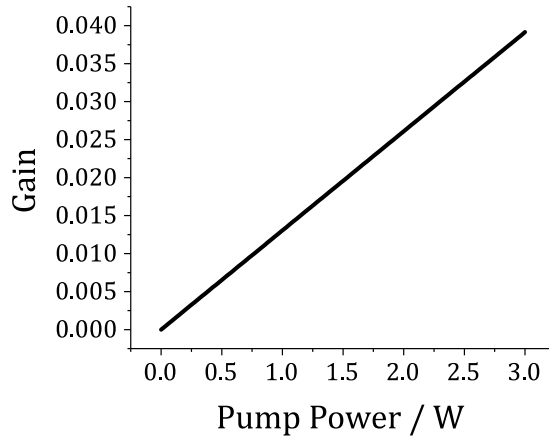


Figure 61 – Expected gain as a function of pump power for diamond sample with an NV-concentration of 0.5 ppm.

Based on Equation 34, the gain is expected to increase linearly with pump power and should be invariant to probe power, assuming you are well below the probe saturation intensity. For a 4-level system, this can be calculated from the following expression [173]:

$$I_{\text{sat}} = \frac{h\nu_{\text{probe}}}{\sigma_{\text{stim}}\tau_f} \quad (38)$$

Using Equation 38, the saturation intensity is $\sim 0.59 \text{ MW cm}^{-2}$ at 723 nm.

5.3.1.1.1 - Reference Sample

For these experiments, titanium:sapphire was chosen as a reference sample to ensure the apparatus was working as expected. It was chosen as it is a commonly used and commercially available laser gain material that can be pumped at 532 nm and

fluoresces around the same wavelength range as NV^- . Furthermore, neglecting the NV^- singlet states, both titanium:sapphire and the NV^- are 4-level systems and should exhibit similar behaviour. For the titanium:sapphire sample, the doping concentration was nominally 0.25 % by weight, which corresponds to a density of $\sim 8.25 \times 10^{19} \text{ cm}^{-3}$ [174]. The fluorescence lifetime of titanium:sapphire is $\tau_f = 3.2 \mu\text{s}$ [175], absorption cross section at 532 nm is $\sigma_{\text{abs}} = 4.9 \times 10^{-20} \text{ cm}^2$ [176], peak stimulated emission cross section $\sigma_{\text{stim}} = 3 \times 10^{-19} \text{ cm}^2$ [172] and the sample had a length of 15 mm. At 723 nm, the stimulated emission cross section is about 0.85 times that of the peak [174]. Using these numbers and Equation 34, the gain using titanium:sapphire was expected to be ~ 4.1 times larger than that with diamond containing an NV^- concentration of 0.5 ppm.

5.3.1.2 - Experimental Design

A simplified experimental setup designed to measure a change in probe power due to stimulated emission is shown in Figure 62.

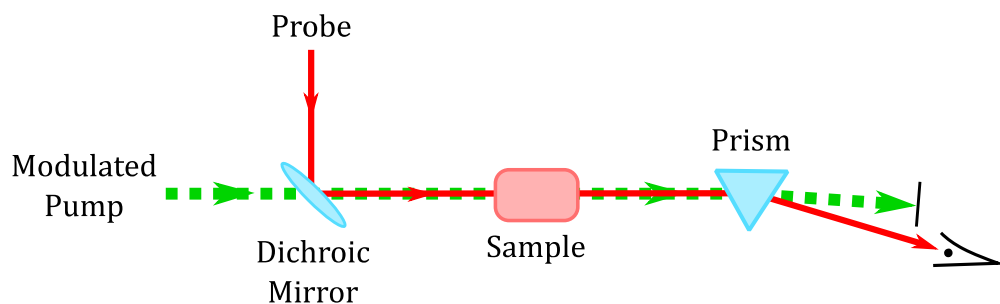


Figure 62 – Simplified experimental setup for measurements of a change in probe power. Pump and probe beams are combined using a dichroic mirror, passed through the sample, and the probe measured after separation from the pump.

A modulated pump beam is overlapped with a continuous wave (CW) probe beam using a dichroic mirror and passed through a sample. The normalised powers before passing through the sample are shown in Figure 63.

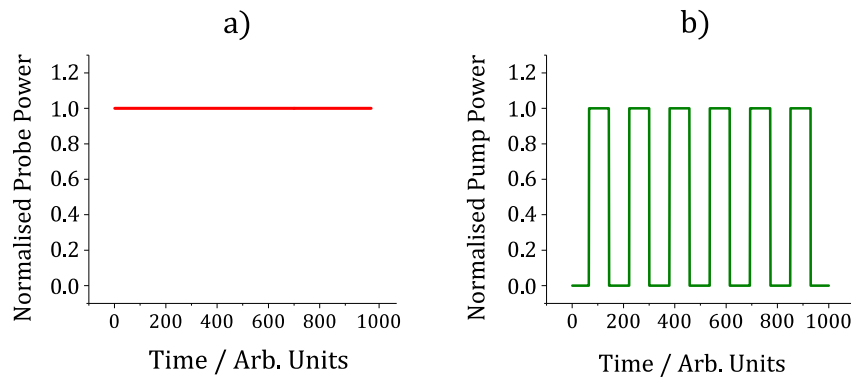


Figure 63 – Normalised probe and pump power as a function of time before passing through the sample.

After passing through the sample, the beams are separated using a prism and the probe power measured as a function of time. If stimulated emission occurs, the probe beam should exhibit increased power in phase with the pump excitation as shown in Figure 64.

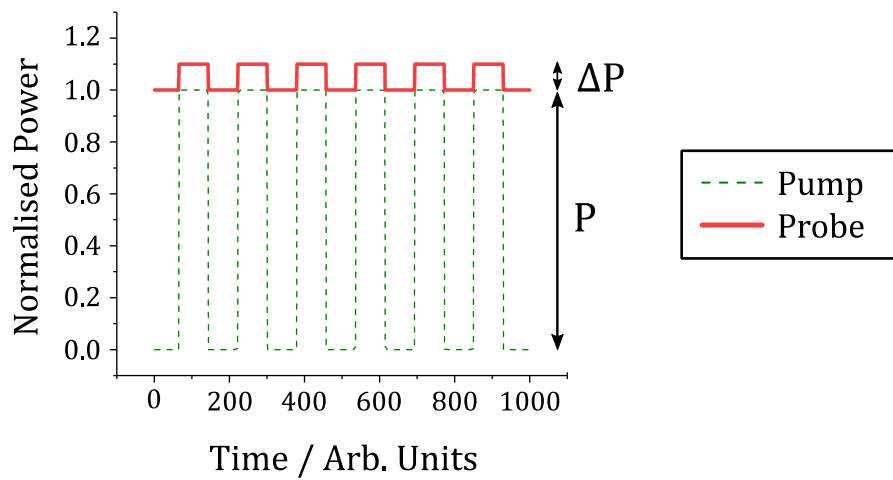


Figure 64 – Expected experimental output – 10% relative gain. Probe power is expected to increase in phase with the pump power due to stimulated emission.

This allows measurement of the probe power gain, relative to the pump being on and off, where:

$$\text{relative gain} = \frac{\Delta P}{P} \quad (39)$$

As stimulated emission can only occur when the sample is in the excited state, when the pump beam is turned off, stimulated emission is expected to cease on a timescale comparable with the fluorescence lifetime of the state. At room temperature, this is ~ 13 ns [77] for the NV $^-$ and 3.2 μ s for titanium:sapphire [175].

5.3.1.3 - Experimental Setup

The experimental setup designed to measure stimulated emission is shown in Figure 65.

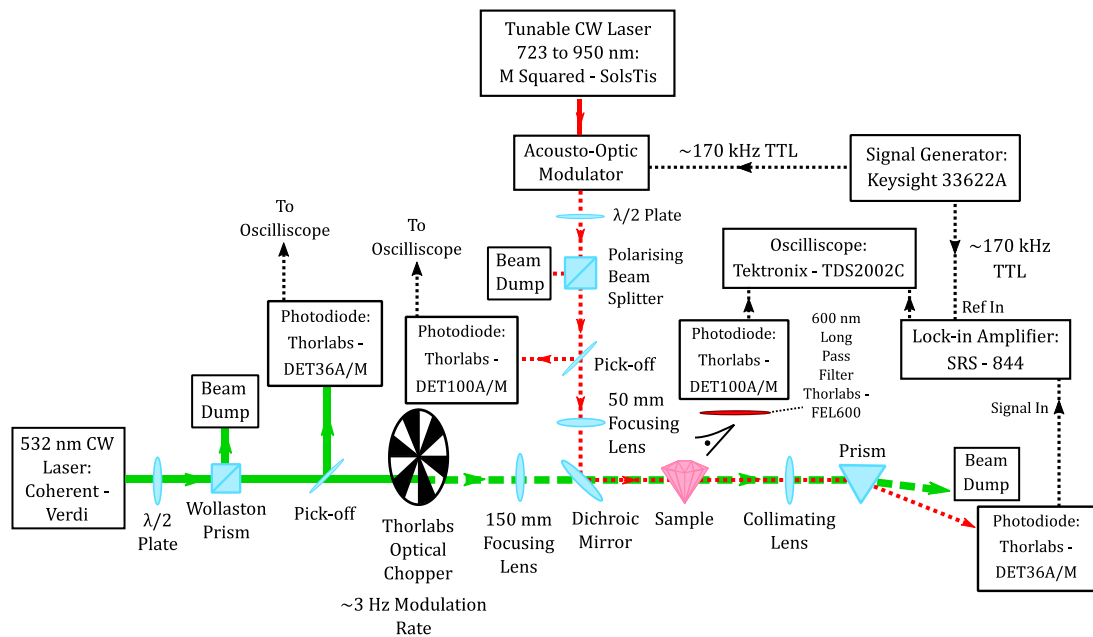


Figure 65 – Experimental setup used to measure stimulated emission with a 532 nm pump wavelength. Modulated pump and probe beams are combined using a dichroic mirror, passed through the sample, and the probe measured with a photodiode after separation from the pump using a prism. Modulation of the pump is achieved using an optical chopper, and the probe using an acousto-optical modulator. Demodulation of the probe is achieved using a lock-in amplifier referenced to the probe modulation rate and is recorded with an oscilloscope.

To mitigate imperfect separation of the pump and probe, both the pump and probe were modulated. This enabled a lock-in amplifier to isolate the probe signal from any fluorescence or pump light that may have reached the detector. This was possible by

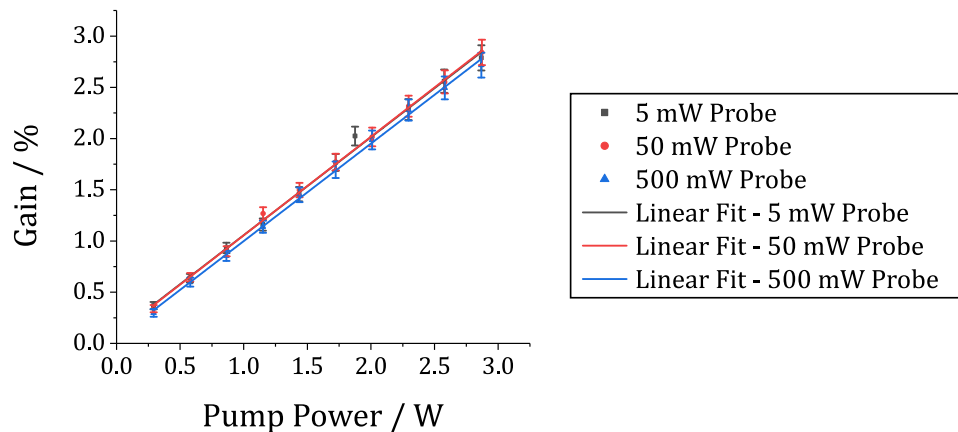
modulating the probe at a high frequency (~ 170 kHz) relative to the pump modulation rate of 3 Hz. An integration time-constant (1 ms) over 100 times shorter than the pump modulation period was chosen on the lock-in amplifier to enable a high signal-to-noise ratio measurement with sufficient bandwidth to measure the low-frequency modulation. The probe was amplitude modulated using an acousto-optic modulator and the pump was modulated using a mechanical chopper. Both were approximately square wave modulated with a 50% duty cycle and 100% modulation depth. The beams were combined using a dichroic mirror and separated using a prism. Fluorescence was used to measure when the pump was on and off for comparison with the probe beam modulation. A commercial tunable CW laser was used as the probe source to allow measurements at several wavelengths. Pump and probe powers were controlled using a $\lambda/2$ plate and Wollaston prism and polarising beam splitter respectively. Optical powers were measured at the sample using a calibrated optical power meter (Thorlabs - PM100D, S305C, S350C) and used to calibrate beam pick-offs measured with photodiodes. These were used to monitor the pump and probe powers during experimentation. The sample sat on a microwave antenna to allow the ODMR experiments described in Section 5.3.3 without having to move the sample. Beam diameters were 93 and 41 μm for the pump and probe respectively. These were measured using a Cinogy - CinCam CMOS (complementary metal-oxide-semiconductor) beam profiler.

5.3.1.4 - Results

Results for titanium:sapphire are presented first, followed by results with diamond sample #1 and #2. Error bars in this section correspond to the resolution and DC uncertainty of the oscilloscope.

5.3.1.4.1 - Titanium:sapphire

Figure 66 shows a measurement of relative gain as a function of pump power using a 723 nm probe.



Equation	y = a + b*x		
	Gain / %	Gain / %	Gain / %
Plot			
Weight	No Weighting		
Intercept	0.10046 ± 0.03668	0.09342 ± 0.02207	0.04734 ± 0.02266
Slope	0.95653 ± 0.02078	0.96226 ± 0.01239	0.95197 ± 0.01272
Residual Sum of Squares	0.02298	0.0083	0.00875
Pearson's r	0.99812	0.99934	0.99929
R-Square(COD)	0.99624	0.99868	0.99857
Adj. R-Square	0.99577	0.99851	0.99839

Figure 66 – Measurement of relative gain using titanium:sapphire.

The sample exhibited gain with the expected linear dependence on pump power. Figure 67 shows the dependence on probe power.

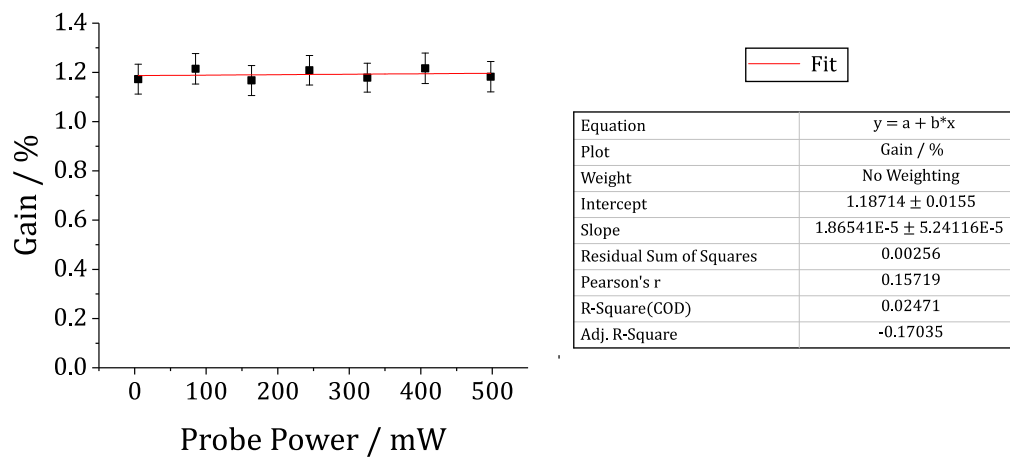


Figure 67 – Measurement of relative gain as a function of probe power. 1.25 W pump power was used.

As expected, the sample gain did not depend on the probe power as shown by the fitted gradient of $(2 \pm 5) \times 10^{-5}$ (Figure 67). The probe was therefore below saturation over the range of powers used. Figure 68 shows the temporal dependence of the relative gain.

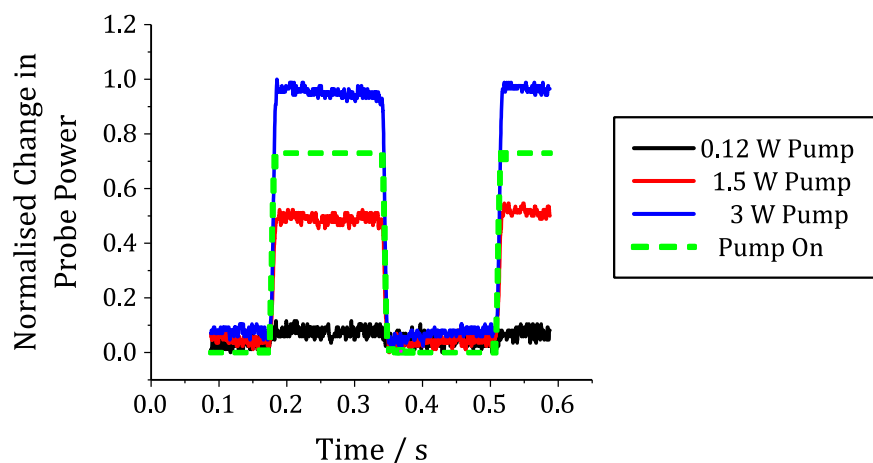


Figure 68 – Change in probe power as a function of time – probe wavelength of 723 nm and power of 5 mW was used.

Due to the lock-in amplifier time constant of 1 ms, the experimental setup was not capable of measuring sub-ms changes in fluorescence. Therefore, it was not possible to verify the fluorescence lifetime of the excited state ($3.2 \mu\text{s}$ [175]). However, Figure 68 confirms the increase in probe power was in phase with the pump, as expected.

The measurements with titanium:sapphire suggest the experimental apparatus worked as expected.

5.3.1.4.2 - Diamond Sample #1

Figure 69 shows that diamond sample #1 generally exhibited a relative loss when the pump was applied. This was true at all wavelengths tested. However, Figures 69a and 69b show, at 820 and 950 nm respectively, a relative increase in probe power was measured. This suggests multiple processes are being optically driven by the pump and

probe beams. Furthermore, the dependencies of the change in probe power as a function of pump power were found to be non-linear.

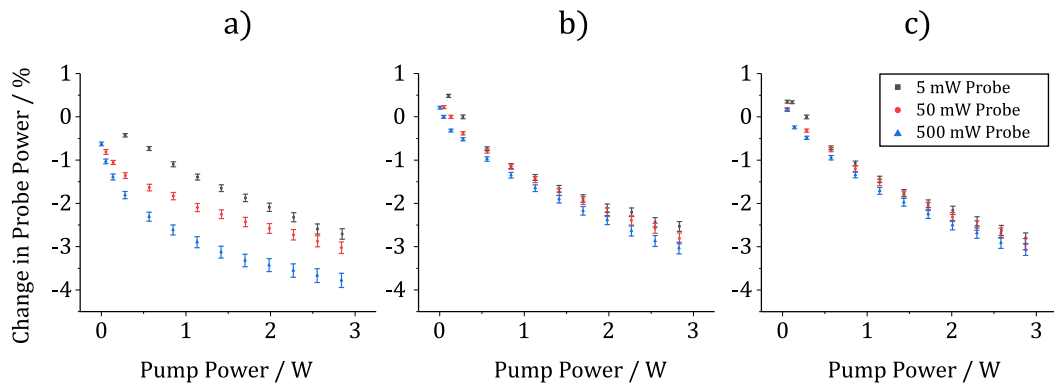


Figure 69 – Change in probe power as a function of pump power with a) 723, b) 820 and c) 950 nm probes.

Figure 70 shows a non-linear dependency on probe power at 723 nm and relatively flat dependencies at 820 and 950 nm. This suggests different processes may be occurring at the different wavelengths.

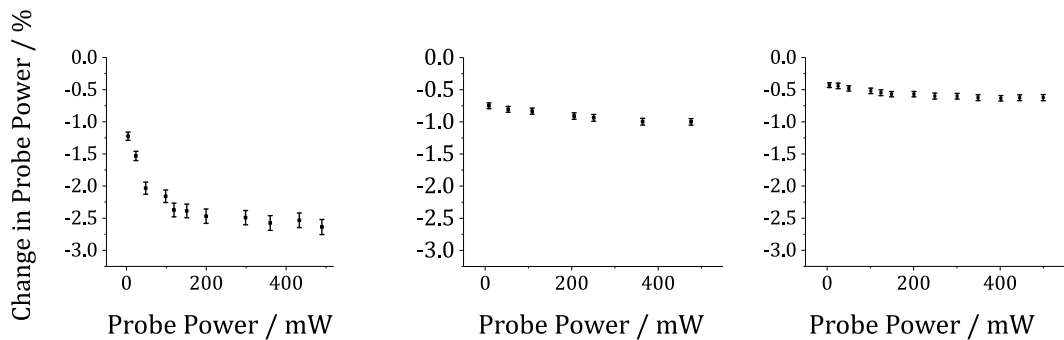


Figure 70 – a) Change in probe power as a function of probe power with 723 nm probe (0.72 W pump), b) 820 nm probe (0.58 W pump) and c) 950 nm probe (0.45 W pump).

Figure 71 shows the change in probe power as a function of time. Modulation of the probe beam is generally out of phase with the pump beam except at the lowest pump powers with 820 nm and 950 nm probes. Furthermore, the sample did not return to its equilibrium value on a timescale consistent with the lifetime of the NV⁻ excited state (~13 ns [50]). This was regardless of the pump power applied and is discussed in Section 5.3.1.5.

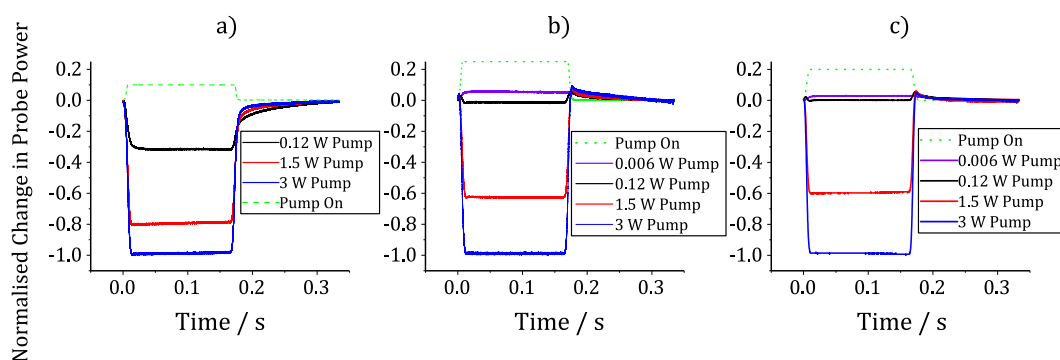


Figure 71 – Change in probe power as a function of time (512 averaged) with a) 723, b) 820 and c) 950 nm probes, all at 400 mW.

The measured relative loss suggests either increased absorption of the probe beam when the pump was applied or that the diamond exhibited increased reflectivity when in a pumped state.

5.3.1.4.3 - Diamond Sample #2

Figure 72 shows that diamond sample #2 exhibited relative gain when the pump was applied. This was true at all wavelengths tested.

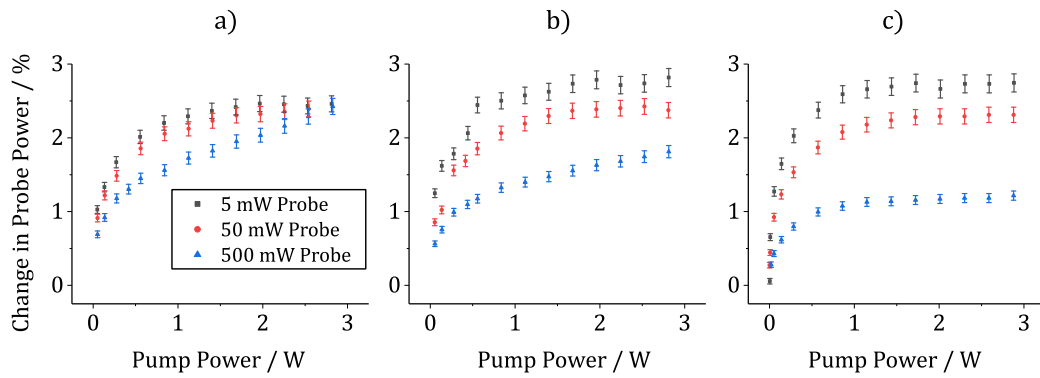


Figure 72 – Change in probe power as a function of pump power with a) 723, b) 820 and c) 950 nm probes.

This suggests either stimulated emission, a reduction in probe absorption or reduced reflectivity when the sample was in the pumped state. The dependencies on probe power were also non-linear, as shown in Figure 73.

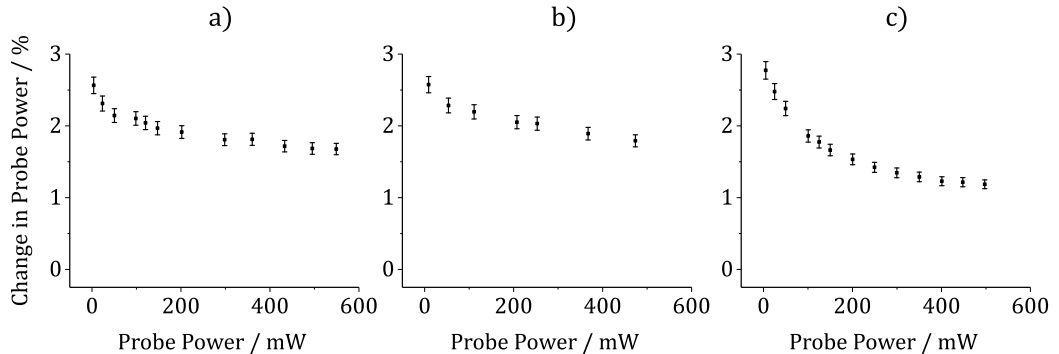


Figure 73 – Change in probe power as a function of probe power with a) 723 nm probe (1.2 W pump), b) 820 nm probe (1.15 W pump) and c) 950 nm probe (1.44 W pump).

The relative gain of sample #2 is demonstrated in Figure 74 by a modulation of the probe beam which is in phase with the pump beam. However, with this sample, the

probe power also did not return to its equilibrium value on a timescale consistent with the lifetime of the NV⁻ excited state.

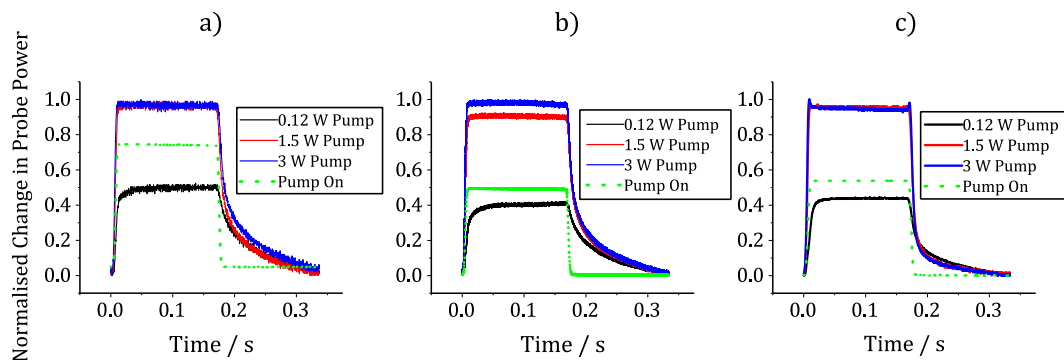


Figure 74 – a) Change in probe power as a function of time (512 averaged) with 723 nm at 5 mW, b) 820 nm at 800 mW and c) 950 nm at 400 mW probes.

5.3.1.5 – Discussion

Figures 69 to 71 show that diamond sample #1 generally exhibited a relative loss of probe power when in the pumped state. This is clearly not indicative of stimulated emission which was expected to cause optical gain. Figures 72-74 show that diamond sample #2 showed a relative increase in probe power when in a pumped state, however, also showed wavelength, temporal and power dependencies that were unexpected. Given it is not currently clear what processes are being measured, it is not clear which models to fit the data from Sections 5.3.1.4.2 and 5.3.1.4.3 to. Therefore, analysis remains primarily qualitative at present.

Based on the NV emission spectrum [22, 57], the stimulated emission cross section was expected to be relatively high at 723 nm, low at 820 nm and near zero at 950 nm.

The wavelength dependencies demonstrated in Figures 69 and 72 do not reflect this. This suggests that the predominant effect responsible for the change in probe power is not stimulated emission.

Previously, the phonon sideband of the NV^- singlet state transition (${}^1E \rightarrow {}^1A_1$), with zero-phonon line at 1042 nm, has been measured to extend to at least 800 nm at 10 K [177]. Absorption of this transition could, at least partially, be responsible for the loss of probe power. Figure 73c shows an increased non-linearity compared with 64a and 64b. This is consistent with increased absorption of the singlet state transition at 950 nm [177]. However, this was not observed in diamond sample #1.

One major difference between these samples, according to Table 2, was that sample #1 contained an almost equal concentration of NV^0 to NV^- . Recent studies have demonstrated a reversible $NV^0 \rightarrow NV^-$ conversion process using excitation wavelengths of 900 to 1000 [127] and 1064 nm [155]. Given the considerably larger NV^0 concentration in diamond sample #1, this may be responsible for the overall loss of probe power when pumped. Furthermore, at increased powers, these wavelengths can also contribute to an increased $NV^- \rightarrow NV^0$ conversion rate [127, 155, 159]. Another study has shown that 780 nm excitation can also increase $NV^- \rightarrow NV^0$ conversion rates [126]. All these processes would require absorption of the probe. Furthermore, they should contribute to relative loss as they are driven from the excited states of the NV^- . These processes are far less likely when the pump is not applied as, at the probe wavelengths, there is insufficient energy to drive the $NV^- \text{ } {}^3A_2 \rightarrow {}^3E$ transition or $NV^0 \text{ } {}^2E \rightarrow {}^2A$ transition (Figure 7) with a single photon. It would, therefore, require two-photon excitation of these transitions. Without full knowledge of the wavelength,

timescales and power ranges over which these processes can be driven, it is not possible to quantify their relative contributions to the presented results.

Figures 71 and 74 show unexpected time dependences on the change in probe power at all wavelengths tested and in both diamond samples. The timescales involved for the signal to return to its unpumped equilibrium is greater than 100 ms. This is many orders of magnitude longer than the nano-second scale expected and inconsistent with a measurement of stimulated emission. Figure 68 shows the titanium:sapphire sample did not exhibit the same behaviour, indicating this is not an experimental artefact.

Previous research has demonstrated NV charge state recovery with time scales ranging from $\sim 100 \mu\text{s}$ [178] to $\sim 450 \text{ s}$ [179] depending on the NV concentration. These processes occurred when in the unpumped state and are presumed to be related to tunnelling [124, 178]. The $100 \mu\text{s}$ timescale was for an NV concentration of $\sim 45 \text{ ppm}$ and the 450 s was for CVD diamond with no treatment to increase NV concentration. The NV concentration used in the presented experiments likely falls in between these two values. Therefore, the timescales in the presented results may be consistent with charge state recovery. This could be tested in future experiments by using a yellow readout laser to measure NV fluorescence as a function of time between pump pulses [178]. This could be performed with and without the 723 to 950 nm probe beam to determine its effect.

Future experiments could also measure the change in probe power as a function of pump power at increasing modulation rates. The presented experiments focussed on low frequency modulation to highlight the difference in behaviour between titanium:sapphire and diamond. It may be the case that the longer timescale processes

would be filtered from results at higher modulation rates and more linear dependencies on pump power would be observed. The effect of angle of polarisation between the pump and probe may also alter the relative efficiencies of the processes being monitored and could be measured in future.

For diamond sample #1, Figure 71a shows the temporal behaviour of the 723 nm probe was qualitatively different from that at 820 and 950 nm, shown in Figures 71b and 71c respectively. This may be related to the neutral vacancy (V^0) which has a phonon sideband peaking at 725 nm [180] and has previously been demonstrated to exhibit non-linear absorption [181]. Figure 70a shows a much greater non-linearity in the probe power dependency compared with those shown in Figures 70b and 70c. This gives further credence to the hypothesis of non-linear absorption by the V^0 defect. According to Table 2, it has a concentration of $\sim 16\%$ that of the NV^- concentration in diamond sample #1 and no measurable concentration in diamond sample #2. Figure 74 shows the behaviour at 723 nm was qualitatively the same as the behaviour at 820 and 950 nm for diamond sample #2. This may be further evidence that the behaviour shown in Figure 71a is, at least partially, related to the V^0 defect. The V^0 emission could be monitored in future experiments but may be difficult to differentiate from NV fluorescence as the emission spectra overlap.

It is also possible that substitutional nitrogen, which is ionised at wavelengths below ~ 765 nm [182], is responsible for absorption of the probe at 723 nm. Furthermore, a previous study has also shown that diamond containing substitutional nitrogen exhibits a variation in probe transmission as a function of temperature at wavelengths in the visible range [183]. This could reduce transmission at all wavelengths tested as a function of pump power. Future experiments should temperature stabilise the diamond

sample and could investigate the effect of temperature on the presented measurements. It is also possible that the probe is interacting with other defects in this wavelength range including the SiV⁻, GeV⁻ and L1 [184, 185].

Previous research has shown that, using HPHT diamond, it is possible to create samples with 16 ppm NV⁻ concentration with no observable NV⁰ concentration [61]. Future studies could also measure samples of this type for comparison. This would significantly increase the signal contribution from NV⁻ at the expense of an increased substitutional nitrogen content. If ionisation of substitutional nitrogen has played a role in the measurements, by using a low power probe at a wavelength above the ionisation energy of substitutional nitrogen (~765 nm [182]), interactions should be avoided. However, this would be at the expense of a relatively low stimulated emission cross section.

In comparison with a recently published experiment on stimulated emission from NV centres [22], the presented results do not compare well. The authors demonstrated a change in fluorescence on a timescale comparable to the lifetime of the NV⁻ excited state and with a wavelength dependency consistent with the stimulated emission cross section. Unlike their results, the wavelength dependencies and timescales demonstrated in the presented pump-probe measurements are not consistent with the excited state lifetime and stimulated emission cross section. Although it should be noted, time did not permit the effect on fluorescence to be measured in the presented experiments and should be checked in future.

The authors also reported a direct measurement of stimulated emission that showed approximately no dependence on probe power. However, there is not enough

information in the paper to determine whether this is an increase or decrease in probe power, only that there is a change in power. Depending on the phase settings of the lock-in amplifier, and whether or not magnitude mode was used, an increase in lock-in signal size could correspond to either an increase or decrease in probe power. The authors' measured dependence on probe power is difficult to compare with the presented results as the authors performed their measurements at a higher modulation rate, 548 Hz vs 3 Hz, the effect of which has not yet been investigated. They also performed measurements at a lower probe wavelength of 705 nm versus the lowest wavelength of 723 nm used in the presented experiments. The authors did not present a measurement of the dependence on pump power, the temporal dependence on the change in probe power or quantify the change in probe power, so these cannot be compared.

5.3.1.6 – Conclusion

A direct measurement of stimulated emission from an NV centre ensemble contained in a mm scale diamond was attempted using a pump-probe setup. Although stimulated emission may have occurred, it does not appear to be the predominant process interacting with the probe beam. Inconsistencies with a measurement of stimulated emission included the dependencies on time, wavelength and pump/probe power. Therefore, a conclusive measurement of stimulated emission from an NV centre ensemble was unsuccessful. Further investigation would be required to determine which processes are interacting with the probe and their relative contributions.

5.3.2 – Attempts to Measure Stimulated Emission under 637 nm Excitation

5.3.2.1 - Introduction

Because of the previous inconclusive measurements of stimulated emission using 532 nm excitation, a measurement of stimulated emission using a 637 nm pump was attempted.

Previous research has demonstrated photochromic behaviour in NV centres [186]. Further research has shown that to maintain high fluorescence rates requires excitation at a wavelength capable of exciting both NV^- and NV^0 charge states [57, 80], typically 532 nm. Excitation at 637 nm can cause rapid ionisation of NV^- [57, 126, 131]. Previous researchers have suggested that because 637 nm cannot excite the NV^0 , the re-combination process back to NV^- cannot take place [80, 187]. Research with single NV centres in nanodiamonds, at room temperature, has also shown that some NV centres can remain stable NV^- or NV^0 whereas others are more likely to undergo photochromic processes [78].

The hypothesis behind these experiments was that the NV^- population that remains under 637 nm excitation may be stable to photoionisation. If so, unlike the entire NV population which is excited at 532 nm, it may demonstrate behaviour typical of stimulated emission.

637 nm excitation is resonant with the ${}^3A_2 \rightarrow {}^3E$ transition and should remove phonon interactions in the excited state. With reference to Figure 60, the $|3\rangle$ state is removed, thus giving a 3-level system, neglecting the NV^- singlet states. Despite this, it is not a standard 3-level system [142] as stimulated emission is still expected to occur from a long-lived state $|2\rangle$ to a fast decaying state $|1\rangle$ at room temperature. It should, therefore, still enable efficient population inversion and stimulated emission.

Because no signal could be measured with diamond sample #1 or sample #2, sample #3 was used for these measurements. According to Table 2, sample #3 had an increased NV^- concentration of 0.76 ppm compared with the 0.549 and 0.313 ppm of sample #1 and #2 respectively.

5.3.2.2 - Experimental Setups

Figure 75 shows the setup used to measure the change of probe power as a function of time.

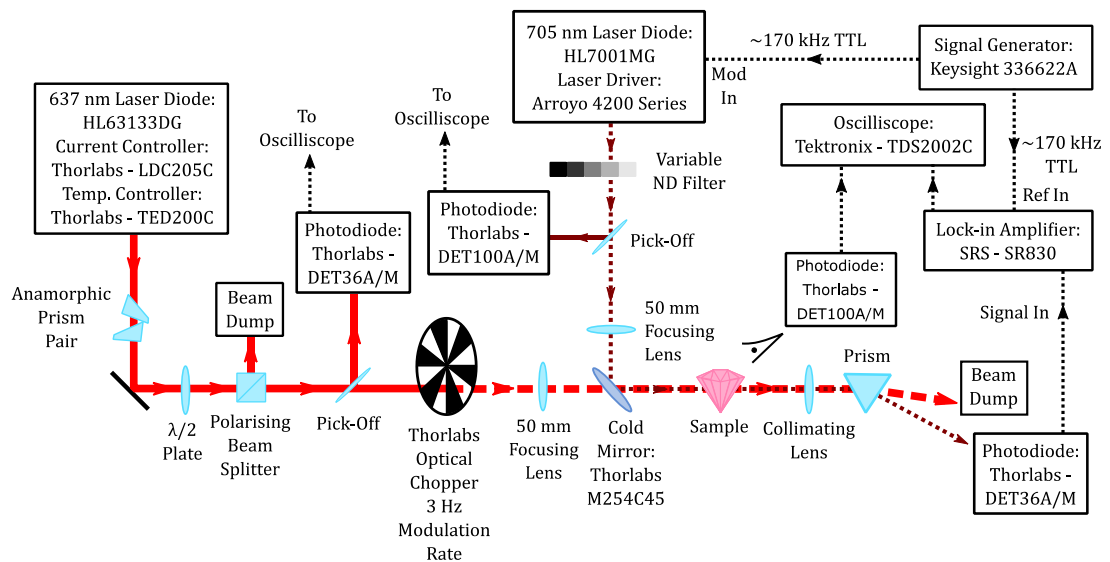


Figure 75 – Experimental setup for measurements of probe power as a function of time.

Modulated pump and probe beams are combined using a cold mirror, passed through the sample, and the probe measured with a photodiode after separation from the pump using a prism. Modulation of the pump is achieved using an optical chopper, and the probe using the laser diode driver. Demodulation of the probe is achieved using a lock-in amplifier referenced to the probe modulation rate and recorded with an oscilloscope.

Optical powers are monitored using beam pick-offs measured with photodiodes.

A 637 nm laser diode was used to generate the pump beam. This was chosen as it was an affordable (<£150) single mode laser diode at the wavelength of the NV- ${}^3A_2 \rightarrow {}^3E$ transition. The nominal maximum power of the diode was 170 mW which greatly reduced the expected pump and stimulated emission rates compared with the 532 nm pumped experiments where 3 W was available at the sample. Furthermore, based on a previous study [80], excitation under 637 nm is only a fraction as efficient as that at 532 nm at room temperature. The 637 nm laser diode was driven using a standard laser driver and temperature controller. An anamorphic prism pair was used to reduce the ellipticity of the beam. This was done to improve the overlap of the pump

and probe beams. The pump beam was modulated using a mechanical chopper, which easily provided enough bandwidth to enable the measurements.

Because the tunable laser used as the probe in Section 5.3.1 was no longer available, the probe beam was generated with another affordable laser diode (<£320). This was driven by a laser diode driver (Arroyo 4200 Series) capable of current modulation of the laser diode. Using a function generator, a voltage was applied to the 'mod in' input of the laser diode driver to modulate the power of the probe beam. This enabled fast modulation of the probe beam (~170 kHz) without the use of an AOM, as used in Section 5.3.1 and 5.3.3. Modulation was only to a depth of 10 % to prevent damage to the laser diode from being overdriven. Fast modulation was done to isolate the probe beam using a lock-in amplifier. Furthermore, it allowed the DC portion of the probe signal to be subtracted using the lock-in amplifier offset function. This is preferable to AC coupling to the oscilloscope as the bandwidth is not affected by using this function. This allowed the oscilloscope to be used to view the probe modulation, due to the pump interaction, at full resolution which is not possible for signals larger than 2 V.

Intensity control of the pump beam was achieved using a rotatable $\lambda/2$ plate and a polarising beam splitter. A variable neutral density filter was used to control the intensity of the probe beam. Pump and probe powers were monitored during experimentation using pick-offs measured with photodiodes. The pick-offs were calibrated to measurements of power at the sample using a calibrated optical power meter (Thorlabs PM100D and S130C). These were used to monitor the excitation powers during experimentation. Pump and probe beam diameters were 115 and 84 μm for the pump and probe respectively. These were measured using a Cinogy - CinCam CMOS beam profiler.

The pump and probe beams were combined using a UV fused silica substrate cold mirror (Thorlabs - M254C45), chosen for its low thermal expansion coefficient.

After initial alignment and measurement of the change in probe power as a function of time, the setup was changed to that shown in Figure 76.

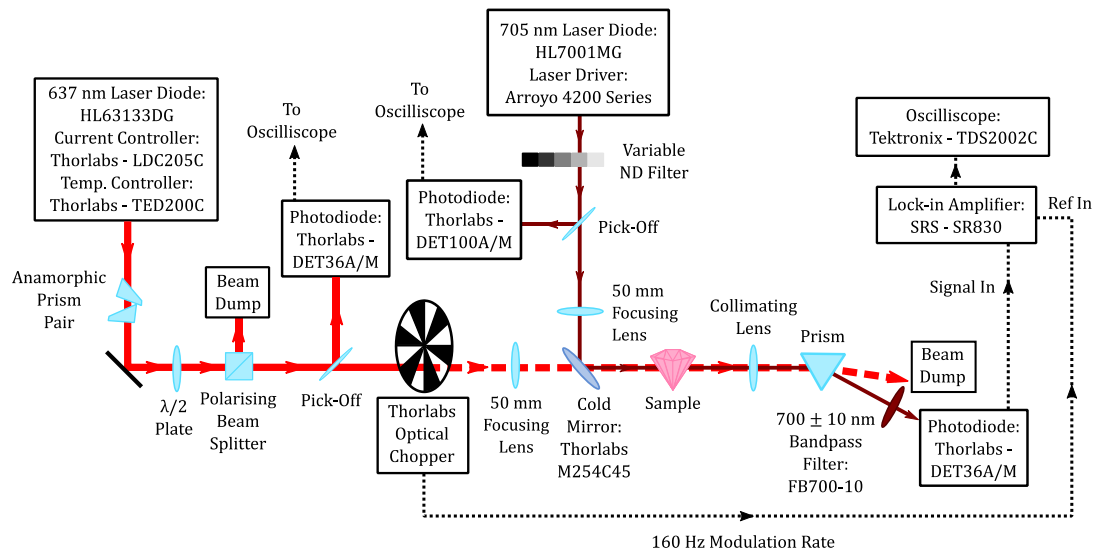


Figure 76 – Experimental setup for measurements as a function of pump and probe power. Modulated pump and CW probe beams are combined using a cold mirror, passed through the sample, and the probe measured with a photodiode after separation from the pump using a prism. Modulation of the pump is achieved using an optical chopper. Probe signal amplitude at the pump modulation rate is measured using a lock-in amplifier and recorded with an oscilloscope. Optical powers are monitored using beam pick-offs measured with photodiodes.

The experimental design was changed to allow measurement of the entire probe power interacting at the sample, rather than only the 10 % AC portion of the probe. To ensure no pump light hit the detector, a bandpass filter was added to the photodiode. By checking the output of the lock-in amplifier was zero when either the pump or the

probe was blocked, a measurement of only the probe modulation due to the pump interaction was ensured.

To increase the signal-to-noise ratio of the measurement, the pump modulation rate was increased to 160 Hz. Unfortunately, because the bandwidth of the photodiode was not checked, it cannot be guaranteed that the full modulation amplitude was detected by the lock-in amplifier. If the photodiode bandwidth was exceeded, the lock-in amplifier should output the same trends with a reduced amplitude. For that reason, the results have been normalised.

5.3.2.3 – Results

Figure 77 shows the dependency of the change in probe power as a function of pump power. Error bars in the following measurements correspond to the resolution and DC uncertainty of the oscilloscope and the peak to peak drift/absolute deviation of the output of the lock-in amplifier. This was measured by filling the oscilloscope screen with the output of the lock-in amplifier and measuring the peak to peak deviation.

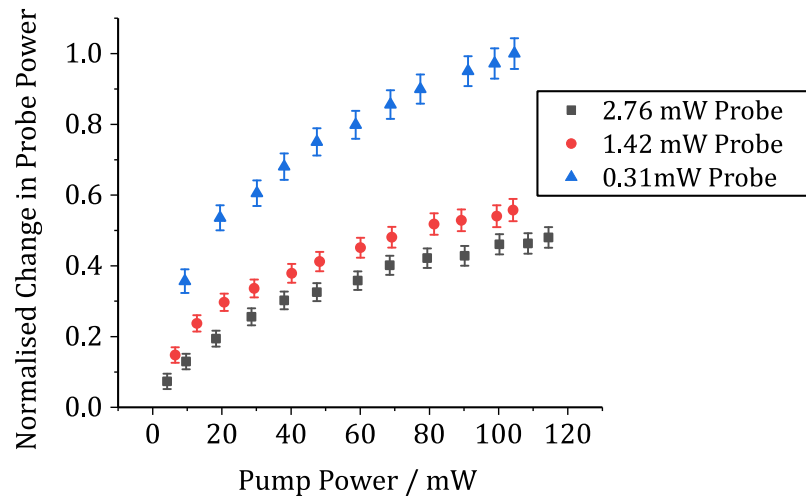


Figure 77 – Change in probe power as a function of pump power.

Figure 77 shows the dependencies are non-linear and reduce with increasing probe power. This is not in agreement with the previous titanium:sapphire results shown in Figures 66 and 67 and suggests stimulated emission is not the process being measured. However, they are qualitatively similar to those in Figure 72, suggesting similar processes are being driven under both 637 and 532 nm pump wavelengths.

The dependence on probe power is shown in Figure 78.

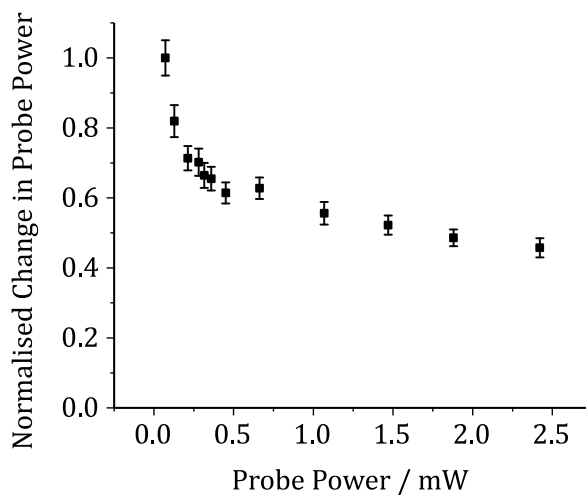


Figure 78 – Change in probe power as a function of probe power with pump power at 120 mW.

Figure 78 also shows a non-linear dependence on probe power and suggests non-linear absorption of the probe.

Figure 79 shows the modulation of the probe beam is in phase with the pump beam and demonstrates there is a relative increase in probe power when the pump is on.

Furthermore, the temporal dynamics are qualitatively similar to those in Figure 74 suggesting similar processes are being driven under both 637 and 532 nm pump wavelengths.

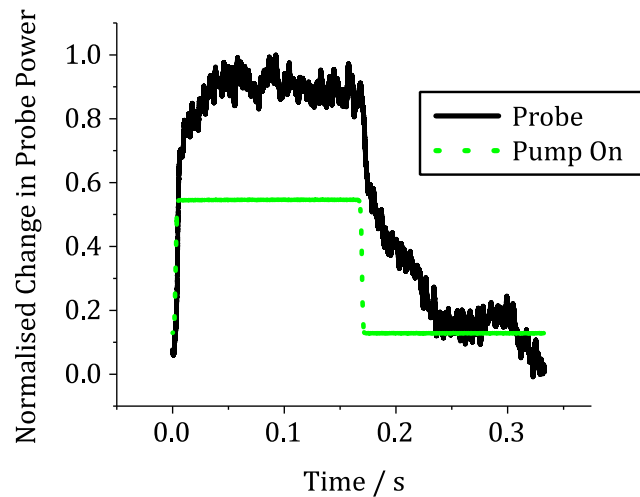


Figure 79 – Change in probe power as a function of time at 120 mW pump and 0.31 mW probe power (512 averaged).

5.3.2.3 - Discussion

Given the behaviour using a 637 nm pump is qualitatively similar to that measured using a 532 nm pump, the hypothesis that the probe would interact with a remaining, stable NV^- population and exhibit characteristics of stimulated emission has been disproven

It is not currently clear if the NV^0 to NV^- recombination process has been inhibited under 637 nm excitation. A previous measurement on a single NV centre has shown that 637 nm excitation only completely inhibited fluorescence at low temperature (10 K) [80]. At room temperature, several studies on single NV centres have shown that the probability of NV^- fluorescence under 637 nm excitation is below 10 % of that under 532 nm excitation [57, 80, 156]. The fact there is fluorescence at all suggests there is still a recombination process happening at room temperature. This may be due to

excitation of the NV^0 via the phonon sideband which would be more likely at higher temperatures [81]. Spectroscopy of the fluorescence under 637 nm excitation should be performed in future experiments to confirm if NV^0 is being excited.

The recombination process could also be related to tunnelling [124, 128]. Therefore, future experiments should measure the NV^- fluorescence rate as a function of time between 637 nm pump pulses. This should be repeated with and without the 705 nm probe to ascertain its effect on the recombination process. The results obtained could be compared with those under 532 nm pump. Under the same pump power, photoionisation rates should be higher under 637 nm pump which should result in a larger change in fluorescence rates between pulses.

Future experiments should also measure the change in probe power under 532 nm and 637 nm pump using the same probe. If the change in probe power was found to be larger under 637 nm pump than under 532 nm pump, at the same pump power, this would provide good indirect evidence that photoionisation processes are responsible for the change in probe power.

5.3.2.4 – Conclusion

A conclusive measurement of stimulated emission from a nitrogen-vacancy centre ensemble under resonant 637 nm excitation has been unsuccessful. Although a relative increase in probe power was detected using a pump-probe setup, inconsistencies with a measurement of stimulated emission included the temporal and power dependencies on the change in probe power. Further investigation would be required to determine with which processes the probe beam is interacting and their relative contributions.

5.3.3 - Attempts to Measure ODMR using Stimulated Emission

5.3.3.1 – Introduction

Despite the presented inconclusive measurements of stimulated emission, ODMR was attempted with a probe beam. The experimental setup used to measure relative changes in probe power under 532 nm excitation was modified to allow the following measurements without having to re-align the pump and probe beams. The primary aim was to demonstrate the first read-out of ODMR using stimulated emission from an NV⁻ ensemble. This is a required process for a proposed laser-based magnetometer using NV⁻ [23]. A second aim was to demonstrate a wavelength dependency that would provide further indirect evidence of stimulated emission from an NV⁻ ensemble.

5.3.3.2 – Theory

As discussed in Section 2.2.6, optical detection of magnetic resonance (ODMR) is possible due to spin-state dependent intersystem crossing rates from the ³E state to the NV⁻ singlet states. Because NV centres in the singlet states cannot undergo stimulated emission from the ³E state, the stimulated emission rate, like the fluorescence rate, is expected to be spin-state dependent. Equation 32 shows the stimulated emission cross-section is proportional to the fraction of pumped NV⁻ in the |2> state (f_2). This would be maximised for NV⁻ in the $m_s=0$ state and reduced for NV⁻ in the $m_s= \pm 1$ states (due to occupation of the singlet states). Optical spin polarisation into the $m_s=0$ state will,

therefore, maximise the stimulated emission rate. If the $m_s=0 \rightarrow m_s=\pm 1$ transition is excited, a corresponding reduction in the stimulated emission rate should occur until spin re-polarisation. This reduction in the stimulated emission rate serves as the read-out method of ODMR.

A simplified setup to measure ODMR using modulated stimulated emission is shown in Figure 80.

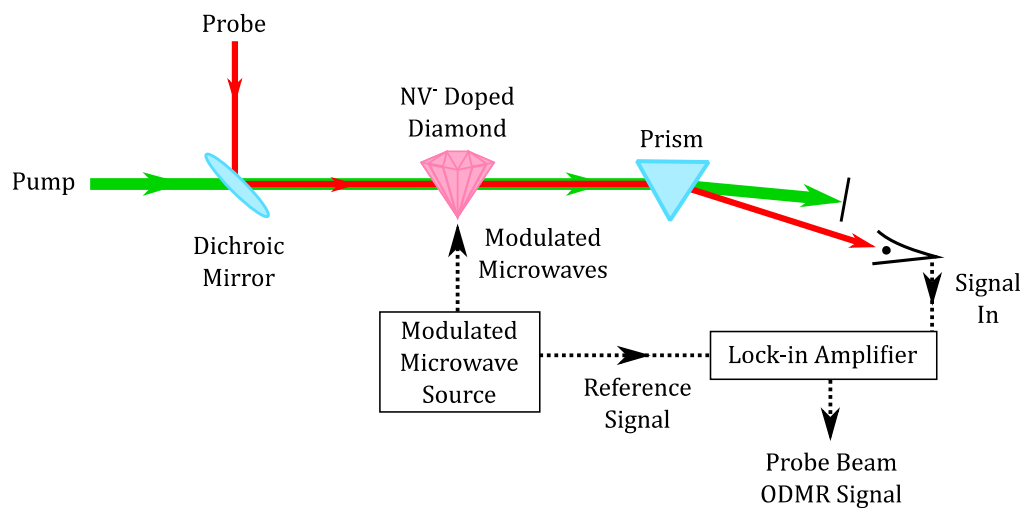


Figure 80 – Simplified experimental setup to measure probe beam ODMR. Pump and probe beams are combined with a dichroic mirror and passed through an NV centre doped diamond sample. Modulated microwaves are applied to the sample and their frequency swept. The pump and probes are separated using a prism and the probe measured with a photodiode connected to a lock-in amplifier. This is referenced to the modulation rate of the microwaves to enable extraction of the ODMR signal.

The pump and probe beam are overlapped using a dichroic mirror and passed through the diamond sample. Optical amplification of the probe beam should occur. Because the

stimulated emission rate is proportional to the spin state of the NV⁻; application of modulated microwaves resonant with the $m_s=0 \rightarrow m_s=\pm 1$ transition will cause modulation of the optical amplification. The microwave frequency is swept across that of the ODMR resonance. The probe is separated from the pump using a prism and the probe power measured as a function of time. By de-modulating the probe signal at the microwave modulation frequency, the ODMR signal should be extracted. The output of the lock-in amplifier is expected to match that described in Section 3.3.3. However, a reduction in probe beam ODMR contrast (C_p), compared with ODMR contrast measured via fluorescence (C), is expected.

In a fluorescence ODMR experiment, 100 % of the fluorescence signal contributes to the ODMR contrast. However, in a single pass optical amplification setup, this is not the case. Only the stimulated emission can contribute to the ODMR contrast, not the entire probe power. If P is the probe power after the diamond in the absence of a pump, and ΔP is the change in probe power due to stimulated emission, it is proposed that C_p will be reduced as such:

$$C_p = C \frac{\Delta P}{P + \Delta P} \quad (40)$$

Based on this model, a graph of ΔP vs. C_p/C is shown in Figure 81.

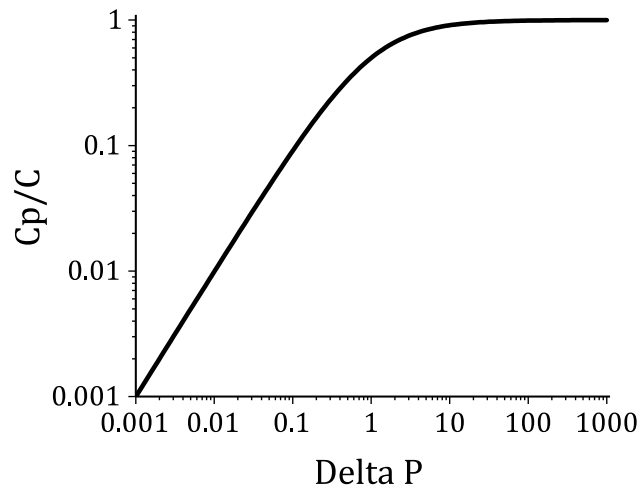


Figure 81 – Plot of ΔP vs. C_p/C based on the proposed model (Equation 40).

Figure 81 shows a relative gain of 100 % is required to achieve a probe beam ODMR contrast that is 50 % that of the fluorescence ODMR contrast. For optical gains $\ll 1$, probe beam ODMR contrast is relatively low.

Because ΔP is proportional to the stimulated emission cross section, assuming Equation 40 is correct, the probe beam ODMR contrast should also match the wavelength dependency of the stimulated emission cross section. This assumes that stimulated emission is the only process responsible for ODMR contrast in the measurement.

5.3.3.3 - Experimental Setup

The experimental setup used to measure ODMR with a probe beam is shown in Figure 82.

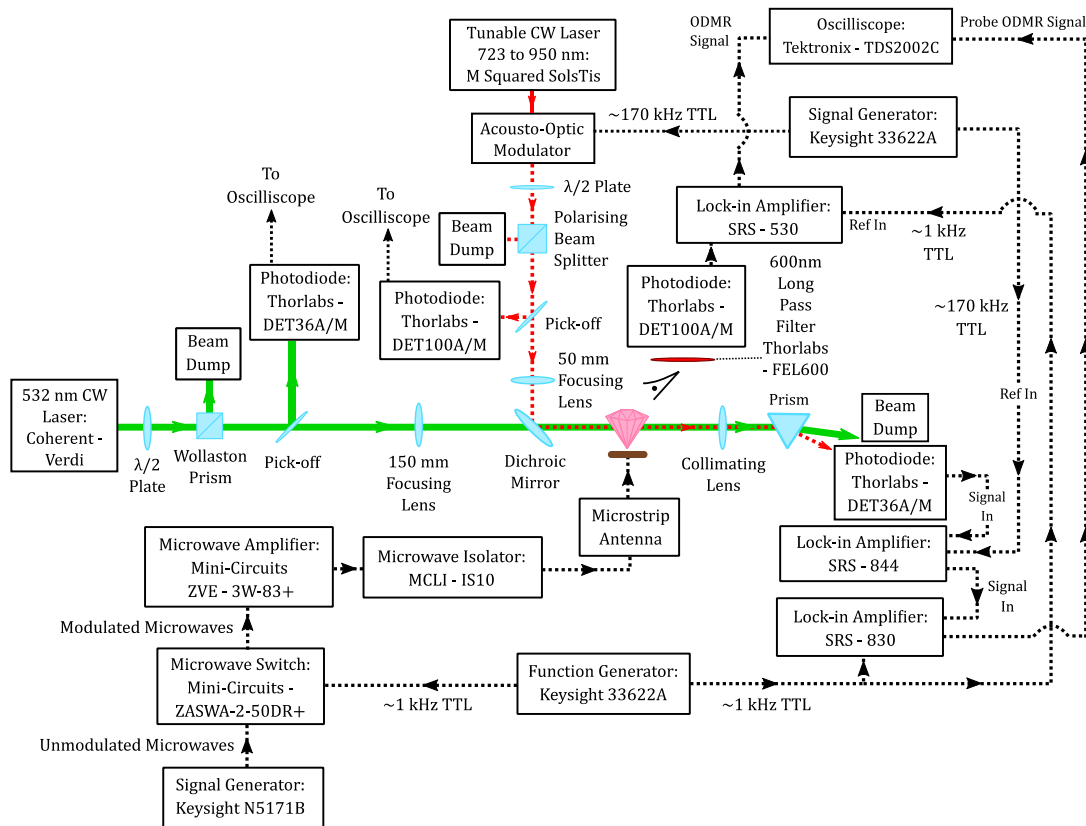


Figure 82 – Experimental setup used to measure probe beam ODMR. Pump and probe beams are combined with a dichroic mirror and passed through an NV centre doped diamond sample. Modulation of the probe is achieved with an AOM. Frequency swept microwaves are modulated using a microwave switch and applied to the sample after amplification. The pump and probes are separated using a prism and the probe measured with a photodiode connected to a lock-in amplifier referenced to the probe modulation rate. The demodulated signal is fed into a second lock-in amplifier referenced to the microwave modulation rate to extract the ODMR signal. This is recorded with an oscilloscope.

To mitigate against mistakenly measuring ODMR via fluorescence, rather than modulation of the probe beam, both the microwaves and probe beams were modulated. This enabled a lock-in amplifier to isolate the probe signal from any fluorescence or pump light that may have reached the detector. This was possible by modulating the

probe at a high frequency (~ 170 kHz) relative to the microwave modulation rate of ~ 1 kHz. Fast modulation of the probe beam was achieved using an acousto-optic modulator and slow modulation of the microwaves was performed using a microwave switch (Mini-Circuits - ZASWA-2-50DR). Both were square-wave modulated with a 50% duty cycle, 100% modulation depth and referenced to a two-channel arbitrary function generator (Keysight - 33622A). Due to very low ODMR contrast, there was a low signal-to-noise ratio for the probe beam ODMR measurements. To enable measurement despite this, no integration was performed on the high-frequency lock-in amplifier (SRS-844) and an integration time-constant of 3 or 10 s was used on the low-frequency lock-in amplifier (SRS-830), depending on the signal-to-noise ratio. Lower integration time constants are preferable as they increase the bandwidth but are at the expense of a decreased signal-to-noise ratio. By slowly sweeping the microwave frequency (sweep time ~ 25 mins), the lock-in amplifier had sufficient bandwidth to measure the ODMR spectra. For comparison with probe beam ODMR measurements, ODMR via fluorescence was measured simultaneously with a photodetector (DET100A/M) and an additional lock-in amplifier (SRS-530) referenced to the microwave modulation rate. The same time constant was used for both lock-in amplifiers that were referenced to the microwave modulation rate.

Measurements of ODMR contrast as a function of pump power were initially performed with a relatively low probe power (5 mW) as probe ODMR contrast was found to reduce with probe power. After finding the optimum pump power, measurements of probe ODMR contrast as a function of probe power and ODMR spectra were performed at the optimum pump powers. In measurements of ODMR contrast as a function of pump and probe power, probe ODMR amplitudes were maximised for each data point by tuning the microwave frequency until the ODMR amplitude maxima were found.

This was to mitigate against thermal shifts of the ODMR resonance. A variable neutral density filter was placed in front of the photodetector and was adjusted to ensure the same power hit the photodetector throughout measurements of probe ODMR contrast as a function of probe power.

To measure the percentage change in probe power, the DC output of the fast lock-in amplifier was measured with an oscilloscope. This corresponded to the probe power (P_{probe}). The output of the fast lock-in amplifier was connected to the input of the slow lock-in amplifier and the output recorded. An arbitrary function generator (Keysight – 33622A) was then used to input a square wave at the slow modulation frequency into the second lock-in amplifier. The peak-to-peak input voltage required for the second lock-in amplifier to output the voltages measured during experimentation corresponded to the change in probe power (ΔP_{probe}).

5.3.3.4 – Results

To verify the experimental setup measured ODMR via the probe beam and not via fluorescence, the ODMR amplitude via fluorescence and probe beam were alternatively measured using the same photodetector at increasing distances from the diamond sample. This is shown in Figure 83 and was possible as, using a lock-in amplifier, measurements of ODMR are possible with only nV-scale signal modulations. Error-bars for the accuracy of the distances are estimated at ± 0.5 cm. Error bars for the ODMR amplitudes correspond to the peak to peak drift/absolute deviation of the output of the final lock-in amplifier and the resolution and DC uncertainty of the oscilloscope.

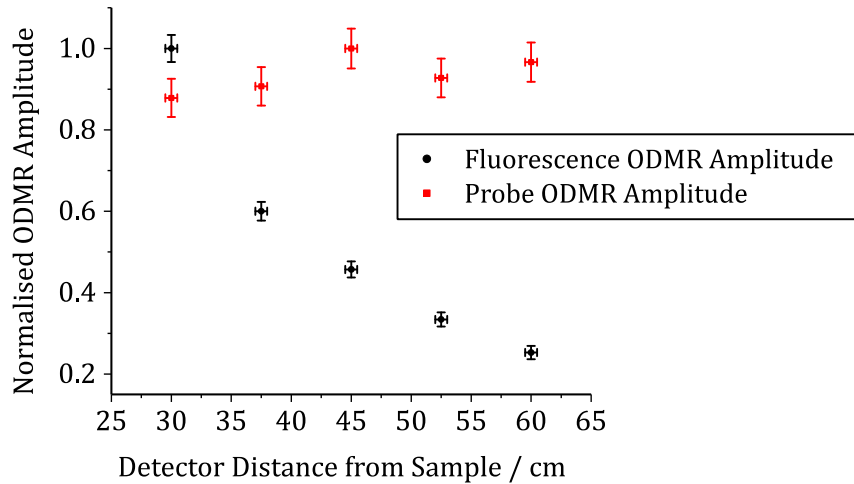


Figure 83 - ODMR amplitude as a function of distance from the sample. 1.75 W of pump power was used and ~1 mW of probe power. Measurements were made with diamond sample #2.

Figure 83 shows the detected fluorescence ODMR amplitude reduced as the distance from the sample was increased. This should be expected as increasing the distance from the sample decreases the signal intensity on the detector. The probe beam amplitude remained constant as the probe beam is collimated and the same power hits the detector throughout the measurements. This conclusively demonstrates the ODMR contrast was contained in the probe beam.

For comparison with measurements of probe beam ODMR contrast, measurements of ODMR contrast via fluorescence, as a function of pump and probe power, were measured. This is shown in Figure 84. Measurements of ODMR contrast via fluorescence were made by measuring the fluorescence intensity with and without microwaves applied. Error bars in Figure 84 correspond to the resolution and DC uncertainty of the oscilloscope.

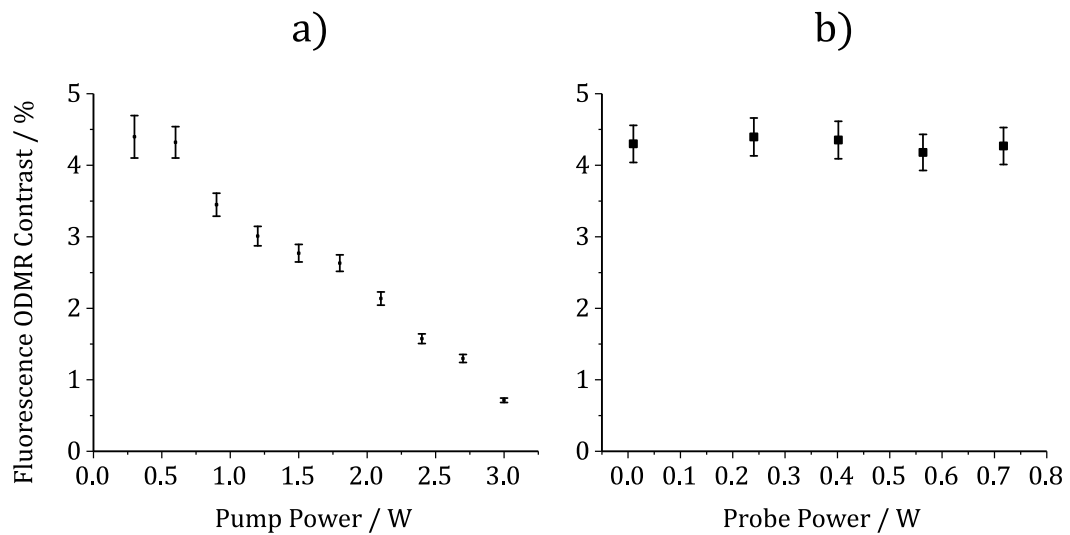


Figure 84 – ODMR contrast as a function of a) pump power and b) probe power at 723 nm (0.5 W of pump power was used). Measurements were made with diamond sample #2.

Figure 84a shows the ODMR contrast reduced as a function of pump power, which, like in Chapter 4 and discussed in Section 4.5, is thought to be due to heating of the microwave antenna on which the diamond sat. Figure 84b shows the probe has no effect on the ODMR contrast measured via fluorescence within the uncertainty of the measurement and over the range tested. There is no known reason why the probe beam would affect the ODMR contrast measured by fluorescence, therefore, this is the expected result.

5.3.3.4.1 - Diamond Sample #1

Measurements of the dependency of probe beam ODMR contrast on pump and probe power, using diamond #1, are shown in Figure 85. Error bars in these measurements correspond to the peak to peak drift/absolute deviation of the output of the final lock-in amplifier and the resolution and DC uncertainty of the oscilloscope.

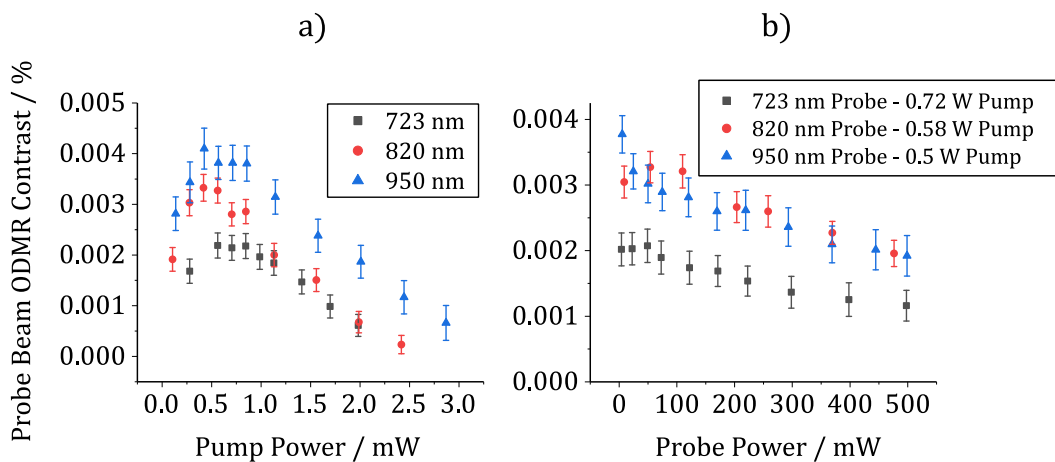


Figure 85 – Probe beam ODMR contrast as a function of a) pump power (probes at 5 mW) and b) probe power (pump at 0.5 W).

Figure 85a shows the probe beam ODMR contrast initially increases with pump power until a maximum is reached, after which, the contrast decreases.

Figure 85b shows probe beam ODMR contrast decreases with increasing probe power. At 723 and 820 nm, there is less of a non-linear trend than at 950 nm. This may indicate there are different processes taking place at the different wavelengths.

Probe beam ODMR spectra, obtained at each wavelength, are shown in Figure 86.

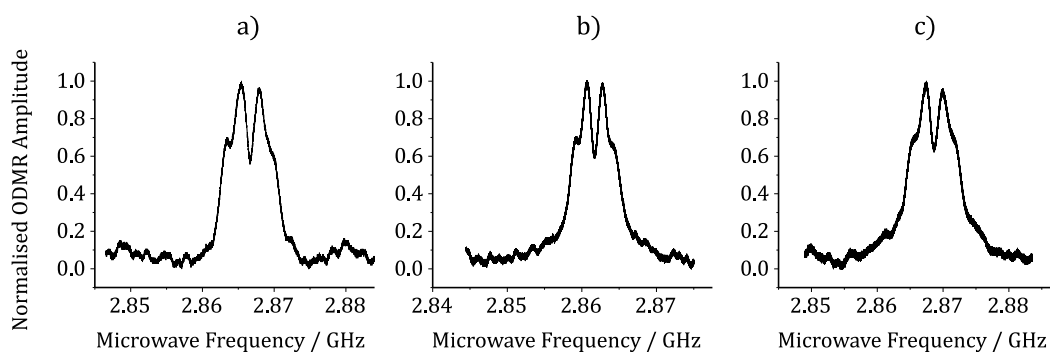


Figure 86 – Probe beam ODMR Spectra with probe at a) 723 nm (1 mW probe and 0.72 W pump), b) 820 nm (5 mW probe and 0.58 W pump) and c) 950 nm (1 mW probe and 0.5W pump).

This demonstrates the ability to perform magnetometry using a probe beam at 723, 820 or 950 nm using diamond sample #1. To verify the spectra are as expected, the ODMR spectra were simultaneously measured via fluorescence, as shown in Figure 87.

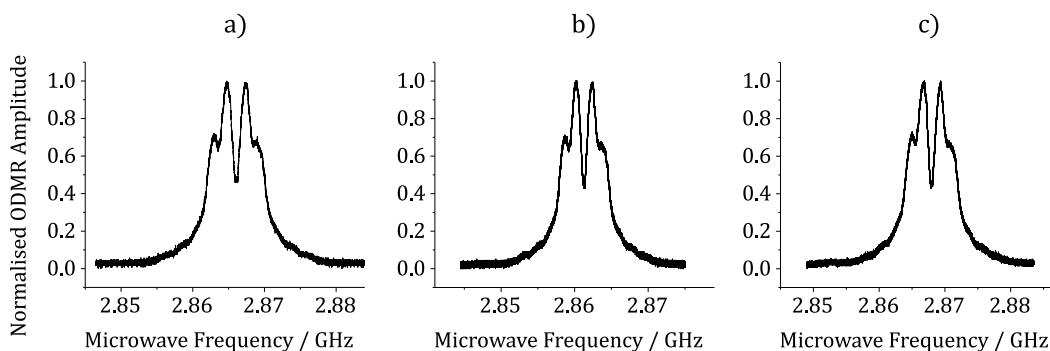


Figure 87 – Fluorescence ODMR Spectra - a), b) and c) correspond to those measured simultaneously with a), b) and c) from Figure 86.

Apart from the obvious increase in signal-to-noise ratio in the spectra shown in Figure 87 compared with Figure 86, it is clear the same spectra are being measured. The increase in signal-to-noise is due to the increased contrast for ODMR via fluorescence,

as shown in Figures 84 compared with 85. For the probe beam measurements, there is also an increased intensity noise from using a probe beam. The probe beam measurement has intensity noise contributions from both the pump and probe beams, whereas the fluorescence measurement has only a contribution from the pump beam.

5.3.3.4.2 - Diamond Sample #2

Measurements of the dependence of probe beam ODMR contrast on pump and probe power, using diamond #2, are shown in Figure 88. Error bars in these measurements correspond to the peak to peak drift/absolute deviation of the output of the final lock-in amplifier and the resolution and DC uncertainty of the oscilloscope.

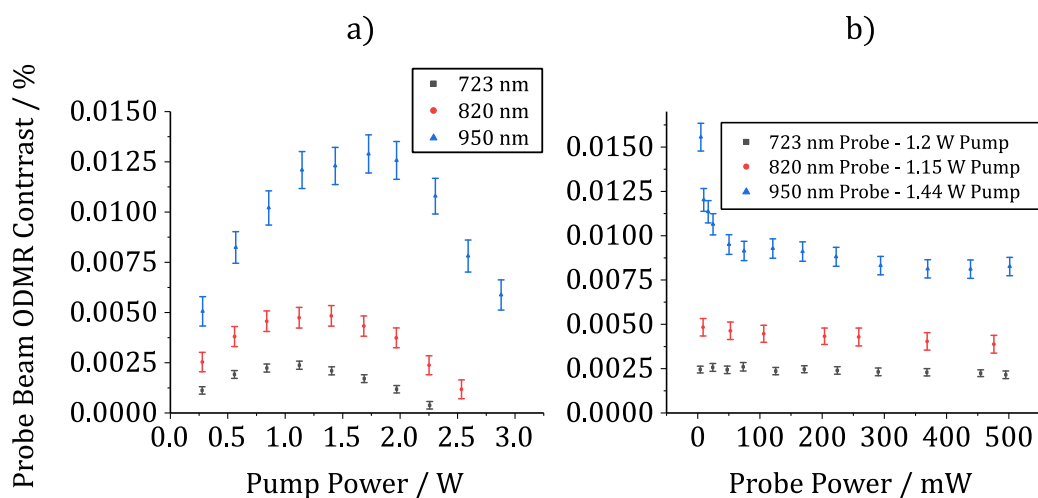


Figure 88 – Probe beam ODMR contrast as a function of a) pump power (probes at 5 mW) and b) probe power.

Compared with Figure 85a, the pump power dependencies shown in Figure 88a are qualitatively very similar. Again, there is an initial increase in ODMR contrast with pump power until a maximum is reached, after which, the contrast drops.

Figure 88b shows a clear difference in the probe power dependencies between 950 nm and 723/820 nm. The probe power dependence at 950 nm is clearly non-linear whereas at 723 nm and 820 nm, there is no dependence, within the uncertainty of the measurement. This may indicate that absorption by the singlet states is responsible for the ODMR contrast at 950 nm whereas at 723 and 820 nm, the ODMR contrast may come from stimulated emission.

Probe beam ODMR spectra, obtained at each wavelength, are shown in Figure 89.

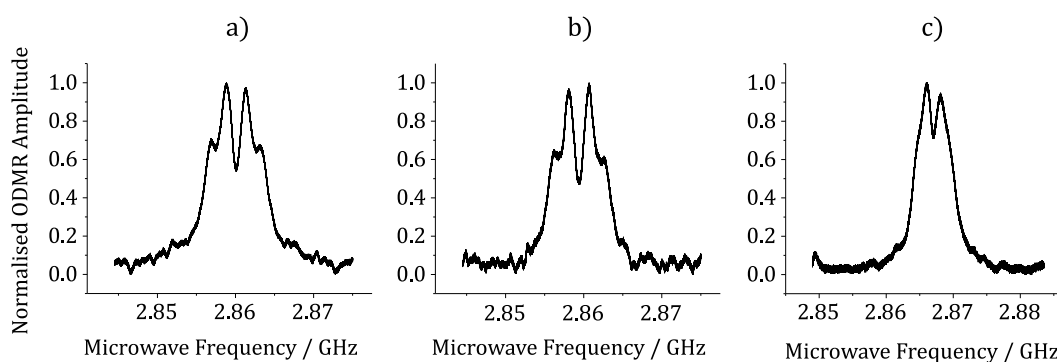


Figure 89 - Probe beam ODMR spectra with probe at a) 723 nm (3 mW probe and 1.2 W pump), b) 820 nm (3 mW probe and 1.15 W pump) and c) 950 nm (5 mW and 1.44 W pump).

This demonstrates the ability to perform magnetometry using a probe beam at 723, 820 or 950 nm using diamond sample #2. The expected output was also verified by measuring ODMR spectra simultaneously via fluorescence, as shown in Figure 90.

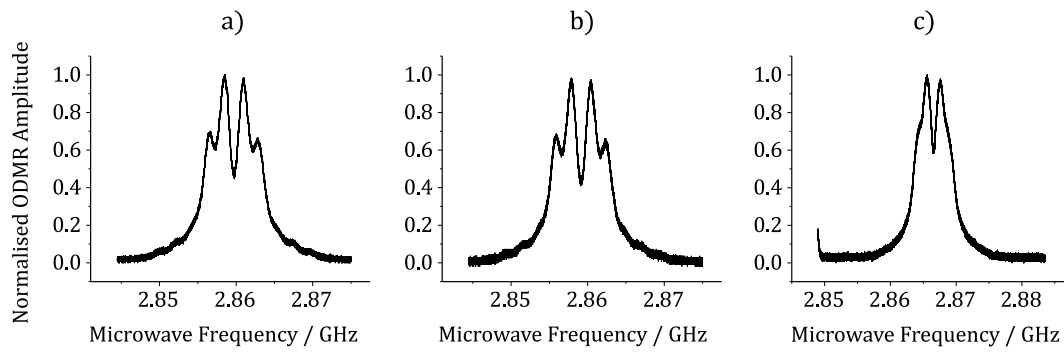


Figure 90 – Fluorescence ODMR spectra – a), b) and c) correspond to those measured simultaneously with a), b) and c) from Figure 89.

Again, Figure 90 clearly shows agreement between the spectra measured in Figure 89 and an increased signal-to-noise ratio when measuring ODMR using fluorescence.

5.3.3.5 – Discussion

Assuming the probe beam ODMR contrast is proportional to the stimulated emission cross section, based on the NV^- emission spectrum [22, 57], the stimulated emission cross section was expected to be relatively high at 723 nm, low at 820 nm and near zero at 950 nm. The presented wavelength dependencies demonstrated in Figures 85 and 79 do not suggest stimulated emission is responsible for the measured probe beam ODMR contrast. However, this is consistent with absorption of the NV^- singlet state transition which has a zero-phonon line at 1042 nm. This transition has previously been shown to absorb to at least 800 nm at 10 K [177] and has been used to perform ODMR [50, 113].

Figures 85a and 88a show qualitatively similar pump dependencies on probe beam ODMR contrast for both diamond samples. An increase in ODMR contrast with pump power is expected for measurements using stimulated emission as the occupancy of the 3E state should increase with pump power, assuming the system is below saturation. However, this would also be true of absorption of the NV^- singlet states [113], as the occupancy of these states should also increase. Thus, these results cannot be considered evidence for stimulated emission.

It is suggested that the reduction in probe beam ODMR contrast at higher pump powers is due to the same reason the ODMR contrast, measured via fluorescence, dropped at higher pump powers, as shown in Figure 84a. This is suspected to be due to heating of the microwave antenna causing a reduction in microwave coupling efficiency. Further investigation would be required to confirm this hypothesis. To mitigate heating of the antenna, future experiments should temperature stabilise the diamond or use an antenna design that is not in contact with the diamond, for example, a loop antenna.

Figure 84b demonstrates the fluorescence ODMR contrast is not affected by the probe beam power. In comparison, Figures 85b and 88b show, at 950 nm, the probe beam ODMR contrast clearly depends on probe power. This suggests the probe is being absorbed at this wavelength, likely by the singlet state transition. However, at 723 nm and 820 nm, there is less of a dependence. In diamond sample #2 there is no dependence, within the uncertainty of the measurements, at these wavelengths. This may be evidence that stimulated emission is responsible for the ODMR contrast at these wavelengths.

All probe power dependencies for diamond sample #1 showed a downward trend. This may indicate an additional absorbance process taking place in this diamond. This could be related to the NV^0 which, unlike sample #2, has an almost equal concentration to that of the NV^- . This may be a recently demonstrated process that used 1064 nm excitation to convert NV^0 to NV^- [155]. As this process was spin-state dependent, it allowed ODMR via measurement of NV^0 fluorescence [155]. Without knowledge of the wavelength range over which this process can be excited, it is not possible to rule it out as being, at least partially, responsible for the observed ODMR contrast.

In future studies, it would be interesting to make the same measurements at additional wavelengths between the peak of the $^3A_2 \rightarrow ^3E$ phonon sideband, near 700 nm, and the zero-phonon line of the $^1E \rightarrow ^1A_1$ transition at 1042 nm. If a clear trend from no dependence to a non-linear dependence on probe power could be demonstrated as a function of wavelength, this would be good indirect evidence that stimulated emission is responsible for the ODMR contrast at the lower wavelengths and absorption of the singlet states is responsible at the higher wavelengths.

Another possible mechanism for the observed ODMR contrast is temperature variations in the diamond causing a change in the transmission properties [183]. Because less pump is absorbed when the $m_s=0 \rightarrow m_s=\pm 1$ transitions are excited, the diamond should be relatively cooler when the microwaves are applied. If this is the mechanism, temperature stabilisation of the diamond should decrease the ODMR contrast. This could be checked in future experiments.

It should also be noted that a measurement of the probe beam ODMR modulation was unable to be made directly, i.e. without use of a lock-in amplifier. Therefore, the change

in probe power upon application of microwaves could be positive or negative. Although attempts were made to make this measurement, there was insufficient signal-to-noise to make conclusive judgements. The relative phase should be checked in future measurements by de-modulating the fluorescence and probe beam ODMR signals using the same lock-in amplifier and checking the relative sign of the output. If the probe beam ODMR was demonstrated to modulate out of phase with the fluorescence ODMR spectrum, both modulation of stimulated emission and absorption of the singlet states could be ruled out as the mechanism for the observed probe beam ODMR contrast. Applying microwaves resonant with the $m_s=0 \rightarrow m_s=\pm 1$ transition should cause an increased population of the NV⁻ singlet states. This should increase probe beam absorption and decrease both fluorescence and stimulated emission rates. These all correspond to drops in measured power.

Because the gain due to stimulated emission could not be measured, the proposed model for a reduction in ODMR contrast via stimulated emission, shown in Figure 81, could not be tested.

5.3.3.6 – Conclusion

ODMR using a probe beam was successfully measured from nitrogen-vacancy centre ensembles contained in mm scale diamonds at 723, 820 and 950 nm.

In diamond sample #2, no probe power dependency on ODMR contrast was measured at 723 and 820 nm. This is consistent with stimulated emission being responsible for the ODMR contrast. At 950 nm the probe power dependency was non-linear, which

suggests absorption by the singlet states. Similar results were obtained using diamond sample #1 except for an additional negative dependency of probe power on probe beam ODMR contrast.

Because of the wavelength dependencies of the probe beam ODMR contrast shown in Figures 85 and 88, absorption of the NV⁻ singlet states could not be ruled out as the mechanism of ODMR at 723 and 820 nm. In particular, a greater ODMR contrast was expected at 723 nm than at 820 nm. This was not observed. The dependencies on pump power were consistent with either stimulated emission or absorption of the singlet states. Therefore, a conclusive demonstration of ODMR via modulated stimulated emission was unsuccessful.

5.4 - Conclusion

The primary aim of this chapter was to quantify the optical gain of a probe beam due to stimulated emission from a nitrogen-vacancy centre ensemble. Despite building a setup that could arguably measure relative optical gain using a titanium:sapphire sample, the results with diamond were not fully consistent with a measurement of stimulated emission. Regardless of whether the diamond samples were pumped resonantly (637 nm) or on the phonon sideband (532 nm), the power and time dependencies of the changes in probe power were inconsistent with stimulated emission.

Despite this, ODMR was demonstrated using a probe beam at a wavelength of 723 nm where stimulated emission was expected, and absorption of the singlet states was not. Furthermore, no dependence of probe power on probe beam ODMR contrast at 723 nm

was observed in diamond sample #2. This is also consistent with stimulated emission. However, because the wavelength dependency of the ODMR contrast did not match the expected wavelength dependency of the stimulated emission cross-section, the mechanism for ODMR readout could not be attributed to stimulated emission.

Further investigation would be required to ascertain with which processes the probe beam was interacting, and their relative contributions, in the presented experiments. These may include NV photo-conversion processes, interactions with the NV⁻ singlet state and interactions with other defects in diamond.

Chapter 6

Conclusion

Studies were performed to progress the application of nitrogen-vacancy centres to the sensing of magnetic fields using the optical detection of magnetic resonance (ODMR).

Chapter 3 described the building of a fluorescence-based optical microscopy system capable of magnetometry via the ODMR of nitrogen-vacancy centre ensembles in microdiamond. The system was designed to perform measurements of bio-magnetism with the goal of measuring the action potentials of a dissected marine worm.

As described in Section 2.2.5.1, it was realised that only ensembles of NV centres contained within a single crystal would allow sensitive quantitative measurements of action potentials using CW-ESR. Thus, a single ~ 150 μm diameter diamond was used to increase the fluorescence yield and to give an upper limit on the expected sensitivity for single (ensemble) nanodiamond measurements. The system was capable of making room temperature, point measurements of magnetic fields with a sensitivity of 70 ± 26 $\text{nT}/\text{Hz}^{1/2}$, with a bandwidth of 3.1 kHz, using 2 mW of optical excitation.

Scanning DC magnetometers with single NV centres can achieve sensitivities of ~ 2 $\mu\text{T}/\text{Hz}^{1/2}$ for point measurements [98]. This is considerably less sensitive than the presented magnetometer. This demonstrates the clear advantage of using ensembles of NV centres for sensing. However, as discussed in Section 2.2.7, state-of-the-art, point

measurement, ensemble NV magnetometers typically achieve sensitivities of ≤ 50 pT/Hz^{1/2} [16, 110, 114]. This can be achieved at room temperature using both absorption-based probe [114] and fluorescence-based [16] sensors, even when performing vector magnetometry [110]. The key difference in these setups is the ability to use high optical excitation powers (up to several watts). This allows as much as 52 mW of fluorescence to be collected [110] and, in probe measurements, 4.2 mW of probe power can be collected with less than 500 mW of pump power used [114]. These exceed even the excitation power of 2 mW used in the presented magnetometry experiments. Thus, the huge decrease in optical power used in the presented magnetometer greatly increases the shot noise limit and achievable sensitivity compared with the state-of-the-art.

The sensitivity achieved in the presented magnetometer fell below the target sensitivity of 380 pT/Hz^{1/2} which, based on a previous study (84), should allow measurement of the action potential of a marine worm with a signal-to-noise ratio of 1, using 1 second of averaging. Without significant gains in the magnetic resonance linewidth / inhomogeneous spin dephasing time (T_2^*), the long-term goal of quantitative measurements of action potentials is not feasible using this experimental method. For that reason, it is recommended that future experiments focus on experimental techniques such as relaxometry [144, 145] or the electric-field detection of membrane potentials [7].

Chapter 4 described experiments that proved the viability of two-photon excited magnetometry using NV centres. To the best of the author's knowledge, it is the first demonstration of two-photon excited optical detection of magnetic resonance using nitrogen-vacancy centres. Should a method of action potential detection be established

in future, this work proves that it should also be possible to use two-photon microscopy to make such measurements. Advantages of using two-photon microscopy for live cell imaging include increased imaging depth and reduced phototoxicity when performing 3D imaging [18]

The experiment in Section 4.4.3 showed a reduction in ODMR linewidth using two-photon excitation compared with one-photon excitation at the same fluorescence rate. This suggests that 2-photon excitation may be superior to one photon excitation for applications in magnetometry. However, it was also found that the two-photon excited fluorescence rate saturated at rates at least two orders of magnitude less than that using one-photon excitation. This is likely related to recently demonstrated processes whereby one-photon excited NV^- fluorescence can quench under simultaneous 532 nm and infrared (780 – 1064 nm) excitation [126, 127, 155, 159]. These processes are related to both thermal and $NV^- \leftrightarrow NV^0$ conversion processes [155] though have not previously been reported under two-photon excitation.

The experiment presented in Section 4.4.3.2 shows the ODMR contrast was reduced by 73.7 % under two-photon excitation compared with under one-photon excitation at the same fluorescence rate. Previous research has shown that the ODMR contrast reduces at high temperature [158], however, assuming this reduction is the same for one and two-photon excited ODMR, this cannot fully explain the presented results. This may be due to heating of the microwave antenna causing a reduction in the microwave coupling efficiency. This can be investigated or mitigated in future research.

Finally, Chapter 5 described experiments that attempt to take the first steps towards building a magneto-sensitive laser using nitrogen-vacancy centres contained in a mm-scale diamond as an optical gain medium.

Despite building an experimental setup that was arguably capable of measuring stimulated emission from a reference sample of titanium:sapphire, experiments using diamond were inconclusive. Although a change in probe power was measured using a pump-probe setup, the wavelength, power and temporal dependencies of the change in probe power were inconsistent with a measurement of stimulated emission. This was found to be true whether the NV centres were pumped resonantly at 637 nm or on the phonon sideband at 532 nm. Further research would be required to ascertain which processes were being monitored using the probe beam and their relative contributions.

Although a measurement of stimulated emission from an NV ensemble was recently reported [22], the experiments were done under different conditions making comparisons difficult, as discussed in Section 5.3.1.5.

Despite the inconclusive measurements of stimulated emission, ODMR was demonstrated to be possible using a probe beam at 723 and 820 nm, where stimulated emission was expected to occur. At these wavelengths, using diamond sample #2, there was no dependence of probe power on ODMR contrast within the uncertainty of the measurements. This is consistent with a measurement of ODMR using stimulated emission. However, with both measured diamond samples, the wavelength dependencies of the ODMR contrast suggest that the probe was being absorbed by the NV⁻ singlet states. This has previously been used to perform ODMR [50, 113]. This hypothesis was strengthened by measurements at 950 nm where stimulated emission

was not expected to occur yet ODMR was successfully performed with increased ODMR contrast. Therefore, despite a possible successful measurement of ODMR using stimulated emission, these experiments must be considered inconclusive.

References

1. Jelezko F, Wrachtrup J. Single defect centres in diamond: a review. *Physica Status Solidi A*. 2006;203(13):3207-25.
2. Taylor JM, Cappellaro P, Childress L, Jiang L, Budker D, Hemmer PR, *et al*. High-sensitivity diamond magnetometer with nanoscale resolution. *Nature Physics*. 2008;4:810-6.
3. Jelezko F, Gaebel T, Popa I, Gruber A, Wrachtrup J. Observation of coherent oscillations in a single electron spin. *Phys Rev Lett*. 2004;92(7):076401.
4. Jiang L, Hodges JS, Maze JR, Maurer P, Taylor JM, Cory DG, *et al*. Repetitive readout of a single electronic spin via quantum logic with nuclear spin ancillae. *Science*. 2009;326(5950):267-272.
5. Tang L, Tsai C, Gerberich WW, Kruckeberg L, Kania DR. Biocompatibility of chemical-vapour-deposited diamond. *Biomaterials*. 1995;16(6):483-8.
6. Vaijayanthimala V, Tzeng Y-K, Chang H-C, Li C-L. The biocompatibility of fluorescent nanodiamonds and their mechanism of cellular uptake. *Nanotechnology*. 2009; 20(42):425103.
7. Schirhagl R, Chang K, Loretz M, Degen CL. Nitrogen-vacancy centers in diamond: nanoscale sensors for physics and biology. *Annu. Rev. Phys. Chem*. 2014;65:83-105.
8. Lodish H, Berk A, Zipursky SL, Matsudaira P, Baltimore D, Darnell J. *Molecular Cell Biology*, 4th ed. New York: W. H. Freeman; 2000.
9. Hall LT, Beart GC, Thomas EA, Simpson DA, McGuinness LP, Cole JH, *et al*. High spatial and temporal resolution wide-field imaging of neuron activity using quantum NV-diamond. *Sci Rep*. 2012;2:401.
10. Massobrio P, Tessadori J, Chiappalone M, Ghirardi M. In vitro studies of neuronal networks and synaptic plasticity in invertebrates and in mammals using multielectrode arrays. *Neural Plast*. 2015;2015:196195.
11. Paredes RM, Etzler JC, Watts LT, Zheng W, Lechleiter JD. Chemical calcium indicators. *Methods*. 2008;46(3):143-51.
12. Shew WL, Bellay T, Plenz D. Simultaneous multi-electrode array recording and two-photon calcium imaging of neural activity. *J Neurosci Methods*. 2010;192(1):75-82.
13. Hinterdorfer P (Ed.), Oijen A. *Handbook of single-molecule biophysics*. New York: Springer-Verlag;2009.

14. Vardi R, Goldental A, Sardi S, Sheinin A, Kanter I. Simultaneous multi-patch-clamp and extracellular-array recordings: single neuron reflects network activity. *Sci Rep.* 2016;6:36228.
15. Barry JF, Turner MJ, Schloss JM, Glenn DR, Song Y, Lukin MD, *et al.* Optical magnetic detection of single-neuron action potentials using quantum defects in diamond. *Proc Natl Acad Sci USA.* 2016;113(49):14133-8.
16. Cole KS, Moore JW. Ionic current measurements in the squid giant axon membrane. *J Gen Physiol.* 1960;44:123-67.
17. Wee TL, Tzeng YK, Han CC, Chang HC, Fann W, Hsu JH, *et al.* Two-photon excited fluorescence of nitrogen-vacancy centers in proton-irradiated type Ib diamond. *J Phys Chem A.* 2007;111(38):9379-86.
18. *Reviews of Physiology, Biochemistry and Pharmacology 160.* Berlin: Springer-Verlag; 2008.
19. Rand SC, Deshazer LG. Visible color-center laser in diamond. *Opt Lett.* 1985 1;10(10):481-3.
20. Davies G (Ed.). *Properties and Growth of Diamond.* Exeter: INSPEC IEE; 1994.
21. Vins VG, Pestryakov EV. Color centers in diamond crystals: their potential use in tunable and femtosecond lasers. *Diam. Relat. Mater.* 2006;15:569-71.
22. Jeske J, Lau DW, Vidal X, McGuinness LP, Reineck P, Johnson BC, *et al.* Stimulated emission from nitrogen-vacancy centres in diamond. *Nat Commun.* 2017;8:14000.
23. Jeske J, Cole JH, Greentree AD. Laser threshold magnetometry. *New J Phys.* 2016;18: 013015.
24. Balmer RS, Brandon JR, Clewes SL, Dhillon HK, Dodson JM, Friel I, *et al.* Chemical vapour deposition synthetic diamond: materials, technology and applications. *J. Phys. Condens. Matter.* 2009;21:364221.
25. Narayan R (Ed.). *Diamond-based materials for biomedical applications.* Cambridge: Woodhead; 2013.
26. Prelas MA (Ed.), Popovici G (Ed.), Bidelow LK (Ed.). *Handbook of industrial diamonds and diamond films.* New York: Marcel Dekker; 1998.
27. Kogel JE, Trivedi NC, Barker JM, Krukowski ST. *Industrial minerals & rocks: commodities, markets, and uses, 7th ed.* Littleton: SME; 2006.
28. Arnault JC (Ed.). *Nanodiamonds: advanced material analysis, properties and applications.* Amsterdam: Elsevier; 2017.
29. Mildren R (Ed.), Rabeau J (Ed.). *Optical engineering of diamond.* Weinheim: Wiley-VCH; 2013.
30. Grosz A (Ed.), Haji-Sheikh MJ (Ed.), Mukhopadhyay SC (Ed.). *High sensitivity magnetometers.* Switzerland: Springer; 2017.
31. Bernardi E, Nelz R, Sonusen S, Neu E. Nanoscale sensing using point defects in single-crystal diamond: Recent progress on nitrogen vacancy center-based sensors. *Crystals.* 2017;7:124.

32. Wrachtrup J, Kilin SY, Nizovtsev AP. Quantum computation using the ^{13}C nuclear spins near the single NV defect center in diamond. *Opt and Spectrosc.* 2001;91(3):429-37.
33. Grezes C, Julsgaard B, Kubo Y, Ma WL, Stern M, Bienfait A, *et al.* Storage and retrieval of microwave fields at the single-photon level in a spin ensemble. *Phys Rev A.* 2015;92:020301.
34. Nakamura K, Yamashita S, Tojo T, Mitsuishi M, Kataoka K, Yoshimoto M. Single-crystal synthesis of highly thermal conductive ^{12}C -enriched diamond from pyrolytic carbon powder by the high- pressure, high-temperature method. *Diam Relat Mater.* 2007;16:1765-9.
35. Yamamoto T, Umeda T, Watanabe K, Onoda S, Markham ML, Twitchen DJ, *et al.* Extending spin coherence times of diamond qubits by high temperature annealing [Preprint]. 2013. Available from: <https://arxiv.org/abs/1309.4316>
36. Faklaris O, Joshi V, Irinopoulou T, Tauc P, Sennour M, Girard H, *et al.* Photoluminescent diamond nanoparticles for cell labeling: study of the uptake mechanism in mammalian cells. *ACS Nano.* 2009;3(12):3955-62.
37. Mohan N, Chen CS, Hsieh HH, Wu YC, Chang HC. In vivo imaging and toxicity assessments of fluorescent nanodiamonds in *Caenorhabditis elegans*. *Nano Lett.* 2010;10:3692-99
38. Tzeng Y-K, Faklaris O, Chang BM, Kuo Y, Hsu JH, Chang HC. Superresolution imaging of albumin-conjugated fluorescent nanodiamonds in cells by stimulated emission depletion. *Angew Chem Int Ed.* 2011;50:2262-65.
39. Le Sage D, Arai K, Glenn DR, Devience SJ, Pham LM, Rahn-Lee L, *et al.* Optical magnetic imaging of living cells. *Nature.* 2013;496(7446):486.
40. Kucsko G, Maurer PC, Yao NY, Kubo M, Noh HJ, Lo PK, *et al.* Nanometre-scale thermometry in a living cell. *Nature.* 2013;500:54-8.
41. Wang W, Moses T, Linares RC, Shigley JE, Hall M, Butler JE. Gem-quality synthetic diamonds grown by a chemical vapor deposition (CVD) method. *Gems Gemology.* 2003;39(4):268-83.
42. Khmelnskiy RA. Prospects for the synthesis of large single-crystal diamonds. *Physics-Uspekhi.* 2015;58(2):134-49.
43. Bundy FP, Bassett WA, Weathers MS, Hemley RJ, Mao HK, Goncharov AF. The pressure-temperature phase and transformation diagram for carbon; updated through 1994. *Carbon.* 1996;34(2):141-53.
44. Giardini AA, Tydings JE. Diamond synthesis: observations on the mechanism of formation. *Am Mineral.* 1962;47:1393-421.
45. Chen Y, Zhang L. Polishing of diamond materials: mechanisms, modeling and implementation. London: Springer; 2013.
46. Nishinaga T (ed.), Rudolph P (ed.). Handbook of crystal growth: bulk crystal growth: growth mechanism and dynamics ,vol 2, part B, 2nd ed. Amsterdam: Elsevier; 2015.

47. Boudou JP, Curmi PA, Jelezko F, Wrachtrup J, Aubert P, Sennour M, *et al.* High yield fabrication of fluorescent nanodiamonds. *Nanotechnology*. 2009;20:235602.
48. Su LJ, Fang CY, Chang YT, Chen KM, Yu YC, Hsu JH, *et al.* Creation of high density ensembles of nitrogen-vacancy centers in nitrogen-rich type Ib nanodiamonds. *Nanotechnology*. 2013;24(31):315702.
49. Yang N (Ed.). *Novel aspects of diamond: from growth to applications*. Switzerland: Springer; 2015.
50. Budker D (Ed.), Kimball DF (Ed.). *Optical magnetometry*. Cambridge: Cambridge University Press; 2013.
51. Bar-Gill N, Pham LM, Jarmola A, Budker D, Walsworth RL. Solid-state electronic spin coherence time approaching one second. *Nat Commun*. 2013;4:1743.
52. Watanabe H, Kitamura T, Nakashima S, Shikata S. Cathodoluminescence characterization of a nitrogen-doped homoepitaxial diamond thin film. *J Appl Phys*. 2009;105(9):093529.
53. Ishiwata H, Nakajima M, Tahara K, Ozawa H, Iwasaki T, Hatano M. Perfectly aligned shallow ensemble nitrogen-vacancy centers in (111) diamond. *Appl Phys Lett*. 2017;111(4):043103.
54. Kleinsasser EE, Stanfield MM, Banks JKQ, Zhu Z, Li WD, Acosta VM, *et al.* High density nitrogen-vacancy sensing surface created via He⁺ ion implantation of 12C diamond. *Appl Phys Lett*. 2016;108(20):202401
55. Doherty MW, Manson NB, Delaney P, Jelezko F, Wrachtrup J, Hollenberg LC. The nitrogen-vacancy colour centre in diamond. *Phys Rep*. 2013;528(1):1-45.
56. Fukui T, Doi Y, Miyazaki T, Miyamoto Y, Kato H, Matsumoto T, *et al.* Perfect selective alignment of nitrogen-vacancy centers in diamond. *Appl Phys Express*. 2014;7(5):055201.
57. Aslam N, Waldherr G, Neumann P, Jelezko F, Wrachtrup J. Photo-induced ionization dynamics of the nitrogen vacancy defect in diamond investigated by single-shot charge state detection. *New J Phys*. 2013;15:013064.
58. Grotz B, Hauf MV, Dankerl M, Naydenov B, Pezzagna S, Meijer J, *et al.* Charge state manipulation of qubits in diamond. *Nat Commun*. 2012;3:729.
59. Pfender M, Aslam N, Simon P, Antonov D, Thiering G, Burk S, *et al.* Protecting a diamond quantum memory by charge state control. *Nano Letters*. 2017;17(10):5931-37
60. Praver S (Ed.), Aharonovich I (Ed.). *Quantum information processing with diamond: principles and applications*. Cambridge: Woodhead Publishing; 2014.
61. Acosta VM, Bauch E, Ledbetter MP, Santori C, Fu KMC, Barclay PE, *et al.* Diamonds with a high density of nitrogen-vacancy centers for magnetometry applications. *Phys. Rev. B*. 2009;80:115202
62. Rabeau JR, Reichart P, Tamanyan G, Jamieson DN, Praver S, Jelezko F, *et al.* Implantation of labelled single nitrogen vacancy centers in diamond using 15N. *Appl Phys Lett*. 2006;88(2):023113.

63. Naydenov B, Reinhard F, Lammle A, Richter V, Kalish R, D'haenens-Johansson UF, *et al.* Increasing the coherence time of single electron spins in diamond by high temperature annealing. *Appl Phys Lett.* 2010;97(24):242511.
64. Hui YY, Cheng C, Chang H. Nanodiamonds for optical bioimaging. *J Phys D Appl Phys.* 2010;43(37):374021.
65. Nagl A, Hemelaar SR, Schirhagl R. Improving surface and defect center chemistry of fluorescent nanodiamonds for imaging purposes—a review. *Anal Bioanal Chem.* 2015;407(25):7521-36.
66. Ermakova A, Pramanik G, Cai JM, Algara-Siller G, Kaiser U, Weil T, *et al.* Detection of a few metallo-protein molecules using color centers in nanodiamonds. *Nano Lett.* 2013;13(7):3305-09.
67. Hsiao WW, Hui YY, Tsai PC, Chang HC. Fluorescent nanodiamond: a versatile tool for long-term cell tracking, super-resolution imaging, and nanoscale temperature sensing. *Acc Chem Res.* 2016;49(3):400-7.
68. Arroyo-Camejo S, Adam M, Besbes M, Hugonin J, Jacques V, Greffet J, *et al.* Stimulated emission depletion microscopy resolves individual nitrogen vacancy centers in diamond nanocrystals. *ACS Nano.* 2013;7(12):10912-19.
69. Gruber A, Drabenstedt A, Tietz C, Fleury L, Wrachtrup J, Borczyskowski C. Scanning confocal optical microscopy and magnetic resonance on single defect centers. *Science.* 1997;276(5321):2012-14.
70. Kurtsiefer C, Mayer S, Weinfurter H, Zarda P, Weinfurter H. Stable solid-state source of single photons. *Phys Rev Lett.* 2000;85(2):290-3.
71. Beveratos A, Brouri R, Poizat JP, Grangier P. Bunching and antibunching from single NV color centers in diamond [Preprint]. 2000. Available from: <https://arxiv.org/abs/quant-ph/0010044>.
72. Hell SW, Wichmann J. Breaking the diffraction resolution limit by stimulated emission: stimulated-emission-depletion fluorescence microscopy. *Opt Lett.* 1994 Jun 1;19(11):780-2.
73. Doherty MW, Manson NB, Delaney P, Hollenberg LC. The negatively charged nitrogen-vacancy centre in diamond: the electronic solution. *New J Phys.* 2011;13:025019.
74. Neumann P, Kolesov R, Jacques V, Beck J, Tisler J, Batalov A, *et al.* Excited-state spectroscopy of single NV defects in diamond using optically detected magnetic resonance. *New J Phys.* 2009;11:013017.
75. Batalov A, Jacques V, Kaiser F, Siyushev P, Neumann P, Jelezko LJ, *et al.* Low temperature studies of the excited-state structure of negatively charged nitrogen-vacancy color centers in diamond. *Phys Rev Lett.* 2009;102(19):195506.
76. Huxter VM, Oliver TA, Budker D, Fleming GR. Vibrational and electronic ultrafast relaxation of the nitrogen-vacancy centers in diamond. *EPJ web conf.* 2013;41:04009.
77. Collins AT, Thomaz MF, Jorge MIB. Luminescence decay time of the 1.945 eV centre in type Ib diamond. *J Phys C Solid State Phys.* 2000;16(11):2177.

78. Berthel M, Mollet O, Dantelle G, Gacoin T, Huant S, Drezet A. Photophysics of single nitrogen-vacancy centers in diamond nanocrystals [Preprint]. 2015. Available from: <https://arxiv.org/abs/1501.03714v1>
79. Rondin L, Tetienne JP, Hingant T, Roch JF, Maletinsky P, Jacques V. Magnetometry with nitrogen-vacancy defects in diamond. *Rep Prog Phys*. 2014;77(5):056503
80. Beha K, Batalov A, Manson NB, Bratschitsch R, Leitenstorfer A. Optimum photoluminescence excitation and recharging cycle of single nitrogen-vacancy centers in ultrapure diamond. *Phys Rev Lett*. 2012;109(9):097404.
81. Manson NB, Harrison JP. Photo-ionization of the nitrogen-vacancy center in diamond. *Diam. Relat. Mater*. 2005;14:1705-10.
82. Halliday D, Resnick R, Walker J. *Fundamentals of physics*, 7th ed. Chichester; Wiley: 2004.
83. Hong, S, Grinolds MS, Pham LM, Le Sage D, Luan L, Walsworth, *et al*. Nanoscale magnetometry with NV centers in diamond. *MRS Bulletin*. 2013;38(2);155-61.
84. Hegyi A, Yablonovitch E. Molecular imaging by optically detected electron spin resonance of nitrogen-vacancies in nanodiamonds. *Nano Lett*. 2013 Mar 13;13(3):1173-8.
85. Hegyi A, Yablonovitch E. Nanodiamond imaging: a new molecular imaging approach. *Conf Proc IEEE Eng Med Biol Soc*. 2012;2012:2639-42.
86. Pham LM, Bar-Gill N, Le Sage D, Belthangady C, Stacey A, Markham M, *et al*. Enhanced metrology using preferential orientation of nitrogen-vacancy centers in diamond [Preprint]. 2012. Available from: <https://arxiv.org/abs/1207.3363v1>
87. Hegyi A, Yablonovitch E. Nanodiamond molecular imaging with enhanced contrast and expanded field of view. *J Biomed Opt*. 2014;19(1);011015.
88. Dréau A, Lesik M, Rondin L, Spinicelli P, Arcizet O, Roch JF, *et al*. Avoiding power broadening in optically detected magnetic resonance of single NV defects for enhanced DC- magnetic field sensitivity [Preprint]. 2013. Available from: <https://arxiv.org/abs/1108.0178v2>
89. Jensen K, Acosta VM, Jarmola A, Budker D. Light narrowing of magnetic resonances in ensembles of nitrogen-vacancy centers in diamond [Preprint]. 2012. Available from: <https://arxiv.org/abs/1210.5574v1>
90. Fraczek E, Savitski VG, Dale M, Breeze BG, Diggle P, Markham M, *et al*. Laser spectroscopy of NV- and NV0 colour centres in synthetic diamond. *Opt. Mater. Express*. 2017;7(7):2571-85.
91. Farfurnik D, Alfasi N, Masis S, Kauffmann Y, Farchi E, Romach Y, *et al*. Enhanced concentrations of nitrogen-vacancy centers in diamond through TEM irradiation. *Appl. Phys. Lett*. 2017;111:123101.
92. Bayat K, Choy J, Baroughi MF, Meesala S, Loncar M. Efficient, uniform, and large area microwave magnetic coupling to NV centers in diamond using double splitting resonators. *Nano Lett*. 2014;14(3):1208-13.

93. Gulka M, Bourgeois E, Hruby J, Siyushev P, Wachter G, Aumayr F, *et al.* Pulsed photoelectric coherent manipulation and detection of N-V center spins in diamond. *Phys Rev Appl.* 2017;7(4):044032.
94. Maze JR, Stanwix PL, Hodges JS, Hong S, Taylor JM, Cappellaro P. Nanoscale magnetic sensing with an individual electronic spin in diamond. *Nature.* 2008;455(7213):644-7.
95. Balasubramanian G, Chan IY, Kolesov R, Al-Hmoud M, Tisler J, Shin C, *et al.* Nanoscale imaging magnetometry with diamond spins under ambient conditions. *Nature.* 2008;455(7213):648-51.
96. Schoenfeld RS, Harneit W. Real time magnetic field sensing and imaging using a single spin in diamond. *Phys Rev Lett.* 2011;106(3):030802.
97. Maletinsky P, Hong S, Grinolds MS, Hausmann B, Lukin MD, Walsworth RL, *et al.* A robust scanning diamond sensor for nanoscale imaging with single nitrogen-vacancy centres. *Nat Nanotechnol.* 2012;7(5):320-4.
98. Grinolds MS, Hong S, Maletinsky P, Luan, Lukin LD, Walsworth RL, *et al.* Nanoscale magnetic imaging of a single electron spin under ambient conditions. *Nat Phys.* 2013;9: 215–19.
99. Knowles HS, Kara DM, Atatüre M. Observing bulk diamond spin coherence in high-purity nanodiamonds. *Nat Mater.* 2014;13(1):21-5.
100. Balasubramanian G, Neumann P, Twitchen D, Markham M, Kolesov R, Mizuochi N, *et al.* Ultralong spin coherence time in isotopically engineered diamond. *Nat Mater.* 2009;8(5):383-7.
101. Kumar P, Bhattacharya M. Magnetometry via spin-mechanical coupling in levitated optomechanics. *Opt Exp.* 2017;25(16):19568-82.
102. Pettit RM, Neukirch LP, Zhang Y, Vamivakas N. Coherent control of a single nitrogen-vacancy center spin in optically levitated nanodiamond. *J. Opt. Soc. Am. B.* 2017;34(6):C31.
103. Sushkov AO, Chisholm N, Lovchinsky I, Kubo M, Lo PK, Bennett SD, *et al.* All-optical sensing of a single-molecule electron spin. *Nano Lett.* 2014 Nov 12;14(11):6443-8.
104. Shields BJ, Unterreithmeier QP, de Leon NP, Park H, Lukin MD. Efficient readout of a single spin state in diamond via spin-to-charge conversion. *Phys Rev Lett.* 2015;114(13):136402.
105. Wolf T, Neumann P, Nakamura K, Sumiya H, Ohshima T, Isoya, J, *et al.* Subpicotesla diamond magnetometry. *Phys. Rev. X.* 2015;5:041001.
106. Pham LM, Sage D, Stanwix PL, Yeung TK, Glenn D, Trifonov A. Magnetic field imaging with nitrogen-vacancy ensembles. *New J Phys.* 2011;13:045021.
107. Steinert S, Dolde F, Neumann P, Aird A, Naydenov B, Balasubramanian G, *et al.* High sensitivity magnetic imaging using an array of spins in diamond. *Rev Sci Instrum.* 2010;81(4):043705.

108. Wojciechowski AM, Karadas M, Huck A, Osterkamp C, Jankuhn S, Meijer J, *et al.* Contributed review: camera-limits for wide-field magnetic resonance imaging with a nitrogen-vacancy spin sensor. *Rev Sci Instrum.* 2018;89(3):031501.
109. Maertz BJ, Wijnheijmer AP, Fuchs GD, Nowakowski ME, Awschalom DD. Vector magnetic field microscopy using nitrogen vacancy centers in diamond. *App Phys Lett.* 2010;96(9):1.3337096.
110. Schloss JM, Barry JF, Turner MJ, and Walsworth RL. Simultaneous broadband vector magnetometry using solid-state spins. *Phys Rev Appl.* 2018;10:034044.
111. Acosta VM, Bauch E, Jarmola A, Zipp LJ, Ledbetter MP, Budker D. Broadband magnetometry by infrared-absorption detection of nitrogen-vacancy ensembles in diamond. *Appl Phys Lett.* 2010;97:174104.
112. Dumeige Y, Chipaux M, Jacques V, Treussart F, Roch JF, Debuisschert T. Magnetometry with nitrogen-vacancy ensembles in diamond based on infrared absorption in a doubly resonant optical cavity. *Phys Rev B.* 2013;87:155202.
113. Jensen K, Leefer N, Jarmola A, Dumeige Y, Acosta VM, Kehayias P, Cavity-enhanced room-temperature magnetometry using absorption by nitrogen-vacancy centers in diamond. *Phys Rev Lett.* 2014 ;112(16):160802.
114. Chatzidrosos G, Wickenbrock A, Bougas L, Leefer N, Wu T, Jensen K. Miniature cavity-enhanced diamond magnetometer. *Phys Rev Appl.* 2017;8:044019.
115. Savitski VG. Optical gain in NV-colour centres for highly-sensitive magnetometry: a theoretical study. *J Phys D.* 2017;50:475602.
116. Bourgeois E, Jarmola A, Siyushev P, Gulka M, Hruby J, Nesladek F, *et al.* Photoelectric detection of electron spin resonance of nitrogen-vacancy centres in diamond. *Nat. Commun.* 2015;6.8577.
117. Bourgeois E, Londero E, Buczak K, Balasubramaniam Y, Wachter G, Stursa J, *et al.* Enhanced dual-beam excitation photoelectric detection of NV magnetic resonances in diamond [Preprint]. 2016. Available from: <https://arxiv.org/abs/1607.00961>
118. Mita Y. Change of absorption spectra in type- Ib diamond with heavy neutron irradiation. *Phys Rev B Condens Matter.* 1996;53(17):11360-11364.
119. Wang K, Steeds JW, Li Z, Tian Y. Photoluminescence studies of both the neutral and negatively charged nitrogen-vacancy center in diamond. *Microsc Microanal.* 2016;22(1):108-12.
120. Doi Y, Fukui T, Kato H, Makino T, Yamasaki S, Tashima T, *et al.* Pure negatively charged state of the NV center in n-type diamond. *Phys Rev B.* 2016;93:081203.
121. Karaveli S, Gaathon O, Wolcott A, Sakakibara R, Shemesh OA, Peterka DS, *et al.* Modulation of nitrogen vacancy charge state and fluorescence in nanodiamonds using electrochemical potential. *Proc Natl Acad Sci U.S.A.* 2016;113(15):3938-43.
122. Schreyvogel C, Wolfer M, Kato H, Schreck M, Nebel CE. Tuned NV emission by in-plane Al-Schottky junctions on hydrogen terminated diamond. *Sci. Rep.* 2014;4:3634.

123. Forneris J, Ditalia Tchernij S, Tengattini A, Enrico E, Grilj V, Skukan N, *et al.* Electrical control of deep NV centers in diamond by means of sub-superficial graphitic micro-electrodes [Preprint]. 2016. Available from: <https://arxiv.org/abs/1607.05553>
124. Chou JP, Bodrog Z, Gali A. First principles study of charge diffusion between proximate solid state qubits and its implications on sensor applications [Preprint]. 2018. Available from: <https://arxiv.org/abs/1708.08626?context=quant-ph>
125. Jayakumar H, Henshaw J, Dhomkar S, Pagliero D, Laraoui A, Manson NB, *et al.* Optical patterning of trapped charge in nitrogen-doped diamond. *Nat. Commun.* 2016;7:12660.
126. Chen XD, Li S, Shen A, Dong Y, Dong CH, Guo GC, *et al.* Near-infrared-enhanced charge-state conversion for low-power optical nanoscopy with nitrogen-vacancy centers in diamond. *Phys Rev App.* 2017;7(1):014008.
127. Hopper DA, Grote RR, Exarhos AL, Bassett LC. Near-infrared-assisted charge control and spin readout of the nitrogen-vacancy center in diamond. *Phys Rev B.* 2016;94:241201.
128. Shenderova OA, Gruen DM. *Ultrananocrystalline diamond: synthesis, properties and applications*, 2nd ed. Oxford: Elsevier; 2012.
129. Hrubesch FM, Braunbeck G, Stutzmann M, Reinhard F, Brandt MS. Efficient electrical spin readout of NV- centers in diamond. *Phys Rev Lett.* 2017;118(3):037601.
130. Pfender M, Aslam N, Waldherr G, Neumann P, Wrachtrup J. Single-spin stochastic optical reconstruction microscopy. *Proc. Natl. Acad. Sci. U.S.A.* 2014;111(41):14669-74.
131. Han KY, Kim SK, Eggeling C, Hell SW. Metastable dark States enable ground state depletion microscopy of nitrogen vacancy centers in diamond with diffraction-unlimited resolution. *Nano Letters.* 2010;10(8):3199-203.
132. Seeler KA. *System dynamics: an introduction for mechanical engineers*. New York: Springer; 2014.
133. Chabay RW, Sherwood BA. *Matter and interactions*. 3rd ed. New Jersey: Wiley; 2011.
134. El-Ella HA, Ahmadi S, Wojciechowski AM, Huck A, Andersen UL. Optimised frequency modulation for continuous-wave optical magnetic resonance sensing using nitrogen-vacancy ensembles. *Opt. Express.* 2017;25(13):14809-21.
135. Carr J. *RF components and circuits*. Oxford: Newnes; 2002.
136. Acosta VM, Bauch E, Ledbetter MP, Waxman A, Bouchard LS, Budker D. Temperature dependence of the nitrogen-vacancy magnetic resonance in diamond. *Phys Rev Lett.* 2010;104(7):070801
137. Sasaki K, Monnai Y, Saijo S, Fujita R, Watanabe H, Ishi-Hayase J, *et al.* Broadband, large-area microwave antenna for optically detected magnetic resonance of nitrogen-vacancy centers in diamond. *Rev Sci Instrum.* 2016;87(5):053904.

138. Herrmann J, Appleton MA, Sasaki K, Monnai Y, Teraji T, Itoh KM, *et al.* Polarization and frequency tunable microwave circuit for selective excitation of nitrogen-vacancy spins in diamond. *Appl Phys Lett.* 2016;109(18):183111.
139. Mrózek M, Mlynarczyk J, Rudnicki DS, Gawlik W. Circularly polarized microwaves for magnetic resonance study in the GHz range: application to nitrogen-vacancy in diamonds. *Appl Phys Lett.* 2015;107(1):013505.
140. Yang L-L, Liu Q-Q, Pan X-Y, Chen D-M. Design and application of a near field microwave antenna for the spin control of nitrogen-vacancy centers. *Chinese Phys Lett.* 2010;27(3):038401.
141. Balanis CA. *Antenna theory: analysis and design.* 3rd ed. New Jersey: Wiley; 2005.
142. Träger F (Ed.). *Springer handbook of lasers and optics.* New York: Springer; 2007.
143. Stanwix PL, Pham LM, Maze JR, Le Sage D, Yeung TK, Cappellaro P, *et al.* Coherence of nitrogen-vacancy electronic spin ensembles in diamond [Preprint]. 2011. Available from: <https://arxiv.org/abs/1006.4219v2>
144. Steinert S, Ziem F, Hall LT, Zappe A, Schweikert M, Götz N, *et al.* Magnetic spin imaging under ambient conditions with sub-cellular resolution. *Nat Commun.* 2013;4:1607.
145. Tetienne JP, Hingant T, Rondin L, Cavailles A, Mayer L, Dantelle G, *et al.* Spin relaxometry of single nitrogen-vacancy defects in diamond nanocrystals for magnetic noise sensing [Preprint]. 2013. Available from: <https://arxiv.org/abs/1304.1197v1>
146. Ivanov IP, Li X, Dolan PR, Gu M. Nonlinear absorption properties of the charge states of nitrogen- vacancy centers in nanodiamonds. *Opt Lett.* 2013;38(8):1358-60.
147. Andrews DL (Ed.). *Photonics: scientific foundations, technology and applications.* vol 1. New Jersey: Wiley; 2015.
148. Gali A. Theory of neutral nitrogen-vacancy center in diamond and its qubit application [Preprint]. 2009. Available from: <https://arxiv.org/abs/0902.2387v1>
149. De Graef M, McHenry ME. *Structure of materials: an introduction to crystallography, diffraction and symmetry.* New York: Cambridge University Press; 2007.
150. Housecroft CE, Sharpe AG. *Inorganic chemistry,* 4th ed. Essex: Pearson; 2012.
151. Braun M (Ed.), Gilch P (Ed.), Zinth W (Ed.). *Ultrashort laser pulses in biology and medicine.* Berlin: Springer; 2008.
152. Ji P, Balili RB, Beaumariage J, Mukherjee S, Snoke DW, Gurudev D. Multiple-photon excitation of nitrogen vacancy center in diamond [Preprint]. 2018. Available from: <https://arxiv.org/abs/1710.07539v2>
153. Benninger KP, Piston DW. Two-photon excitation microscopy for the study of living cells and tissues. *Curr Protoc Cell Biol.* 2013;20(1):1-36.

154. Kim E, Acosta VM, Bauch E, Budker D, Hemmer PR. Electron spin resonance shift and linewidth broadening of nitrogen-vacancy centers in diamond as a function of electron irradiation dose. *Appl Phys Lett*. 2012;101(8):082410.
155. Ji P, Dutt MV. Charge state dynamics of the nitrogen vacancy center in diamond under 1064 nm laser excitation [Preprint]. 2016. Available from: <https://arxiv.org/abs/1603.08066v2>
156. Chen XD, Zou CL, Sun FW, Guo GC. Optical manipulation of the charge state of nitrogen-vacancy center in diamond. *Appl Phys Lett*. 2013;103(1):013112.
157. Szczuka C, Drake M, Reimer JA. Effects of laser-induced heating on nitrogen-vacancy centers and single-nitrogen defects in diamond. *J. Phys. D*. 2017;50(39):395307.
158. Toyli DM, Christle DJ, Alkauskas A, Buckley BB, Walle CG, Awschalom DD. Measurement and control of single nitrogen-vacancy center spins above 600 K. *Phys Rev X*. 2012;2(3):031001.
159. Lai ND, Faklaris O, Zheng D, Jacques V, Chang HC, Roch JF, *et al*. Quenching nitrogen-vacancy center photoluminescence with an infrared pulsed laser. *New J Phys*. 2013;15:033030.
160. Geiselmann M, Marty R, García FJ, Quidant R. Fast optical modulation of the fluorescence from a single nitrogen-vacancy centre. *Nat Phys*. 2013; 9:785-9.
161. Goldman ML, Sipahigil A, Doherty MW, Yao NY, Bennett SD, Markham M, *et al*. Phonon-induced population dynamics and intersystem crossing in nitrogen-vacancy centers. *Phys Rev Lett*. 2015;114(14):145502.
162. Wickenbrock A, Zheng H, Bougas L, Leefer N, Afach S, Jarmola A, *et al*. Microwave-free magnetometry with nitrogen-vacancy centers in diamond. *Appl. Phys. Lett*. 2016;109(5):053505.
163. Muller M. Introduction to confocal fluorescence microscopy. 2nd ed. Bellingham: SPIE; 2006.
164. Keiser G. Biophotonics: concepts to applications. Singapore: Springer; 2016.
165. Prelas MA (Ed.), Gielisse P (Ed.), Popovici G (Ed.), Spitsyn BV (Ed.), Stacy T. (Ed.). Wide band gap electronic materials. 3. high technology – vol 1. Dordrecht: Springer; 1995.
166. Han KY, Willig KI, Rittweger E, Jelezko F, Eggeling C, Hell SW. Three-dimensional stimulated emission depletion microscopy of nitrogen- vacancy centers in diamond using continuous-wave light. *Nano Lett*. 2009;9(9):3323-9.
167. Reider GA. Photonics: an introduction. Switzerland: Springer; 2016.
168. Svelto O, Hanna DC (Ed.). Principles of lasers. 5th ed. New York: Springer; 2010.
169. Aull B, Jenssen H. Vibronic interactions in Nd:YAG resulting in nonreciprocity of absorption and stimulated emission cross sections. *IEEE J. Quantum Electron*. 1982;18(5):925-30.
170. Lakowicz JR. Principles of fluorescence spectroscopy. 3rd ed. New York: Springer; 2006.

171. Digonnet MJF, Gaeta CJ. Theoretical analysis of optical fiber laser amplifiers and oscillators. *Appl Opt.* 1985;24(3):333-42.
172. Backus S, Kirchner M, Lemons R, Schmidt D, Durfee C, Murnane M, *et al.* Direct diode pumped Ti:sapphire ultrafast regenerative amplifier system. *Opt. Express.* 2017;25(4):3666-74.
173. Menzel R. *Photonics: linear and nonlinear Interactions of laser light and matter.* Berlin: Springer; 2007.
174. Moulton PF. Spectroscopic and laser characteristics of ti:al2O3. *J Opt Soc Am B.* 1986;3(1):125-33.
175. Koechner W. *Solid- State Laser Engineering, 6th and updated Ed.* New York: Springer; 2006.
176. DeShazer LG, Eggleston JM. Saturation of green absorption in titanium-doped sapphire laser crystals. *Optics Letters.* 1988;13(5):363-5.
177. Kehayias P, Doherty MW, English D, Fischer R, Jarmola A, Jensen K, *et al.* The infrared absorption band and vibronic structure of the nitrogen-vacancy center in diamond [Preprint]. 2013. Accessible From: <https://arxiv.org/abs/1301.6197v2>
178. Choi J, Choi S, Kucsko G, Maurer PC, Shields BJ, Sumiya H, *et al.* Depolarization dynamics in a strongly interacting solid-state spin ensemble. *Phys Rev Lett.* 2017;118(9):093601.
179. Iakoubovskii K, Adriaenssens GJ, Nesladek M. Photochromism of vacancy-related centres in diamond. *J Phys Condens Matter.* 2000;12(2):189-99.
180. Lowther JE, Vermeulen LA. The 1.71 eV phonon sideband at the GR1 centre in diamond. *J Phys C Solid State Phys.* 1982;15(4):81-5.
181. Mironov VP, Martinovich EF, Grigorov VA. Laser materials based on diamond with GR1 centers. *Diam Relat Mater.* 1994;3(4-6):936-8.
182. Li BB, Tosin MC, Peterlevitz AC, Baranauskas V. Measurement of the substitutional nitrogen activation energy in diamond films. *Appl Phys Lett.* 1998;73(6):812-4.
183. Enckevort WJP. Temperature dependence of optical absorption by the single-substitutional nitrogen donor in diamond. *J Phys Condens Matter.* 1992;4(9):2361-73.
184. John R, Lehnert J, Mensing M, Spemann D, Pezzagna S, Meijer J. Bright optical centre in diamond with narrow, highly polarised and nearly phonon-free fluorescence at room temperature. *New J Phys.* 2017;19:053008.
185. Haubler S, Thiering G, Dietrich A, Waasem N, Teraji T, Isoya J, *et al.* Photoluminescence excitation spectroscopy of SiV- and GeV- color center in diamond. *New J Phys.* 2017;19:063036.
186. Gaebel T, Domhan M, Wittmann C, Popa I, Jelezko F, Rabeau J, *et al.* Photochromism in single nitrogen-vacancy defect in diamond. *Appl Phys B.* 2006;82(2):243-6.

187. Siyushev P, Pinto H, Vörös M, Gali A, Jelezko F, Wrachtrup J. Optically controlled switching of the charge state of a single nitrogen-vacancy center in diamond at cryogenic temperatures. *Phys Rev Lett.* 2013;110(16):167402.

Appendices

Appendix 1 – MATLAB code to acquire and average magnetometry data

```
%Program to acquire and average magnetometry data
%Written by - Calum Macrae - Feb 2017

%Clear all variables
clear all

%Connect to Digital Acquisition Card
s = daq.createSession('ni');

%record from channels 0 and 7
addAnalogInputChannel(s, 'Dev1', 0, 'Voltage');
addAnalogInputChannel(s, 'Dev1', 7, 'Voltage');

%set sample rate and acquisition time
s.Rate =125000
s.DurationInSeconds=1;

%acquire Data
[data,time] = s.startForeground;

%seperate magnetometry data and trigger data in differnt variables
trigdata=data(:,2);
magdata=data(:,1);

%obtain trigger point - note this section of code was adapted from
code
%found at https://www.picotech.com/support/topic13207.html -
Accessed Feb
%2017

% Set the threshold to 0 V.
threshold = 2.5;

% Create the offset data. Need to append a NaN to the final sample
since
```

```

% both vectors need to have the same length.
offsetData = [trigdata(2:end); NaN];

% Find the rising edge(s).
risingEdge = find(trigdata < threshold & offsetData > threshold);

%end of code adapted from -
https://www.picotech.com/support/topic13207.html

%obtain first sample
sample1=magdata(risingEdge(1):risingEdge(2));

%set averaging sample length - three samples are removed to account
for
%variance in number of samples between trigger points
samplesize=size(sample1,1)-3;

%create an array with each sample of magnetometry data
for counter=1:(size(risingEdge,1)-1)

sampleddata{counter}=magdata(risingEdge(counter):risingEdge(counter)
+samplesize);
%remove mean to perform AC averaging - i.e. remove DC component
sampleddata{counter}=sampleddata{counter}-
mean(magdata(risingEdge(counter):risingEdge(counter)+samplesize));
end

%average data
averageddata=zeros(samplesize+1,1);
for counter2=1:size(sampleddata,2)
    averageddata=averageddata+sampleddata{counter2};
end
averageddata=averageddata./size(sampleddata,2);

```

Appendix 2 – MATLAB code to perform negative feedback

```
%Program to Perform Negative Feedback to maintain AC magnetometry
under DC
%Drift - Written by Calum Macrae - Feb 2017

%clear all variables
clear all

%Set initial microwave frequency - this is found experimentally
freq=2.9256*10^9

%Create Variable called counter
counter=1

%Connect to oscilloscope
deviceObj = icdevice('tektronix_tds2024.mdd', interfaceObj);
connect(deviceObj);
groupObj = groupObj(1);

% Connect to microwave signal generator
deviceObj2 = icdevice('AgilentRfSigGen_AgilentRfSigGen.mdd',
'USB0::2391::7937::MY53051062::0::INSTR');
connect(deviceObj2);

%Create loop - 100000000 is simply a large number to repeat for a
long
%period of time

for counter=1:100000000
%Read the waveform from the oscilloscope - this is the output of the
%lock-in amplifier
[Y1,X1] = invoke(groupObj, 'readwaveform', 'channell');
%Calculate the mean of the waveform and calculate the new microwave
frequency
%6*10^3 is the adjustment factor (i.e. proportional adjustment)
%this is found experimentally
freq=freq+mean(Y1)*6*10^3;
%set new microwave frequency
set(deviceObj2.Rf(1), 'Frequency', freq);
```

```
end
```

```
% Disconnect for microwave signal generator  
disconnect(deviceObj2);
```